Electronic coupling in self-assembled nanocrystal arrays

a scanning tunneling microscopy study

Cover design by author
Photograph taken by Ivar Pel
ISBN 978-90-393-4891-8

Electronic coupling in self-assembled nanocrystal arrays

a scanning tunneling microscopy study

Elektronische koppeling in zelfgeorganiseerde nanokristal structuren

bestudeerd met scanning tunneling microscopie

(met een samenvatting in het Nederlands)

Proefschrift

ter verkrijging van de graad van doctor aan de Universiteit Utrecht op gezag van de rector magnificus, prof. dr. J. C. Stoof, ingevolge het besluit van het college voor promoties in het openbaar te verdedigen op woensdag 1 oktober 2008 des middags te 2.30 uur

door

Karin Overgaag

geboren op 24 mei 1978, te Dosso, Niger

Promotores:	Prof. dr. D.A.M. Vanmaekelbergh
	Prof. dr. J. J. Kelly
Co-promotor:	Dr. P. Liljeroth

Contents

Chapter 1

Semiconductor quantum dots and quantum dot assemblies

This thesis deals with semiconductor nanocrystals, also called quantum dots. The research is focussed on the electronic properties of individual semiconductor nanocrystals and the influence of quantum mechanical coupling between the nanocrystals on these properties. Nearly all properties of nanometer sized crystals depend strongly on their size, shape and material. In this chapter, we discuss the basic principles of quantum size effects and their effect on the electronic properties of semiconductor quantum dots. The individual nanocrystals can be considered as chemical building blocks for larger and more complex structures. The properties of these nanocrystal solids depend on the properties of the individual nanocrystal building blocks and the interactions between them. We will discuss how the properties of the quantum dots are influenced by quantum mechanical coupling between the dots in a nanocrystal superlattice.

1.1 Introduction

Macroscopic semiconductor crystals are well known and of utmost importance for e.g. microprocessors chips, transistors, solar cells and many other electronic devices. The properties of these semiconductors change as the size of the crystal is reduced to the nanometer scale. New electronic and optical properties arise that can be tuned by adjusting the diameter, the material and/or the shape of these nanocrystals (NCs) or quantum dots (QDs).[1–6]

The effect of the crystal size on the electronic properties of semiconductors results from spatial confinement of electrons and holes and is well described by S, P, D, etc. symmetry similar to the electronic wavefunctions in atoms. Therefore, QDs are often referred to as 'artificial atoms'. About twenty years ago, Kastner stated: "The age of artificial atoms has only just begun".[7] Regarding today's immense scientific activity dealing with the synthesis and opto-electrical properties of semiconductor nanocrystals, we should conclude that this was no exaggeration.

The nanocrystalline QD materials that are used in this research are CdSe and PbSe. The choice to investigate CdSe[8–11] and PbSe QDs[12–15,29] is motivated by the fact that they exhibit strongly different electronic properties, CdSe QDs can be tuned in the nanometer range to emit throughout the visible spectrum and PbSe QDs can be tuned in the near infra-red range of the spectrum relevant to telecommunication.

The good control over size, shape and size distribution of these colloidal nanocrystals enables one to use them as 'building blocks' for the preparation of larger and more complex architectures, e.g. nanocrystal molecules, two-dimensional arrays and three-dimensional assemblies.[1–5,17,23–25] In the literature, the latter are often called nanocrystal superlattices, nanocrystal- or quantum dot solids. The properties of these structures depend on the properties of the individual nanocrystal building blocks, and on the chemical, electronic or magnetic coupling between them. Materials with new collective properties could be designed which makes these QD solids interesting for future opto-electronic applications, such as LEDs, lasers and solar cells.[26–31]

In the next section, the theory of the transition from a bulk semiconductor material to nanometer sized QDs will be introduced, followed in section 1.3 by the principles of self-assembly used to design and control the fabrication of superlattices, especially binary structures. Section 1.4 discusses the effects of quantum mechanical coupling (electronic coupling) which occur in larger structures made of QDs. Finally, the outline of this thesis is presented in the last section of this chapter.

1.2 Semiconductors and quantum dots

In order to understand the change of properties in the transition from bulk semiconductors to nanometer sized semiconductor nanocrystals, the free-electron model is used and refined to explain band structure formation. Then, by further refining the model, the change of the properties of the semiconductor crystals of sizes below 10 nm is discussed.

Bulk crystalline semiconductor materials consist of a periodic lattice of atoms. The model used to explain the electronic properties of solids is the Sommerfeld free-electron-gas model. In this model, the electrons are assumed to move in a field-free space; the potential due to the atomic cores and other electrons is neglected except at the boundary of the solid (simple-particle-in-a-box, figure 1.1A, dashed line).[32] The electrons are unable to leave the crystal, thus the probability of finding an electron outside the 'box' is zero. Inside the 'box' the electrons are supposed to move independently and each electron obeys the time-independent Schrödinger equation:

$$-\frac{\hbar^2}{2m_e}\nabla^2\Psi(r)+V(r)\Psi(r)=E\Psi(r) \tag{1.1}$$

where Ψ is the wavefunction for the electron and E is its energy, V is the potential, r is the position vector (x,y,z), m_e is the free electron mass and $\hbar$ is Planck's constant. Because in this model the potential energy of the electron due to the atoms in the crystal lattice is neglected, $V(x,y,z)$ is taken as a constant and the envelope wavefunction Ψ is given by:

$$\Psi_{\vec{k}}(\vec{r})=\frac{1}{\sqrt{L^3}}e^{i\vec{k}\cdot\vec{r}}=\sqrt{\frac{8}{L^3}}sin(k_x x)sin(k_y y)sin(k_z z) \tag{1.2}$$

which represents a standing wave with a wavelength $\lambda_e=\frac{2\pi}{k}$ where $\vec{k}$ is the wave vector (k_x,k_y,k_z). The possible wavefunctions for an electron in a cubic 'box' in one direction (x-direction) is shown in figure 1.1B for the lowest three eigenvalues. The kinetic energy of the electron is:

$$E(\vec{k})=\frac{\hbar^2\vec{k}^2}{2m_e} \tag{1.3}$$

This is the dispersion relation of the free electron model which is presented in figure 1.1C. The allowed energy levels for the electrons of a crystal of macroscopic dimensions lie very close together, the electrons can have any k-value.

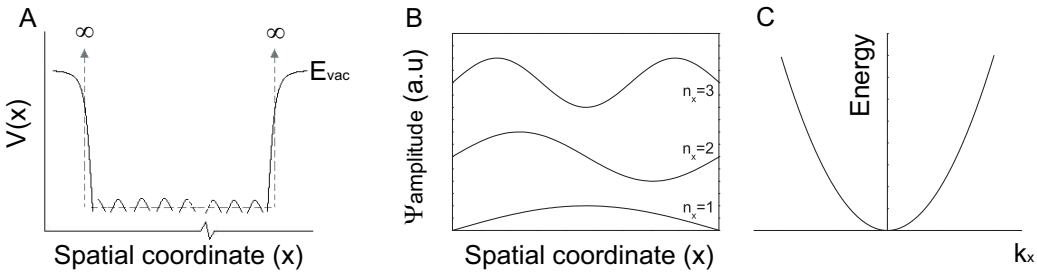

Figure 1.1: Schematic of the potential energy of an electron in a crystalline solid (A) Sommerfeld model (dashed line) assuming an electron in an infinite potential well and assuming an electron in a periodic potential due to atomic cores (solid lines). (B) Schematic of an electron in an infinite potential well of size L showing the first three eigenvalues in the x-direction corresponding to quantum numbers $n_x = 1, 2, 3$. (C) Dispersion relation of the free electron model. Electrons can have any k-value.

The free-electron model ignores the interactions of electrons with the periodic crystal lattice and therefore cannot explain the formation of energy bands in semiconductors. The crystal lattice is composed of atoms with a spacing of a few Ångstroms as is presented in figure 1.2A by black dots. The distance between the centers of the cores is denoted as a. An electron travelling through the crystal with a wavelength much longer than a does not feel this periodic potential. However, electrons with short wavelength feel the periodic potential energy variation due to the positive ion cores (figure 1.1A and figure 1.2A, solid black line). The electron wave will diffract from the atoms for wavelengths that obey the Bragg condition ($k = \frac{n\pi}{a}$). The Bragg diffracted electrons are reflected by the crystal structure and interfere with their incoming counterparts. This leads to two standing waves (ψ_+ and ψ_-). The probability density function corresponding to the first standing wave is centered at the core ions (solid line), the probability density function of the second wave lies between the core ions (dotted line in figure 1.2A). The kinetic energy is preserved since both waves have the same wave vector, however, the potential energy is different. The scattering of the free electrons by the periodic lattice leads to discontinuities in the dispersion relation: at $k = n\frac{\pi}{a}$, a gap opens up at the edge of the Brillouin zone. For one direction this is presented in figure 1.2B. The dispersion relation for free electrons is a good approximation for most of the electrons in a band, but does not hold for electrons near the edge of the Brillouin zones.

This is shown by solving the time-independent Schrödinger equation for a periodic potential $V(r) = V(r + r_n)$ where $r_n = n_1a_1 + n_2a_2 + n_3a_3$. The solution of the single electron Schrödinger equation for a periodic potential can be written as a modulated plane wave:

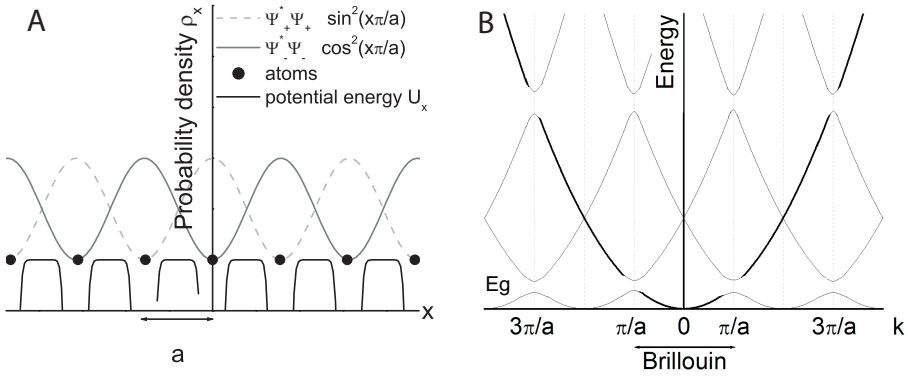

Figure 1.2: (A) Bottom, potential energy *V(x)* of an electron in a one-dimensional lattice. The positions of the atoms are indicated by black dots with separation a, the lattice constant. Top dashed line, probability density for the standing wave produced by Bragg reflection at $k = \pm\pi/a$ for a standing wave at the upper edge of the band. Top solid line, probability density for a standing wave at the lower edge of the band. (B) Splitting of the free-electron energy bands at the edge of the Brillouin zone.

$$\Psi_k(r) = U_j(r)e^{ik\cdot r} \tag{1.4}$$

with a modulation function $U_j(r) = U_j(r + r_n)$ resulting from the periodic potential of the periodic lattice and j is the band index. This result is known as a form of Bloch's theorem and the wavefunctions are called the Bloch waves of an electron.

Having explained the properties of bulk semiconductor materials, we can further refine the model to explain the electronic band structure of nanocrystalline QDs. The QDs used in this research are in the size range of 3-10 nm and electron scattering with the periodic lattice leads to band formation, identical to the macroscopic semiconductor crystals (bulk semiconductors). Assuming again the simple 'particle in a box' within the effective mass approximation[6,33] and infinite potential barriers, the electron wave functions have to change more drastically within the limiting size of the "box" (QD). The electrons are described by standing waves which limits the number of allowed k-values. If the size of the "box" in the x-direction is L_x, the allowed k-values are $k_x = 2\pi/\lambda = n_x\pi/L_x$. With decreasing dimensions of the 'box', the energy of the wavefunction increases (equation1.3) leading to an increase of the forbidden gap and a reduced number of states (k-values) as is schematically shown in figure 1.3 for three different regimes. The regimes are assigned by comparing the Bohr radius (a_B) of the electron-hole exciton (Wannier exciton) with the size of the nanocrystal. When the size of the crystal is much larger than the Bohr radius

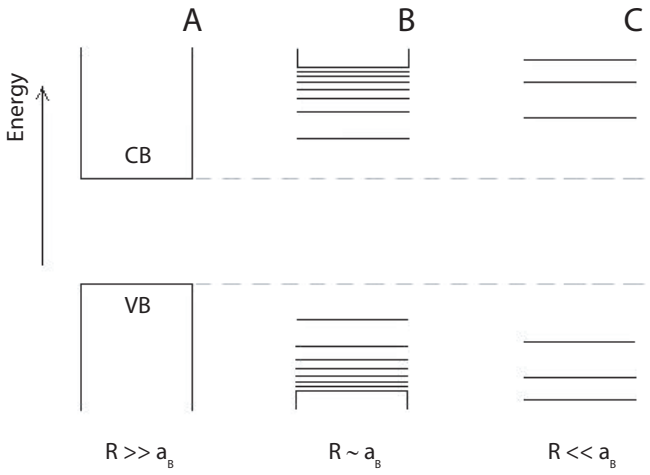

Figure 1.3: Relation between the electronic structure of (A) a macroscopic semiconductor and a semiconductor nanocrystal (B) in the weak confinement regime and (C) the strong confinement regime. The valence and conduction levels are separated by a bandgap and the energy spacing increases with decreasing QD size.

($R >> a_B$), no quantum confinement effects are observed. For large three-dimensional crystalline semiconductor materials, the energy band is presented in figure 1.3A as a continuous filled valence band (VB) and an empty conduction band (CB) separated by a bandgap energy (E_g). At the size range $R \sim a_B$ - the weak quantum confinement regime - the bandgap increases and the energy level separation increases at the band edges where the density of states (DOS) is low (figure 1.3B). In the strong confinement regime where $R < a_B$, the energy level separation increases even more as is presented in figure 1.3C. The energy levels have S-, P- , D- etc. wavefunction symmetry[6] and QDs are therefore often referred to as "artificial atoms".[7] The quantum dots used in this research belong to the strong confinement regime. This quantum confinement offers unprecedented possibilities to manipulate the opto-electronic properties by changing the size and/or the shape of a given type of semiconductor nanocrystal.

1.3 Self-assembly

Besides the possibility to manipulate single QDs, it is believed that they can serve as 'building blocks' for larger ordered QD solids with novel optical and electrical properties. These properties will depend on the nature of the QD building blocks and the degree of coupling between them. In recent years, a lot of research has been devoted to the design and controlled fabrication of single component and binary structures using colloidal

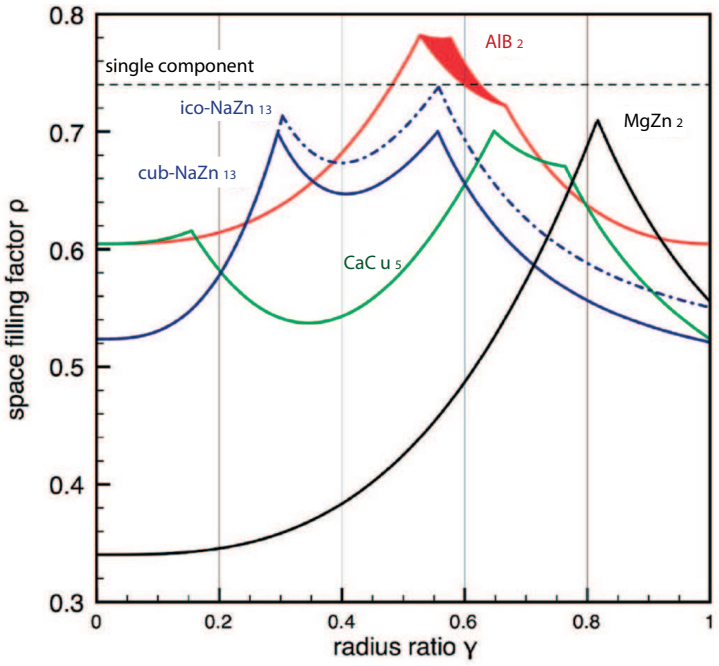

Figure 1.4: Space-filling curves of AlB_2, $MgZn_2$ (AB_2) , cub-$NaZn_{13}$, ico-$NaZn_{13}$ (AB_{13}) and $CaCu_5$ (AB_5) for the range of radius ratio $0 < \gamma < 1$ (reproduced from references 17, 23). The space-filling curves of AlB_2, cub-$NaZn_{13}$, and ico-$NaZn_{13}$ are obtained by Murray and Sanders.[24] The space-filling curve of $MgZn_2$ is obtained by Parthé.[25] The space-filling factor (ρ = 0.74) corresponding to the single component close-packed structure is indicated by the dotted line.

nanocrystals with the aim to create functional materials.[34–36]

Nanocrystal self-assembly (i.e. colloidal crystallization) is the only practical preparation method to form binary structures. Two different types of NCs are mixed in a suspension and binary structures are formed by evaporation of the solvent. This method has already been proven successful especially in the case of combinations of semiconductor and metal NCs. However, at this moment, the driving forces in the formation of these NC superlattices are not well understood.

The formation of nanocrystal superlattices is often described by assuming that NCs act as non-interacting hard-spheres. Using this approximation, the only possible driving force in the formation of ordered structures is the increase in entropy of the system.[37–41] A loss in entropy (configurational contribution) occurs when NCs are centered on lattice sites in a NC solid. At the same time a gain in entropy arises from the fact that the NC on its lattice

site has more free volume to move than it has in a disordered (fluid) phase of the same density (more space available for each particle to perform local motions). At sufficient high densities, the gain in entropy due to this increase in free volume exceeds the loss in configurational entropy and therefore favors crystallization.[40]

Theoretical predictions on the formation of binary structures are often presented in space-filling curves where the maximum packing fraction is presented as a function of the 'size ratio'. Binary structures form when the close-packed densities of A_mB_n are greater than the close-packed densities of the single-component spheres A or B. For the large spheres A and small spheres B, an overview of these space filling curves for AB_2, AB_5 and AB_{13} are presented in figure 1.4.[17,24,25,36] Phase diagrams for AB, AB_2 and AB_{13} for different size ratios can be found in references 37–39.

The QDs used in this research are capped with ligands to stabilize them in the solution and to prevent them from aggregation. We are thus not dealing with hard-spheres, but hard-spheres with soft shells. In the formation of binary NC structures, the distance between NCs decreases, ligands of the NCs can interdigitate, resulting in van der Waals attraction forces. Besides the influence of capping molecules in the formation of binary structures, Coulomb interactions and dipole-dipole interactions between the NCs could play a role in structure formation. These interactions (forces) depend on the nature of the building blocks, the substrate (patterning) and the solution used in the self-assembly process. The fabricated binary structures can be used as model system to test existing theories predicting the configurational stability of these structures.

1.4 Quantum mechanical coupling

As discussed in section 1.2, QDs belong to the strong confinement regime. Electrons are localized within the limiting space of the QD (spherical potential well) leading to quantum confinement effects. When two QDs are placed close to each other, electronic wavefunctions can become delocalized over the complete 'molecule'. This delocalization is directly related to a reduction of the quantum confinement. Figure 1.5A presents a scheme of the electronic wavefunctions ($n = 1$) confined in the QDs 1 and 2 (solid lines) and in figure 1.5B the electrons are delocalized over the two QDs:

$$\Psi = C_1\Psi_1 + C_2\Psi_2 \tag{1.5}$$

where Ψ_1 and Ψ_2 are the electron orbitals centered on the two QDs and C_1 and C_2 are normalization constants. When the two orbitals (Ψ_1 and Ψ_2) overlap and have the same sign C_1=C_2, their wavefunctions interfere constructively and give rise to a region of enhanced

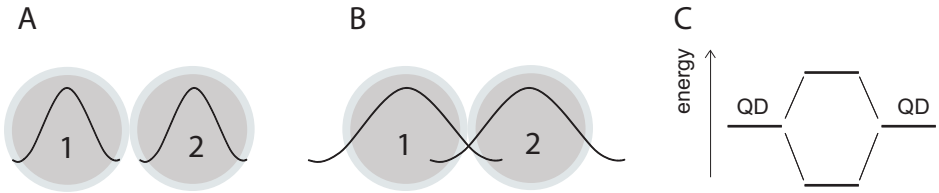

Figure 1.5: Model used for the effective mass approximation for two QDs (dielectric spherical well) positioned close to each other (A) Cross-section of the energy diagram of a QD molecule the ground state wavefunctions are not delocalized over the QD molecule (B) for a QD molecule where the ground state wavefunction is delocalized over the QD molecule. (C) Schematic of level hybridization when the electron wavefunction is delocalized over the QD molecule.

amplitude between the two QDs. This is often related to molecular orbital theory[42] and called a bonding orbital. The coefficients depend on the energy mismatch of the orbitals and C_1=C_2=1/$\sqrt{2}$ for identical QDs. In the second 'molecular orbital', C_1=-C_2, the two atomic orbitals interfere destructively leading to an antibonding orbital. An electron in a quantum mechanical coupled 'molecule' has a lower kinetic energy than an electron in a single QD because the electron now occupies a larger volume than when confined to a single QD (particle in a box, section 1.2). When *N* QDs in a system are involved in quantum mechanical coupling, the energy levels form *N* 'molecular orbitals' (figure 1.5C).

The electronic coupling strength depends strongly on the extension of the orbitals outside the nanocrystals, and the width and height of the energy barrier between two nanocrystal neighbours. This means that the nature of the nanocrystals, the capping molecules, the possible chemical linkers between the nanocrystals and the degree of disorder in the QD solid will strongly influence the electronic coupling, and thus the opto-electronic properties of the nanocrystal solid.

1.5 Outline of this thesis

Experimentally, the electronic structure of colloidal nanocrystals has been studied mostly via light absorption and emission spectroscopy.[8,9,43,44] However, due to limited spatial resolution of these techniques, only sample average properties are probed. They do not give insight in the electronic properties of single isolated nanocrystals. Therefore we prefer to study these systems using a local probe technique.

This thesis explores the electronic properties of individual PbSe and CdSe QDs, QD molecules, two-dimensional arrays and three-dimensional assemblies using scanning tunneling microscopy (STM) and scanning tunneling spectroscopy (STS). The local configu-

ration is measured with STM, and STS is used to probe the local density of states at the position of interest.[45,46]

Chapter 2 presents the principles of STM and STS, needed for detailed analysis and consistent interpretation of the experiments. In chapter 3, the results of low-temperature STS on single quantum dots (QDs) in a size range of 3-10 nm are described for colloidal PbSe quantum dots covalently bound to a self-assembled monolayer of hexanedithiol. The aim of this work is to unravel the mysteries of the electronic structure of PbSe quantum dots. A long lasting debate on the second optical transition in absorption experiments and broadening of resonances in spectroscopy are discussed. While the properties of individual PbSe semiconductor quantum dots are more and more understood, chapter 4 and 5 present the effects of quantum mechanical coupling as a function of the number of neighbouring QDs. Therefore we mechanically stabilized individual and molecular aggregates of PbSe QDs (dimers, trimers, . . .) in a two-dimensional superlattice of wide band-gap CdSe QDs acting as an inert matrix, and made micrometer large monolayers of hexagonally packed PbSe QDs. Chapter 6 deals with superlattices consisting of hexagonally packed double layers of CdSe nanocrystals. The local density of states is measured with STS and is related to the local configuration. In the last chapter we show that self-organization of colloidal PbSe and CdSe semiconductor nanocrystals with a size ratio of 0.57 leads to formation of binary structures with AB_2 or AB_{13} lattice over large micrometer sized areas. These well ordered binary superlattices provide opportunities to further study the electronic properties and the interparticle coupling with scanning tunneling microscopy and spectroscopy and provide possibilities to design meta-materials with new collective properties.

References

[1] Henglein, A. "Photochemistry of colloidal cadmium sulfide. 2. Effects of adsorbed methyl viologen and of colloidal platinum" J. Phys. Chem. 1982, 86, 2291-2293.

[2] Rossetti, R.; Ellison, J. L.; Gibson, J.M.; Brus, L.E. "Size effects in the excited electronic states of small colloidal CdS crystallites" J. Chem. Phys. 1984, 80, 4464-4467.

[3] Alivisatos, A.P. "Semiconductor clusters, nanocrystals, and quantum dots" Science 1996, 271, 933-937.

[4] Delerue, C.; Lannoo, M. "Nanostructures, theory and modelling" Springer-Verlag, Berlin, 2004.

[5] Duonghong, D.; Ramsden, J.; Grätzel, M. "Dynamics of interfacial electron-transfer processes in colloidal semiconductor systems" J. Am. Chem. Soc. 1982, 104, 2917-2985.

[6] Brus, L.E. "Electronic wave functions in semiconductor clusters: experiment and theory" J. Chem. Phys. 1986, 90, 2555-2560.

[7] Kastner, M.A. "Artificial atoms" Physics today 1988, 46, 24-29.

[8] Efros, A.L.; Rosen, M. "The electronic structure of semiconductor nanocrystals" Annu. Rev. Mater. Sci. 2000, 30, 475-512.

[9] Murray, C.B.; Kagan, C.R.; Bawendi, M.G. "Synthesis and characterization of monodisperse nanocrystals and close-packed nanocrystal assemblies" Annu. Rev. Mater. Sci. 2000, 30, 545-610.

[10] Jdira, L.; Liljeroth, P.; Stoffels, E.; Vanmaekelbergh, D.; Speller, S. "Size-dependent single-particle energy levels and interparticle coulomb interactions in CdSe quantum dots measured by scanning tunneling spectroscopy" Phys. Rev. B 2006, 73, 115305/1-6.

[11] Yu, W.W.; Qu, L.; Guo, W.; Peng, X. "Experimental determination of the extinction coefficient of CdTe, CdSe, and CdS nanocrystals" Chem. Mater. 2003, 15, 2854-2860.

[12] Koole, R.; Allan, A.; Delerue, C.; Meijerink, A; Vanmaekelbergh, D.; Houtepen, A.J. "Optical investigation of quantum confinement in PbSe nanocrystals at different points in the brilloin zone" Small 2008, 4, 127-133.

[13] Trinh, M.T.; Houtepen, A.J.; Schins, J.M.; Piris, J.; Siebbeles, L.D.A. "Nature of the second optical transition in PbSe nanocrystals" Nano Lett. 2008, 8, 2112-2117.

[14] Liljeroth, P.; Zeijlmans van Emmichoven, P.A.; Hickey, S.G.; Weller, H; Grandidier, B.; Allan, G.; Vanmaekelbergh, D. "Density of states measured by scanning tunneling spectroscopy sheds new light on the optical transitions in PbSe nanocrystals" Phys. Rev. Lett. 2005, 95, 086801/1-4.

[15] Moreels, I.; Lambert, K.; De Muynck, D.; Vanhaecke, F.; Poelman, D.; Martins, J.C.; Allan, G.; Hens, Z. "Composition and size-dependent extinction coefficient of colloidal PbSe quantum dots" Chem. Mater. 2007, 19, 6101-6106.

[16] An, J.M.; Franceschetti, A.; Dudly, S.V.; Zunger, A. "The peculiar electronic structure of PbSe quantum dots" Nano Lett. 2006, 6, 2728-2735.

[17] Chen, Z.; O'Brien, S. "Structure direction of II-VI semiconductor quantum dot binary nanoparticle superlattices by tuning radius ratio" ACS Nano 2008, 2, 1219-1229.

[18] Kiely, C. J.; Fink, J.; Brust, M.; Bethell, D.; Schiffrin, D. J. "Spontaneous ordering of bimodal ensembles of nanoscopic gold clusters" Nature 1998, 396, 444-446.

[19] Rogach, A. L. "Binary superlattices of nanoparticles: self-assembly leads to metamaterials" Angew. Chem.-Int Ed 2004, 43, 148-149.

[20] Redl, F. X.; Cho, K. S.; Murray, C. B.; O'Brien, S. "Three-dimensional binary superlattices of magnetic nanocrystals and semiconductor quantum dots" Nature 2003, 423, 968-971.

[21] Shevchenko, E. V.; Talapin, D. V.; Kotov, N. A.; O'Brien, S.; Murray, C. B. "Structural diversity in binary nanoparticle superlattices" Nature 2006, 439, 55-59.

[22] Urban, J. J.; Talapin, D. V.; Shevchenko, E. V.; Kagan, C. R.; Murray, C B. "Synergism in binary nanocrystal superlattices leads to enhanced p-type conductivity in self-assembled PbTe/Ag_2Te thin films" Nature Mat. 2007, 6, 115-121.

[23] Chen, Z.; Moore, J.; Radtke, G.; Sirringhaus, H.; O'Brien, S. "Binary Nanoparticle Superlattices in the Semiconductor- Semiconductor System: CdTe and CdSe" J. Am. Chem. Soc. 2007, 129, 15702-15709.

[24] Murray, M.J.; Sanders, J.V. "Close-packed structures of spheres of 2 different sizes II. The packing densities of likely arrangements" Philos. Mag. A 1980, 42, 721-740.

[25] Partheé, E. "Space filling of crystal structures. A contribution to the graphical presentation of geometrical relationships in simple crystal structures" Z. Kristallogr. 1961, 115, 52-79.

[26] Wehrenberg, B.L.; Wang, C.; Guyot-Sionnest, P. "Interband and intraband optical studies of PbSe colloidal quantum dots" J. Phys. Chem. B 2002, 106, 10634-10640.

[27] Murray, C.B.; Sun, S.H.; Gaschler, W.; Doyle, H.; Betley, T.A.; Kagan, C.R. "Colloidal synthesis of nanocrystals and nanocrystal superlattices" IBM J. Res. Dev. 2001, 45, 47-56.

[28] Wise, F.W. "Lead salt quantum dots: the limit of strong quantum confinement" Acc. Chem. Res. 2000, 33, 773-780.

[29] Wehrenberg, B.L.; Guyot-Sionnest, P. "Electron and hole injection in PbSe quantum dot films" J. Am. Chem. Soc. 2003, 125, 7806-7807.

[30] Hens, Z.; Vanmaekelbergh, D.; Kooij, E. S.; Wormeester, H.; Allan, G.; Delerue, C. "Effect of quantum confinement on the dielectric function of PbSe" Phys. Rev. Lett. 2004, 92, 026808/1-4.

[31] Schaller, R.D.; Klimov, V.I. "High efficiency carrier multiplication in PbSe Nanocrystals: implications for solar energy conversion" Phys. Rev. Lett. 2004, 92, 186601/1-4.

[32] Ibach, H.; Lüth, H. "Solid-state physics" Springer-Verlach, New York, 1995.

[33] Brus, L.E. "Electron-electron and electron-hole interactions in small semiconductor crystallites: the size dependence of the lowest excited electronic state" J. Chem. Phys. 1984, 80, 4403-4409.

[34] Murray, C.B.; Kagan, C.R.; Bawendi, M.G. "Self-organization of CdSe nanocrystallites into three-dimensional quantum dot superlattices" Science 1995, 270, 1335-1338.

[35] Collier, C.P.; Vossmeyer, T.; Heath, J.R. "Nanocrystal superlattices" Annu. Rev. Phys. Chem. 1998, 49, 371-404.

[36] Chen, Z.; Moore, J.; Radtke, G.; Sirringhaus, H.; O'Brien, S. "Binary nanoparticle superlattices in the semiconductor-semiconductor system: CdTe and CdSe" J. Am. Chem. Soc. 2007, 129, 15702-15709.

[37] Eldridge, M.D.; Madden, P.A.; Frenkel, D. "The stability of the AB_{13} crystal in a binary hard sphere system" Mol. Phys. 1993, 79, 105-120.

[38] Eldridge, M.D.; Madden, P.A.; Frenkel, D. "A computer simulation investigation into the stability of the AB_2 superlattice in a binary hard sphere system" Mol. Phys. 1993, 80, 987-995.

[39] Cottin, X.; Monsona, P.A. "Substitutionally ordered solid solutions of hard spheres" J. Chem. Phys. 1995, 102, 3354-3360.

[40] Frenkel, D. "Order through disorder: entropy strikes back" Physics world, 1993, 6, 24-25.

[41] Hunt, N.; Jardine, R.; Bartlett, P. "Superlattice formation in mixtures of hard-sphere colloids" Phys. Rev. E, 2000, 62, 900-913.

[42] Atkins, P.; Jones, L. "Chemical principles, the quest for insight" W.H. Freeman and company, New York, 2005.

[43] Banin, U.; Millo, O. "Tunneling and optical spectroscopy of semiconductor nancrystals" Annu. Rev. Phys. Chem. 2003, 54, 465-492.

[44] El-Sayed, M.A. "Small is different: shape-, size-, and composition-dependent properties of some colloidal semiconductor nanocrystals" Acc. Chem. Res. 2004, 37, 326-333.

[45] Banin, U.; Cao, Y.; Katz, D.; Millo, O. "Identification of atomic-like electronic states in indium arsenide nanocrystal quantum dots" Nature 1999, 400, 542-544.

[46] Bakkers, E.P.A.M.; Hens, Z.; Zunger, A.; Franceschetti, A.; Kouwenhoven, L. P.; Gurevich, L.; Vanmaekelbergh, D. "Shell-tunneling spectroscopy of the single-particle energy levels of insulating quantum dots" Nano Lett. 2001, 1, 551-556.

Chapter 2

Scanning tunneling microscopy and spectroscopy

Since the invention of the scanning tunneling microscope in the early eighties by Binnig and Rohrer, the interest in nanoscale structures has increased tremendously. Scanning tunneling microscopy (STM) and spectroscopy (STS) can measure topography and electronic structures with very high spatial resolution. The combination of STM and STS has already proved to be very useful in probing the geometry and electronic structure of individual atoms and molecules. In this chapter, the basic principles of STM and STS are discussed as well as the way these techniques can be used to perform experiments on semiconductor nanocrystalline quantum dots.

2.1 Introduction

In the late nineteen seventies at the IBM Research Laboratory in Zurich, Gerd Binnig and fellow researcher Heinrich Rohrer were interested to measure the properties of thin inhomogeneous insulators between two metal plates. The original idea was to locally investigate the electronic structure of an insulator on an area less than 100 Ångstrom in diameter, but an appropriate instrument was not available. Binnig and Rohrer considered to replace one of the metal electrodes by a positionable metal tip in a vacuum. Soon they realized that they did not only have a probe (tip) to investigate the electronic structure, but, that by moving the metal tip over the substrate also topographic images could be obtained.[2] The final experimental set-up is now widely known as the scanning tunneling microscope.[2–4]

Since the invention in the early 1980s, STM has been used in numerous studies with the emphasis on imaging and electronic properties at atomic resolution. In 1991 Eigler et al. showed the possibility of manipulating individual atoms and molecules[5,6] by for example building an island of CO molecules. Ho et al. showed in 1999 that it was even possible to investigate chemical reactions with STM by making and breaking individual chemical bonds between a metal atom Fe and CO molecules.[7]

2.2 Scanning tunneling microscopy and spectroscopy

Scanning tunneling microscopy (STM) is based on the principle of electron tunneling between two metals. This can be described as follows: we consider two metal plates (conductive electrodes) separated by a vacuum or insulating layer (figure 2.1A region II) brought close to each other (region I and III). If the electron energy in the metal in region I (dotted line) is large enough ($E > V$), a free electron travelling from left to right (represented as a wave), does not feel the energy barrier and just passes the vacuum barrier. However, when the electron energy is smaller than the vacuum barrier ($E < V$), the electron travelling from the left to the right has a certain probability of tunneling through the vacuum barrier (solid line). The probability of this process depends on the barrier height and width and can be described by the decay of the wavefunction in the barrier region, given by:[1]

$$|\Psi(L)|^2 = |\Psi(0)|^2 e^{-2\kappa L} \tag{2.1}$$

where $\kappa = \frac{\sqrt{2m(V-E)}}{\hbar}$ within the vacuum barrier, $E < V$ and L is the width of the barrier. This is an elastic tunneling process due to energy conservation. The current measured through such a barrier is related to the probability of finding an electron at the other

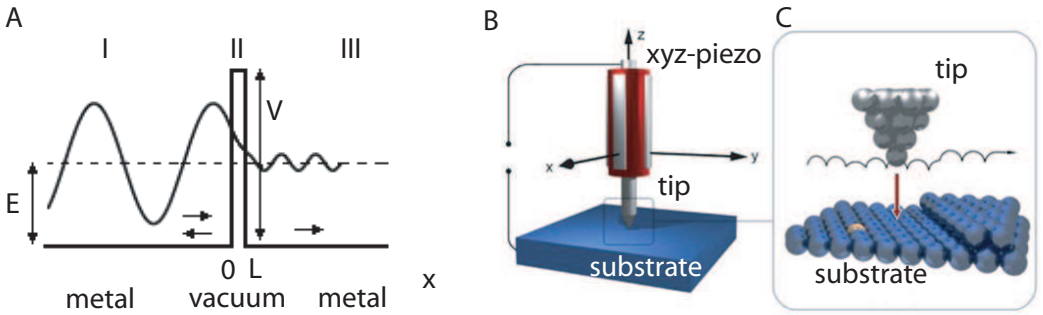

Figure 2.1: Schematic representation of (A) the tunneling effect, an electron (wave) hits a barrier of width L and height V. The barrier is sufficiently thin to pass part of the wave decaying exponentially, (B) macroscopic scale of the scanning tunneling microscope with a tip positioned less than 1 nm from a substrate. (C) Microscopic representation of tunneling in the constant current mode, the solid line representing the line profile.

side of the barrier. Equation 2.1 shows that the current $I \propto |\Psi(L)|^2$ is thus exponentially dependent on the barrier height (E) and width (L). This means that the electron tunneling rate (current) is extremely sensitive to the barrier height and width variations. At an effective barrier height ($E - V$) of 4 eV ($\kappa \sim 0.1$ nm), almost a factor of ten in current increase is observed as the barrier width decreases with 0.1 nm.

STM can be operated in two modes, in constant-current or constant-height mode. In this research mainly the constant-current mode is used. The metal tip is brought a few Ångström (typically < 10 Å) above the conducting sample surface as is shown in figure 2.1B. In figure 2.1C, an atomic scale of the illustration is shown with substrate atoms and an atomically sharp tip. In the constant-current mode, the metal tip scans the surface in a raster pattern (figure 2.1C, solid line). The distance between the tip and the sample surface is adjusted by the feedback loop to keep the current constant. The recorded z-position together with the xy-position results in a three-dimensional map of the surface. Due to the exponential dependence of the tunneling probability on distance, images with sub-Ångstrom resolution can be obtained.

Scanning tunneling spectroscopy (STS) gives information on the electronic properties of the sample. This is done by positioning the tip at a region of interest chosen from the STM image. The feedback loop is interrupted to keep the tip-sample distance constant and the current is measured as a function of the bias voltage. The conductance spectrum ($\mathrm{d}I/\mathrm{d}V$) is proportional to the local density of states.

The first experimental results with STM were published in 1982[3,4,8] and over the past

twenty five years, different models have been developed to explain the experimentally obtained topography images and spectroscopy data. Bardeen[9] and Harrison[10] were one of the first to give an equation for the tunnel current. In their approach called the time-dependent perturbation theory, the current is determined by a combination of local density of states (LDOS) of the sample, the LDOS of the tip and the tunneling matrix element between the states of the tip and the sample. From this result, Tersoff and Hamann[11–13] have developed an approach to simplify Bardeen's approximation. They assumed that the tip can have an arbitrary shape but is atomically sharp, figure 2.1C. The tip has a constant density of states and the wavefunction is assumed S-like. When a bias voltage is applied between tip and substrate, Tersoff and Hamann showed that the tunnel current at a certain distance between tip and sample can be reduced to:

$$I \propto \sum |\Psi_{sub}(r_0)|^2 \delta(E_{sub} - E_{F_{tip}}) \tag{2.2}$$

where $|\Psi_{sub}(r_0)|$ is the amplitude of the wavefunction of the substrate at the position of center of curvature r_0 of the tip. $\delta(E_{sub} - E_{F_{tip}})$ results from the fact that an electron can only tunnel if there is an unoccupied state in the substrate electrode E_{sub} with the same energy as the tip $E_{F_{tip}}$ (elastic tunneling). $\sum |\Psi_{sub}(r_0)|^2 \delta(E_{sub} - E_{F_{tip}})$ is the surface local density of states (LDOS) at the Fermi energy of the tip $E_{F_{tip}}$ (bias voltage). STM and STS open a range of possibilities to investigate the shape (dimensions) and the electronic structure of single QDs.

2.3 Quantum dots and spectroscopy

Initial STS measurements were performed on metallic grains[14] and covalently linked metal nanoparticles,[15,16] followed by measurements on colloidal CdSe QDs[17] and InAs QDs.[18,19] The experiments on InAs and CdSe QDs presented the first examples of a clearly resolved atomic-like energy level spectrum of colloidal quantum dots.

2.3.1 Double barrier tunnel junction

In order to study a single isolated QD or larger structures of QDs with STM, QDs have to be immobilized on a conducting substrate. In the last few years, different methods have been developed to immobilize these dots: (i) QDs are absorbed on a conducting substrate by van de Waals interactions of the capping molecules with the substrate, figure 2.2A; (ii) A self-assembled monolayer of functionalized organic molecules are used to covalently anchor QDs to the substrate, figure 2.2B; (iii) QDs are mechanically stabilized in an array formed by self-assembly, figure 2.2C. While the method of absorption by van der Waals

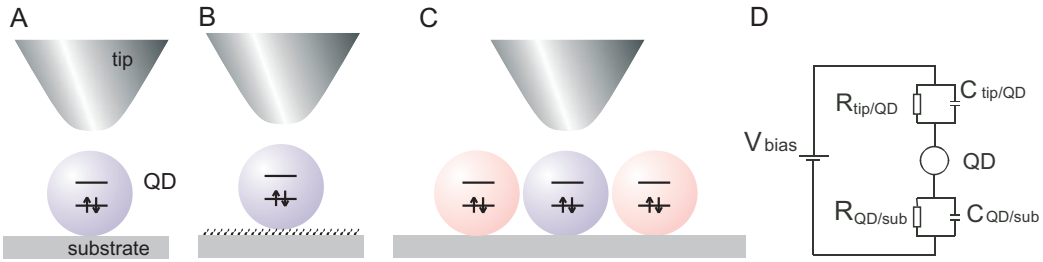

Figure 2.2: Schematic representation of STM in a DBTJ configuration (A) a QD absorbed on a conducting substrate by van de Waals interactions of the capping molecules (B) Self-assembled monolayer on the substrate used to covalently anchor QDs to the substrate (C) QDs mechanically stabilized in an array. (D) The equivalent electric circuit of the DBTJ.

interactions has been proven to be insufficient to immobilize the dots, the other two methods have been very successful. Both methods are used for experiments described in this thesis. Once the QDs are immobilized and the STM tip is positioned above a QD, a double barrier tunnel junction (DBTJ) is formed. The barriers (junctions) are located between the tip and dot, and between the dot and substrate. The equivalent electric circuit of the DBTJ is illustrated in figure 2.2D, the two tunnel junctions are represented by a parallel configuration of resistances and capacitances.

2.3.2 Potential distribution

To obtain quantitative information and relate the bias voltage at resonance (peaks in the tunneling spectra) to the energy levels of the QD, the distribution of the bias voltage over the DBTJ must be known. The bias voltage distribution in the tunneling spectrum is characterized by η:

$$\eta = \frac{V_{dot} - V_{tip}}{V_{bias}} \tag{2.3}$$

where η is the fraction of the bias voltage that drops between the tip and the QD, V_{tip} is the electrochemical potential of the tip, V_{dot} the potential at the center of the QD and V_{bias} is the total applied potential difference over the DBTJ. The potential distribution over the DBTJ can be calculated by solving the Laplace equation for a realistic tip-dot-substrate configuration. Figure 2.3A shows the schematic representation of the geometry used in our simulations. A bias is applied between the metal tip and substrate, the tip is connected to zero potential, the substrate is connected to a V_{sub} potential (in this example 1 V) and the QD is modelled as a dielectric sphere. Assuming a charge free region of space (this can be justified by assuming that the QD is neutral, with a dielectric constant $\varepsilon_{QD} = \varepsilon_{in}$),

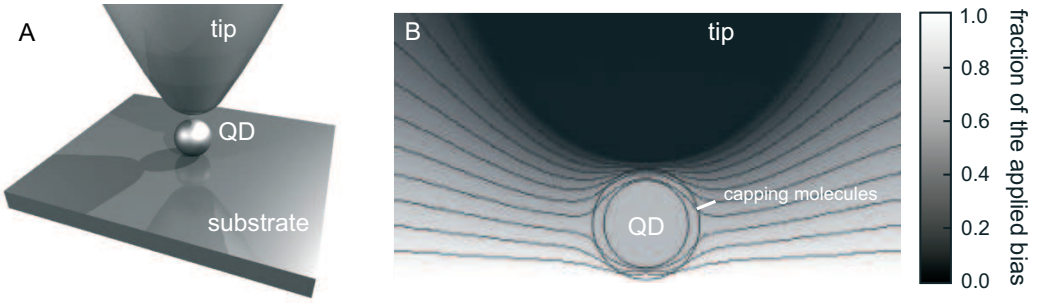

Figure 2.3: (A) Schematic representation of a single QD in a STM (B) Potential distribution in the tip/QD/substrate junction calculated by solving the Laplace equation for a dielectric sphere of radius 3.5 nm with dielectric constant 227 (PbSe).

the solution of the electric potential (*V*) is found by solving the Laplace equation: $\nabla^2 V$=0. As an example, the electric potential over a DBTJ is calculated for a metal tip positioned above a PbSe QD chemically attached to a gold substrate. This potential distribution calculation will be used in the following chapters of this thesis. For a PbSe QD with a core radius 3.0 nm (capping layer thickness of 0.5 nm, tip-dot distance 1.0 nm, dot-substrate distance 0.5 nm, QD ε_{QD}=227 and the capping molecules $\varepsilon_{capping}$=3), η ~0.75. This implies that most of the potential (bias voltage) drops between the tip and the QD as is shown in figure 2.3B. Due to the high dielectric constant of PbSe, the potential over the QD is constant.

For this same realistic tip-dot-substrate configuration, the effect on η is calculated: (i) for different QD materials by varying the dielectric constant, (ii) for different QD sizes, (iii) for different tip-dot distances and (iv) for different tip radii. The dependence of η on the dielectric constant is shown in figure 2.4A for QDs with a core diameter of 6 nm and a tip-dot distance of 0.5 nm. We found that η becomes strongly dependent on the dielectric constant below 50. Due to the low dielectric constant, the potential distribution over the QD is not constant resulting in a stronger dependence on η. For PbSe QDs ($\varepsilon_{QD} = 227$) we found η ~0.75 and for CdSe QDs ($\varepsilon_{QD} = 10$) we found η ~0.7. These two examples are relevant as they are the materials used in our studies. The dependence of η on the diameter of QDs is shown in figure 2.4B. Due to the high dielectric constant of PbSe the bias distribution over the dot remains almost constant with size. As the dielectric constant of CdSe is much lower, a clear decrease in η is observed for increasing QD sizes. The effect of η on the tip-dot distance is shown in figure 2.4C. The tip-dot distance is determined by the current that is applied over the DBTJ and can thus be adjusted during STS experiments. For the simulations on PbSe and CdSe QDs with a core diameter of 6 nm we found the same trend, η decreases with decreasing tip-dot distance.

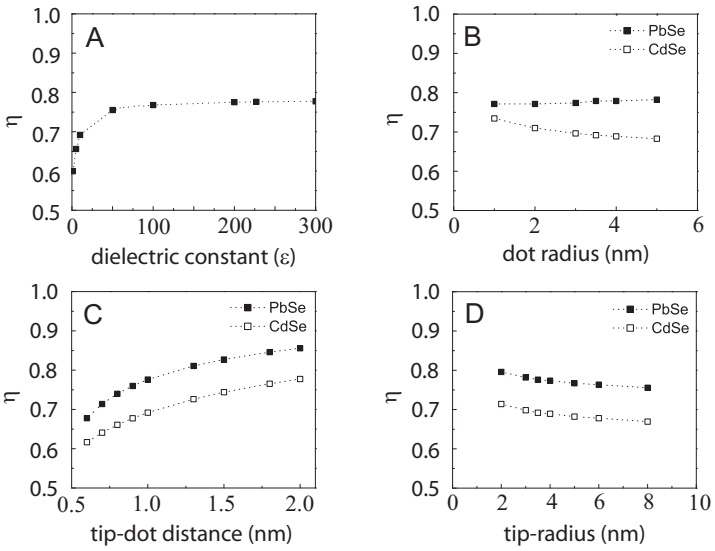

Figure 2.4: Effect on the potential distribution over a DBTJ for (A) single QDs made of different materials (B) a PbSe QD ($\varepsilon = 227$) of different diameters (C) PbSe QD of 7 nm diameter with adjusting tip-dot distances (D) PbSe QD with tip-dot distance 1.0 nm as a function of bluntness of the tip (E) PbSe QD with changing dielectric constant of capping molecules.

The potential distribution over the DBTJ becomes more symmetric which means that a larger fraction of the bias voltage drops between the QD and the substrate. This situation can also be reached by increasing the distance between the QD and substrate. The effect of the sharpness of the tip on η is shown in figure 2.4D. We found that the relation between η and the sharpness of the tip is almost linear for tip radii between 2 and 8 nm. For a sharp tip, most of the potential drops between the tip and QD whereas with a blunt tip, a larger part of the potential distribution is allowed to drop over the dot-substrate barrier. The sharpness of the tip can be deduced experimentally from topography images.

2.3.3 Shell-tunneling spectroscopy

As was already mentioned in section 2.3.2, tunnelling spectroscopy on individual QDs is based on resonant tunnelling of electrons (holes) across the double-barrier tunnel junction. In order to study the electronic properties of an isolated QD, it is required that the electronic coupling between the QD and the substrate and between the QD and the STM tip is weak. In the initial configuration where no bias is applied between tip and substrate, the Fermi-levels of the tip and substrate are in the gap of the QD: no electrons (holes) tunnel through the QD (figure 2.5 A). The discrete energy levels of the QD are presented as horizontal lines, the valence levels are filled with electrons (vertical arrows), the conduc-

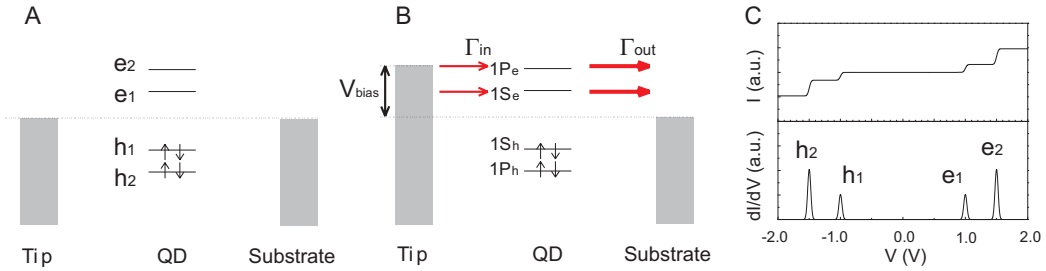

Figure 2.5: Schematic representation of the principles of STS in the shell-tunneling regime in a DBTJ (A) no applied bias between tip and substrate (B) positive applied bias resulting in tunneling of electrons through the energy levels of the QD. (C) Spectrum resulting from STS with two resonances at positive bias (conduction levels) and negative bias (valence levels) separated by the bandgap of the semiconductor, $\eta = 1$.

tion levels are empty. When the Fermi-level (E_F) of the tip or substrate aligns with one of the energy levels of the QD (by applying a bias over the DBTJ), a tunnelling channel opens up, resulting in resonant electron (hole) tunneling from the tip to the QD and from the QD to the substrate, or vice versa (figure 2.5 B). In the measured spectra, a stepwise increase in the current *I* and peaks in the tunnelling conductance ($\mathrm{d}I/\mathrm{d}V_{bias}$) are observed (figure 2.5 C). On individual QDs the resonances from tunneling through valence energy levels (negative bias) and conductance energy levels (positive bias) are separated by a zero-conductance gap which is directly related to the single-particle gap (figure 1.3). At positive bias the resonances are denoted e_1 and e_2 and at negative bias h_1 and h_2 and correspond to electron and hole-states respectively.

Resonant tunneling spectra depend sensitively on whether a carrier (electron or hole) tunnels through an empty QD where interelectronic interactions are absent or whether carriers accumulate inside the dot and experience Coulomb repulsion. This depends on the dynamics of electron tunneling into and out of the QD.[17,20–23] Figure 2.5B shows the tunnelling rate into (Γ_{in}) and out of (Γ_{out}) the QD, represented as arrows. The tunneling rate of electrons into the QD is lower than the tunneling rate out of the QD ($\Gamma_{in} << \Gamma_{out}$) resulting in no more than one added electron (hole) in the QD at a time. This regime is called shell-tunnelling regime (figure 2.5) and can be reached for example by increasing the tip-dot distance. In this regime, the potential distribution over the double-barrier tunnelling junction is asymmetric and most of the potential drops between tip and dot ($\eta \sim 1$).

The electron occupancy of the lowest unoccupied molecular orbital (LUMO) e_1 of the QD is:[22]

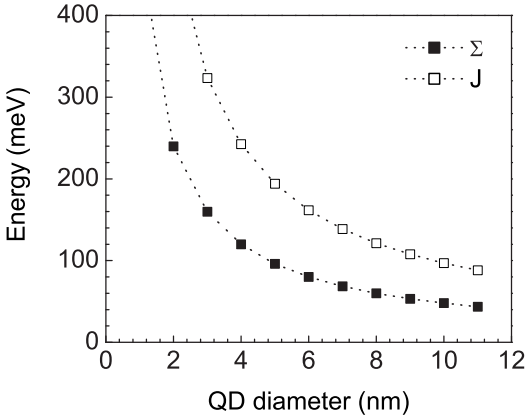

Figure 2.6: Calculated polarization energy and electron-electron repulsion energy for a PbSe QD of different diameters with $\varepsilon_{in} = 227$ and $\epsilon_{out} = 3$.

$$P_{e_1} = \frac{2\Gamma_{in}}{2\Gamma_{in} + \Gamma_{out}} \tag{2.4}$$

where Γ_{in} is the rate at which an electron tunnels from the tip into the empty first resonance orbital and Γ_{out} is the tunneling rate from the occupied orbital into the substrate electrode. In shell-tunneling $P_{e_1} \sim 0$ and only one electron tunnels through the dot at a time. Tunneling of a single electron through an energy level e_i ($e.g.\ i = 1$) leads to polarization of the QD. Thus, the peaks (resonances) in the tunneling spectrum are related to the energy levels E_i through:

$$\eta V_{bias} = E_{e_i} + \Sigma_{e_i} \tag{2.5}$$

where Σ_i is the polarization energy, the electrostatic energy needed to add one electron on level e_i. When the electrochemical potential (bias) of the tip is further increased, (figure 2.5 B), tunneling from the tip to the higher energy levels e_2 and e_3 occurs.

Tunneling of a single hole (at negative bias) through an energy level also leads to polarization of the QD (polarization energy Σ_i). Thus, the bias voltage at resonance in the tunneling spectrum at negative bias is related to the energy levels E_i through:

$$\eta V_{bias} = E_{h_i} - \Sigma_{h_i} \tag{2.6}$$

The polarization energy Σ_i depends on the dielectric mismatch between the QD core and its surroundings and can be estimated with the effective mass approximation (assuming S-type wavefunction) given the dielectric constant of the quantum dot, ε_{in} and the effective value for the environment ε_{out}:[24–26]

$$\Sigma = \frac{1}{2}\frac{e^2}{4\pi\varepsilon_0 R}\left(\frac{1}{\varepsilon_{out}} - \frac{1}{\varepsilon_{in}}\right) + \frac{0.47e^2}{4\pi\varepsilon_0\varepsilon_{in}R}\left(\frac{\varepsilon_{in}-\varepsilon_{out}}{\varepsilon_{in}+\varepsilon_{out}}\right) \tag{2.7}$$

where R is the radius of the QD. For PbSe QDs, the polarization energy varies between 160 mV and 48 mV for dot diameters between 3 and 10 nm, respectively, with $\varepsilon_{out} = 3$ (figure 2.6). The zero-conductance gap in the tunneling spectrum is then related to the quasi-particle gap (band gap) by the separation between the electron and hole resonances ($E_{e_1} - E_{h_1}$) and the polarization energy (Σ) as:

$$E_g^{qp} = \eta V_{zc}^{STM} = E_{e_1} - E_{h_1} + \Sigma_{e_1} + \Sigma_{h_1} \tag{2.8}$$

where V_{zc}^{STM} is the zero-conductance gap in the tunneling spectra. As electron-electron interactions are absent in the shell-tunneling regime, the measured $\mathrm{d}I/\mathrm{d}V$ spectra directly reflect the LDOS of the QD.

2.3.4 Shell-filling spectroscopy

In shell-filling spectroscopy (figure 2.7), the tunneling rate of electrons into the QD is higher than the tunneling rate out of the QD, $\Gamma_{in} >> \Gamma_{out}$. This can be obtained by e.g. decreasing the tip-dot distance and/or increasing the dot-substrate distance. More than one added electron (hole) at a time is present in the QD. The degeneracy of the energy levels is lifted due to interactions (J) between the carriers (electrons/holes) accumulating in the dot. At zero bias (figure 2.7A), no electrons (holes) tunnel through the QD. As the bias voltage is increased and $\Gamma_{in} >> \Gamma_{out}$, two electrons can occupy the first non-degenerate level e_1, one spin up and one spin down leading to splitting of the first resonance (figure 2.7B, the energy levels of the QD are presented as horizontal lines). At larger bias voltage, the three-fold degenerate level e_2 is filled. The spectrum reflected in figure 2.7C shows the first non-degenerate level e_1 represented by two peaks separated by J_{e_1,e_1} and the second three-fold degenerate levels (six-fold if spin is taken into account) is observed. As in the shell-tunneling regime, the energy of the first resonance is related to the applied bias according to equations 2.5 and 2.6. However, addition of the second electron in the same energy levels leads to electron-electron repulsion and the bias voltage is related to the energy levels through: $\eta\, V_{bias} = E_{e_1} + \Sigma_{e_1} + J_{e,e}$. Adding a third electron into the QD in e_2 gives (neglecting exchange energy):[27] $\eta\, V_{bias} = E_{e_2} + \Sigma_{e_2} + 2J_{e,e}$.

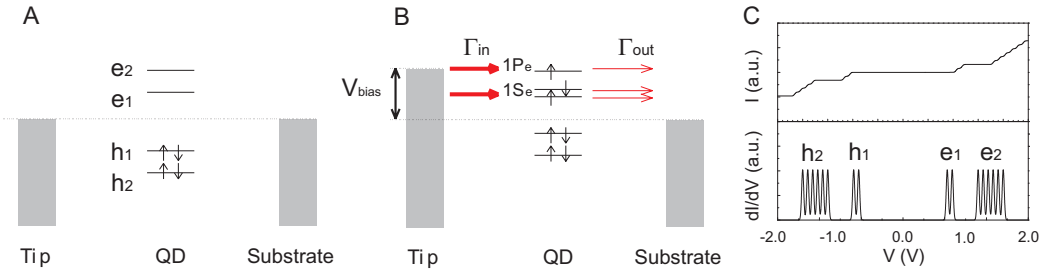

Figure 2.7: Schematic representation of the principles of STS in a DBTJ in the shell-filling regime (A) no applied bias between tip and substrate (B) positive applied bias resulting in tunneling of electrons through the energy levels of the QD, the tunneling rate into the QD is larger than out of the QD resulting in accumulation of electrons. (C) Resulting shell-filling spectrum from tunneling through the QD with $\frac{\Gamma_{in}}{\Gamma_{out}} = 4$.

The polarization energy and electron-electron (hole-hole) repulsion depend on the dielectric constant of the nanocrystal material, ε_{in}, and the (effective) dielectric constant of the surroundings, ε_{out}.[25,27] The electron-electron repulsion can be estimated as:

$$J = \frac{e^2}{4\pi\varepsilon_0 R}\left(\frac{1}{\varepsilon_{out}} + \frac{0.79}{\varepsilon_{in}}\right) \tag{2.9}$$

where R is the QD radius. J is calculated for a PbSe QD with different diameters (figure 2.6). The electron-electron repulsion energy varies between 323 mV and 97 mV for dot diameters between 3 and 10 nm respectively. For QDs with high dielectric constant like PbSe, $J \simeq 2\Sigma$.

2.3.5 Electron or hole transport on both sides of the zero-conductance gap

When the QDs are weakly coupled to the substrate, a more symmetric potential distribution over the DBTJ, $\eta \approx 0.5$ is possible. In that case, it is possible that tunnelling of electrons (holes) occurs on both sides of the zero-conductivity gap.[24] The experimentally observed zero-conductivity gap $\Delta(V_{gap}^{STM})$ is no longer related to the separation between the first conduction and valence levels but in the case of electrons tunneling on both sides of the gap is given by:

$$\Delta(V_{gap}^{STM}) = \frac{1}{\eta(1-\eta)}(E_{e_1} + \Sigma_{e_1} - E_F) \tag{2.10}$$

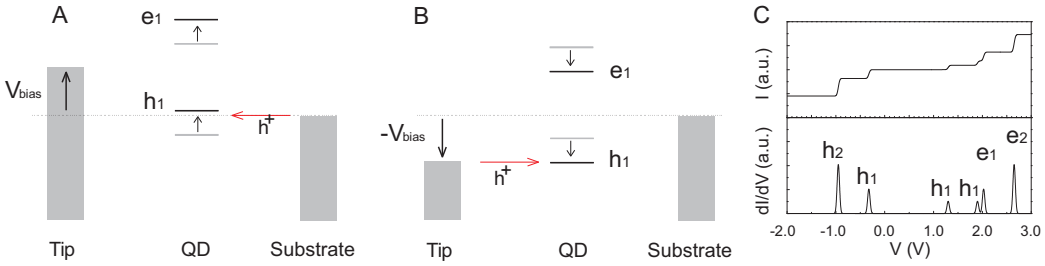

Figure 2.8: . Schematic representation of the principles of STS in a DBTJ, where holes tunnel on both sides of the gap (A) The Fermi level at equilibrium is indicated by the dashed line, the valence (hole) levels, gray lines, lie closer to the equilibrium of the Fermi-level. At positive bias, before the Fermi-level of the tip reaches the first resonance e_1, a channel opens up through the valence (hole) levels, black line. (B) At negative bias normal resonant tunneling through the valence levels is observed. In the schematic diagrams, the position of the Fermi level of the substrate is kept constant. (C) Tunneling spectrum; the top-trace represents the IV-spectrum and the lower trace the conductance dI/dV spectrum. At positive bias the first two resonances result from hole tunneling denoted by h_1 and h_2.

where $E_{e_1} - E_F$ is the difference between the first conduction level and the Fermi level of the tip and substrate at zero bias. If holes tunnel on both sides:

$$\Delta(V_{gap}^{STM}) = -\frac{1}{\eta(1-\eta)}(E_{h_1} - \Sigma_{h_1} - E_F) \tag{2.11}$$

In this case the experimentally observed zero-conductivity gap is much smaller than $E_{e_1} - E_{h_1}$ which may result in misleading information on the single-particle gap. There is concomitant electron and hole tunneling, electrons (holes) tunnel on both sides of the zero-conductivity gap if the junction is symmetric ($\eta \sim 0.5$) and/or when the conduction or valence levels (gray lines) lie close to the Fermi level E_F. If a bias is applied between tip and substrate, the energy levels of the QD will shift (black horizontal lines in figure 2.8A and B) with respect to the position of the Fermi level of the substrate which is kept constant. Figure 2.8C shows the results of a simulation where the valence levels lie closer to the Fermi level. When a negative bias is applied over the DBTJ (figure 2.8A), the first two resonances occurring in the spectrum in figure 2.8C result from holes tunneling through the valence levels. The top curve shows the IV-spectrum and the lower curve shows the conductance spectrum dI/dV. At positive bias (figure 2.8B), the valence level h_1 is observed as a doublet: the two peaks in the spectrum result from shell-filling spectroscopy, holes accumulate in the QD. At larger bias, resonances of the conduction levels are observed. The complete spectrum has shifted to the right (positive bias). Electron and hole transport through the QD can occur simultaneously at higher bias, which can

lead to electron-hole recombination and may give rise to single-photon emission. When experimentally complicated spectra are observed that do not fit in the schemes of 'simple' shell-tunneling or shell-filling spectroscopy, concomitant electron and hole tunneling should be considered as a possible explanation.

2.3.6 Linewidth of resonances in STS

At a temperature $T \rightarrow 0$ K the conductance scanning tunneling spectra show discrete peaks (delta-functions) with a spectral linewidth that should be defined by the Heisenberg uncertainty relation $\Delta E \Delta t \geq \hbar/2$ where Δt is the lifetime of the tunneling electron in the QD. For typical tunneling rates in STM/STS (on the order of $1{\cdot}10^8 \mathrm{s}^{-1}$) the linewidth ($\Delta E$) should be smaller than 1μeV. At low temperatures, the Fermi-Dirac distribution is a step function and resonant electron transfer only occurs at resonance with an energy level of the QD. As the temperature increases, the transition regime between fully occupied and empty energy levels in the tip and substrate has a width of $\sim 2k_B T$. Spectroscopy at 5 K would then result in an extra broadening of the resonances of $\sim$1 meV.

A phenomenon that is not well understood in scanning tunneling spectroscopy is the line shape and the considerable linewidth ($\sim$100 meV) of the resonances in the experimentally obtained spectra, which are much broader than anticipated from the uncertainty relation or from the Fermi-broadening at $T > 0$ K. The additional broadening of the line-width observed in STS experiments must be due to other factors such as electron-phonon coupling, charge and dipole fluctuations in the close environment of the QDs, mechanical oscillations of the QD in the tunneling junction, electrical noise from the STM and/or internal heating by non-resonant electron transport.

Considerable effort has been made to investigate the different factors involved in linewidth broadening.[28] We have performed a large number of spectroscopy experiments on CdSe QDs and compared them to theoretical calculations, it follows that electron-phonon coupling forms the main contribution to broadening of the peaks in the tunneling spectra. The fluctuations in the current caused by fluctuations of the charge around the QD is responsible for an additional broadening of the peaks and it was shown that internal heating due to the non-resonant tunneling is not important.

The results of the study mentioned above are important for the scanning tunneling experiments on PbSe QDs which are discussed in chapter 3. However, beside the impact of electron-phonon coupling and current fluctuations around the QD on the linewidth and shape of the resonances, for PbSe QDs there is an additional source of broadening outlined below. In PbSe QDs, the fundamental gap is at the L-point of the Brillouin zone and hence 4-fold degenerate.[29,30] But, the different valleys in the Brillouin zone are coupled

(intervalley coupling), and this lifts the 4-fold degeneracy of the S-states for electrons and holes. The splitting of the energy levels depends on the size of the crystal and is larger for smaller QDs. Tight-binding and pseudopotential calculations predict splittings in the order of a few tens of meV depending on the size of the QDs. The lifting of the degeneracy is seen as a peak broadening in the tunneling spectra.

References

[1] Griffiths, D.J. "Introduction to quantum mechanics" - 3rd ed. Prentice Hall, New Jersy, 1999.

[2] Binnig, G.; Rohrer, H. "Scanning tunneling microscopy-from birth to adolescence" Rev. of Mod. Phys. 1987, 59, 615-625.

[3] Binnig, G.; Rohrer, H.; Gerber, C.; Weibel, E. "7 x 7 reconstruction on Si(111) resolved in real space" Phys. Rev. Lett. 1983, 50, 120-123.

[4] Binnig, G.; Rohrer, H.; Gerber, C.; Weibel, E. "Surface studies by scanning tunneling microscopy" Phys. Rev. Lett. 1982, 49, 57-61.

[5] Eigler, D. M.; Schweizer, E. K. "Positioning single atoms with a scanning tunneling microscope" Nature 1990, 344, 524-526.

[6] Stroscio, J. A.; Eigler, D. M. "Atomic and molecular manipulation with the scanning tunnling microscope" Science 1991, 254, 1319-1326.

[7] Lee, H. J.; Ho, W. "Single-bond formation and characterization with a scanning tunneling microscope" Science 1999, 286, 1719-1724.

[8] Binnig, G.; Rohrer, H.; Gerber, C.; Weibel, E. "Tunneling through a controllable vacuum gap" Appl. Phys. Lett. 1982, 40, 178-180.

[9] Bardeen, J. "Tunneling from a many-particle point of view" Phys. Rev. Lett. 1961, 6, 57-59.

[10] Harrison, W.A. "Tunneling from an independent-particle point of view" Phys. Rev. 1961, 123, 85-89.

[11] Tersoff, J.; Hamann, D.R. "Theory and application for the scanning tunneling microscope" Phys. Rev. Lett. 1983, 50, 1998-2001.

[12] Tersoff, J.; Hamann, D.R. "Theory of the scanning tunneling microscope" Phys. Rev. B 1985, 31, 805-813.

[13] Hansma, P.K.; Tersoff, J. "Scanning tunneling microscopy" J. Appl. Phys. 1986, 61, R1-R23.

[14] Bar-Sadeh, E.; Goldstein, Y.; Zhang, C.; Deng, H.; Abeles, B.; Millo, O. "Single electron tunneling effect in granular metal films" 1994, 50, 8961-9864.

[15] Dorogi, M.; Gomez, J.; Osifchin, R.; Andres, R. P.; Reifenberger, R. "Room-temperature coulomb blockade from a self-assembled molecular nanostructure" Phys. Rev. B 1995, 52, 9071-9077.

[16] Andres, R.P.; Bein, T.; Dorogi, M.; Feng, S.; Henderson, J.I.; Kubiak, C.P.; Mahoney, W.; Osifchin, R.G.; Reifenberger, R. "Coulomb staircase at room-temperature in a self-assembled molecular nanostructure" Science 1996, 272, 1323-1325.

[17] Bakkers, E.P.A.M.; Vanmaekelbergh, D. "Resonant electron tunneling through semiconducting nanocrystals in a symmetrical and an asymmetrical junction" Phys. Rev. B 2000, 62, R7743-R7746.

[18] Banin, U.; Cao, Y.; Katz, D.; Millo, O. "Identification of atomic-like electronic states in indium arsenide nanocrystal quantum dots" Nature 1999, 400, 542-544.

[19] Millo, O.; Katz, D.; Cao, Y.; Banin, U. "Scanning tunneling spectroscopy of InAs nanocrystal quantum dots" Phys. Rev. B 2000, 61, 16773-16777.

[20] Banin, U.; Millo, O. "Tunneling and optical spectroscopy of semiconductor nanocrystals" Annu. Rev. Phys. Chem. 2003, 54, 465-492.

[21] Jdira, L.; Liljeroth, P.; Stoffels, E.; Vanmaekelbergh, D.; Speller, S. Size-dependent single-particle energy levels and interparticle Coulomb interactions in CdSe quantum dots measured by scanning tunneling spectroscopy Phys. Rev. B 2006, 73, 115305/1-6.

[22] Bakkers, E. P. A. M.; Hens, Z.; Zunger, A.; Franceschetti, A.; Kouwenhoven, L. P.; Gurevich, L.; Vanmaekelbergh, D. "Shell-tunneling spectroscopy of the single-particle energy levels of insulating quantum dots" Nano Lett. 2001, 1, 551-556.

[23] Averin, D.V.; Korotov, A.N.; Likharev, K.K. "Theory of single-electron charging of quantum wells and dots" Phys. Rev. B 1991, 44, 6199-6211.

[24] Niquet, Y.M., Delerue, C., Allan, G., Lannoo, M. "Interpretation and theory of tunneling experiments on single nanostructures" Phys. Rev. B 2002, 65, 165334/1-14.

[25] Lannoo, M.; Delerue, C.; Allan, G. "Screening in semicondcutor nanocrystallites and its consequences for porous silicon" Phys. Rev. Lett. 1995, 74, 3415-3418.

[26] Delerue, C.; Lannoo, M. "Nanostructures, theory and modelling" Springer-Verlag, Berlin, 2004.

[27] Franceschetti, A.; Williamson, A.; Zunger, A. "Addition spectra of quantum dots: the role of dielectric mismatch" J. Phys. Chem. B 2000, 104, 3398-3401.

[28] Jdira, L.; Overgaag, K.; Stiufiuc, R.; Grandidier, B.; Delerue, C.; Speller, S.; Vanmaekelbergh, D. "Linewidth of resonances in scanning tunneling spectroscopy" Phys. Rev. B 2008, 77, 205308/1-11.

[29] An, J. M.; Franceschetti, A.; Dudiy, S.; Zunger, A. "The peculiar electronic structure of PbSe quantum dots" Nano Lett. 2006, 6, 2728-2735.

[30] Allan, G.; Delerue, C. "Confinement Effects in PbSe Quantum Wells and Nanocrystals" Phys. Rev. B 2004, 70, 245321/1-9.

Chapter 3

Size-dependent single-particle energy levels in PbSe semiconductor QDs measured by STS

This chapter presents a detailed investigation of the electronic properties of single PbSe quantum dots using scanning tunneling spectroscopy. The electronic density of states is explored for quantum dots of diameters between 3 and 10 nm. In this size regime, quantum dots show strong quantum confinement effects resulting in an increase of the measured gap and energy spacing between energy levels with decreasing size of the quantum dot. State of the art tight-binding calculations confirm the size dependent spectral features. The linewidth of the peaks in the conductance spectra is investigated; for PbSe QDs larger that 5 nm most of the broadening can be attributed to electron-phonon coupling while for PbSe QDs smaller than 5 nm, inter-valley coupling is the main contributor. Finally, scanning tunneling microscopy experiments are related to optical absorption experiments and the assignment of the second and third optical transitions in absorption spectra is discussed.

3.1 Introduction

In recent years, the interest in optical, electric and opto-electronic properties of semiconductor nanocrystals - often referred to as semiconductor quantum dots (QDs) - has increased considerably. Lead chalcogenides (PbS, PbSe and PbTe, IV-VI compounds) have a rock-salt lattice structure and therefore have an electronic band-structure different from that of typical II-VI compounds such as CdSe. The most striking difference is that the fundamental band gap is located at the L-point of the Brillouin zone and hence four-fold degenerate (eight-fold including spin degeneracy).[1–4] At the same time, the effect of quantum confinement is particularly strong in PbSe[5,6] as a result of the small effective mass (m^*) of the charge carriers (electrons and holes) at the L-point of the Brillouin zone ($m_h^* \approx m_e^* = 0.05$), the large bulk exciton Bohr radius (46 nm) and the high static dielectric constant (227). Related to their electronic structure and high dielectric constant, lead chalcogenide NCs possess a number of optical properties of high potential for future opto-electronic applications, such as LEDs, lasers, and solar cells.[1,5,7–10]

The electronic structure of the colloidal PbSe QDs in the regime of strong confinement has received recently much interest. Optical absorbance, luminescence, and excitation spectroscopies have been used to study in detail the dependence of the electronic structure on the nanocrystal size,[1,5,9,11,12] external pressure[13] and temperature.[9,14] The nature of the second optical transition in absorption spectra has been discussed extensively in literature,[2,9–11,14–20] but this debate has not led to an unanimous understanding of the fundamental optical properties of PbSe QDs.

Optical spectroscopy has in fact its limitations in investigating separately electron and hole energy levels, as it inherently involves transitions between two energy levels and not individual energy levels. Scanning tunneling spectroscopy (STS) does not suffer from this limitation, and has recently been used to probe the individual energy levels of semiconductor nanocrystals.[21–28] Tunneling spectroscopy is able to provide unique information on the electronic properties of the nanocrystals as it can probe the complete density of states in the absence of selection rules.

In this work we will complement previous optical experiments on PbSe QDs[12] with detailed STS experiments on individual PbSe QDs over a large size range of 3-10 nm. The tunneling spectra measured on single PbSe QDs reflect the single-electron density of states, i.e. shell-tunneling conditions prevail. The broadening of the peaks in the tunneling spectra is discussed and compared to theoretical calculations.[3,29,30] We show the relation between optical and scanning tunneling spectroscopy and discuss the nature of the optical transitions. The measured local density of states on single QDs can provide a solution for a long-standing controversy concerning the optical transitions in PbSe QDs.

3.2 Experimental details

Figure 3.1 shows a schematic representation of the sample preparation method. A flame-annealed Au(111) substrate with a self-assembled hexanedithiol monolayer[31] was immersed in a dispersion of colloidal PbSe QDs in chloroform and thoroughly rinsed to remove excess and non-covalently attached QDs. This procedure was performed in a glovebox under nitrogen atmosphere (oxygen- and water-free conditions). Details on the chemicals used can be found in appendix B. After sample preparation, the sample was inserted into the ultra high vacuum (UHV) system (appendix A) and annealed at 110°C prior to scanning tunneling microscopy (STM) experiments. This resulted in stable QDs, chemically linked to the gold substrate.

We investigated different sizes of PbSe QDs ranging from 3-10 nm (synthesized according to reference 32) were capped with oleic acid (OA) or recapped with hexylamine. The average diameter, shape and size distribution ($5-10$ %) were determined by transmission electron microscopy (TEM) and optical spectroscopy.

A low-temperature STM (Omicron Nanotechnology system) operated at 4.8 K in UHV with a base pressure of $5 \cdot 10^{-11}$ mbar was used to investigate the topography and electronic structure of single PbSe QDs. STM topography images were typically obtained at a bias of 2.5 V and set-point current of 10-40 pA. For tunneling spectroscopy (STS), the tip was positioned above a single PbSe QD and the feedback loop was disconnected. The tunneling current (I) and conductance (dI/dV), were obtained simultaneously (lock-in amplifier settings: rms modulation 6 mV at 1 kHz). The conductance spectra were also calculated by numerically differentiating the IV-curves and these were compared with spectra obtained with the lock-in amplifier. The signal-to-noise ratio was improved by using a lock-in amplifier.

Between 80 and 100 $I-V$ and $dI/dV-V$ spectra were measured on the same single QD and checked for their reproducibility. In general, the conductance spectra were very reproducible, although discrete shifts of the spectra along the voltage axis were observed in some cases. Trapping of a charge in the surroundings of the dot that acts as a local "$gate$" can lead to a shift of all the resonances. Sets of reproducible $I-V$ and $dI/dV-V$ spectra were averaged to further increase the signal to noise ratio. This did not affect the width of the peaks.

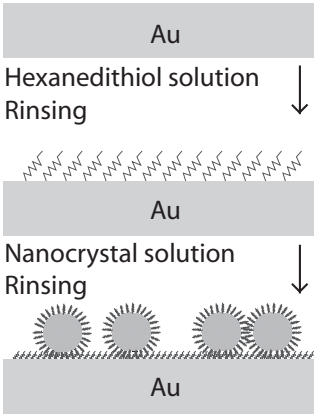

Figure 3.1: Schematic representation of sample preparation, a flame annealed Au(111) sample was immersed in a solution with hexanedithiol over night, rinsed and dried. Immersion of the sample in a dispersion of PbSe QDs results in stable attachment of the QDs on the Au(111) sample.

3.3 Results and discussion

3.3.1 Topography of PbSe quantum dots on gold

Figure 3.2A shows an example of a topography STM image of 200×200 nm^2 measured at a sample voltage V_{bias} = 2.5 V and a tunnel current $I_{setpoint}$ = 20 pA. Single PbSe QDs of diameters between 3 and 10 nm were chemically attached to a gold substrate. Control over QD concentration and immersion time of the substrate during sample preparation lead to a uniform and low coverage of individual isolated PbSe QDs over the gold substrate surface. The darker coloured background is the gold substrate and the various PbSe QDs are clearly recognized as bright dots. The QDs are well separated and have a spherical shape. Figure 3.2B shows the three height profiles of PbSe QDs on the Au(111) substrate denoted in figure 3.2A as 1,2 and 3 with sizes of 3.9, 5.6 and 6.9 nm respectively.

Four different samples with PbSe QDs of average diameters 4.0, 5.3, 7.1, and 9.8 nm (measured with TEM) were investigated with STM. Histograms of the height of the QDs measured from the STM images are shown in figure 3.2C. The upper histogram shows the STM height for QDs with TEM diameters of 5.3 and 9.8 nm and the lower histogram shows the STM height for QDs with TEM diameters of 4.0 and 7.1 nm. It is clear that the average STM height of the PbSe QDs is in good agreement with the core diameters from the TEM analysis. It should be noted that the height difference from the PbSe QDs in the topography images is not only due to the size of the PbSe QDs, as STM topography is also sensitive to electronic effects. However, due to the exponential dependence of the tunnelling current on distance (section 2.2), the measured QD heights quite accu-

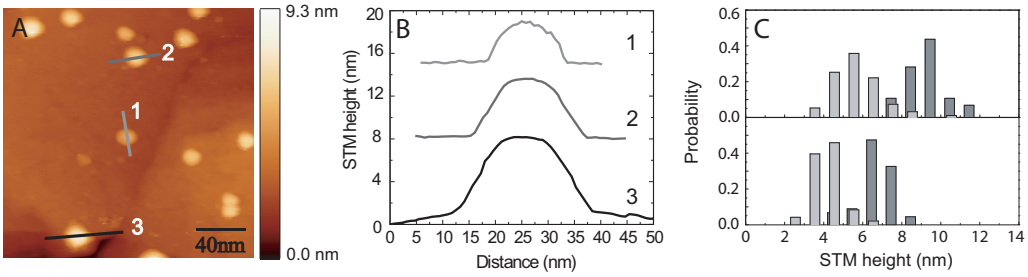

Figure 3.2: STM image of a sample with different sizes PbSe QDs chemically linked to Au(111) with hexanedithiol. (A) The topography image shows single PbSe QDs with size of 3 to 10 nm on a gold surface. Parameters $I_{setpoint} = 20\ pA$ and $V_{bias} = 2.5\ V$. (B) Three height profiles along the lines denoted in (A). (C) Histogram of the STM height extracted from topography for the four samples with TEM determined core sizes of 5.3 (light gray) and 9.8 nm (dark gray, upper histogram), and 4.0 (light gray) and 7.1 nm (dark gray).

rately reflects the true QD size. From the histograms it is also clear that individual PbSe QDs can be found with a considerable deviation from the average size. In this way we could select individual QDs of different sizes between 3 and 10 nm for resonant tunneling spectroscopy.

3.3.2 Spectroscopy on PbSe quantum dots on gold substrates

In figure 3.3, typical tunneling spectra of PbSe QD of 6.9 and 7.7 nm (STM height) are shown. The spectra show several relatively broad tunneling resonances (peaks) on both sides of the zero-conductance gap. We varied the tip-QD distance by altering the set-point current between 50 and 700 pA at a bias voltage of 1.1V and 0.8V respectively. As can be seen in figure 3.3, this did not affect the peak positions in the measured spectra; only the peak intensity is increased by decreasing the tip-QD separation (increasing set-point current). At low set-point currents (figure 3.3A lower spectrum), not all peaks are well resolved. We conclude that the conductance spectra presented in figure 3.3A and B are obtained under shell-tunneling conditions and directly reflects the single-particle density of states of the PbSe QD.[24,25,29] The peaks at negative bias voltage correspond to the first valence orbitals (hole levels) of the PbSe QDs, the peaks at positive bias voltage correspond to the conductance energy levels (electron levels).

An overview of the spectra obtained as function of size is shown in figure 3.4. All spectra show clear resonances due to tunneling through the discrete valence and conduction energy levels. We verified that the spectra were obtained in the shell-tunneling regime and hence directly reflect the energy level structure of the QDs. The spectra have been fitted with a sum of Gaussians, one for each resonance. The resonances are labeled h_1 to h_5 at

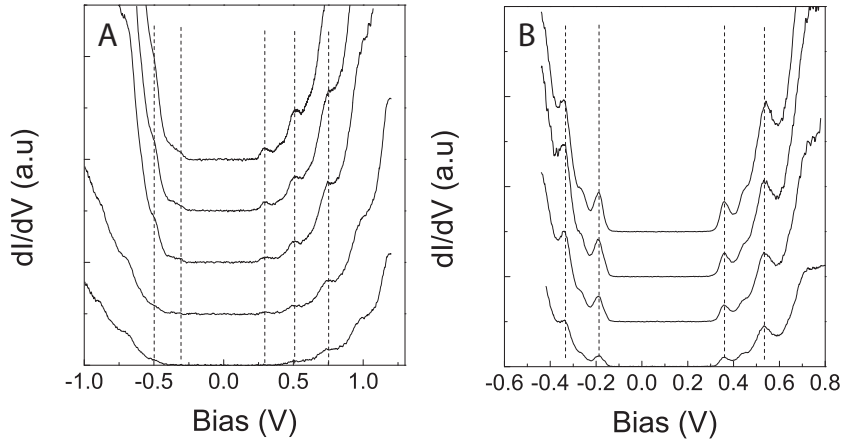

Figure 3.3: Tunneling spectrum measured at 5 K on PbSe QDs chemically linked to Au(111) with hexanedithiol (A) QD with STM height of 6.9 nm, set-point current 50, 100, 200, 300 and 400 pA at a bias voltage of 1.2 V. (B) QD with STM height of 7.7 nm, set-point current 200, 400, 550, 700 pA at a bias voltage of 0.8 V. With increasing set-point current, the peak positions do not change, only the intensity increases. At low set-point current not all peaks are well resolved. The peaks at positive bias voltage correspond to electrons tunneling through the conduction levels and the peaks at negative bias correspond to holes tunneling through the valence levels of the QD. The vertical dashed lines serve as guide to the eye.

negative bias (hole levels) and e_1 to e_5 at positive bias (electron levels). The resonances e_1 and h_1 stand for the lowest unoccupied molecular orbital (LUMO) and the highest occupied molecular orbital (HOMO), respectively, with S-type envelope symmetry. Both the zero-conductance gap ($e_1 - h_1$) and the energy level separations (e.g. e_1-e_2) increase with decreasing QD diameter (quantum confinement as discussed in section 1.2).

In order to obtain quantitative information from the tunneling spectra, the distribution of the bias voltage over the double barrier tunnel junction has to be known. We calculated this by solving the Laplace equation for a realistic tip-dot-substrate geometry as discussed in section 2.3.2. We found that for dot sizes between 3 and 10 nm $\eta = (V_{dot} - V_{tip})/V_{bias}$ is close to 0.75. The bias voltage at the resonances (peaks) in the tunneling spectrum is related to the energy levels (E_i) through $\eta V_{bias} = E_i + \Sigma_i$, where Σ_i is the polarization (charging) energy of an electron in level i. This energy depends on the energy mismatch between the QD core and its surroundings and can be estimated given the effective dielectric constant.[14,29,33,34] For QDs used in this study, the polarization energy varies between 48 (diameter 10 nm) and 160 meV (diameter 3 nm) for ϵ_{in}=227 and ϵ_{out}^{eff}=3. The zero-conductance gap in the tunneling spectrum ΔV_{zc}^{STM}, is then related to the single-particle HOMO-LUMO gap $\Delta E_{S_e-S_h}$ as follows: $\eta \Delta V_{zc}^{STM} = \Delta E_{S_e-S_h} + \Sigma_{s_e} + \Sigma_{S_h}$.

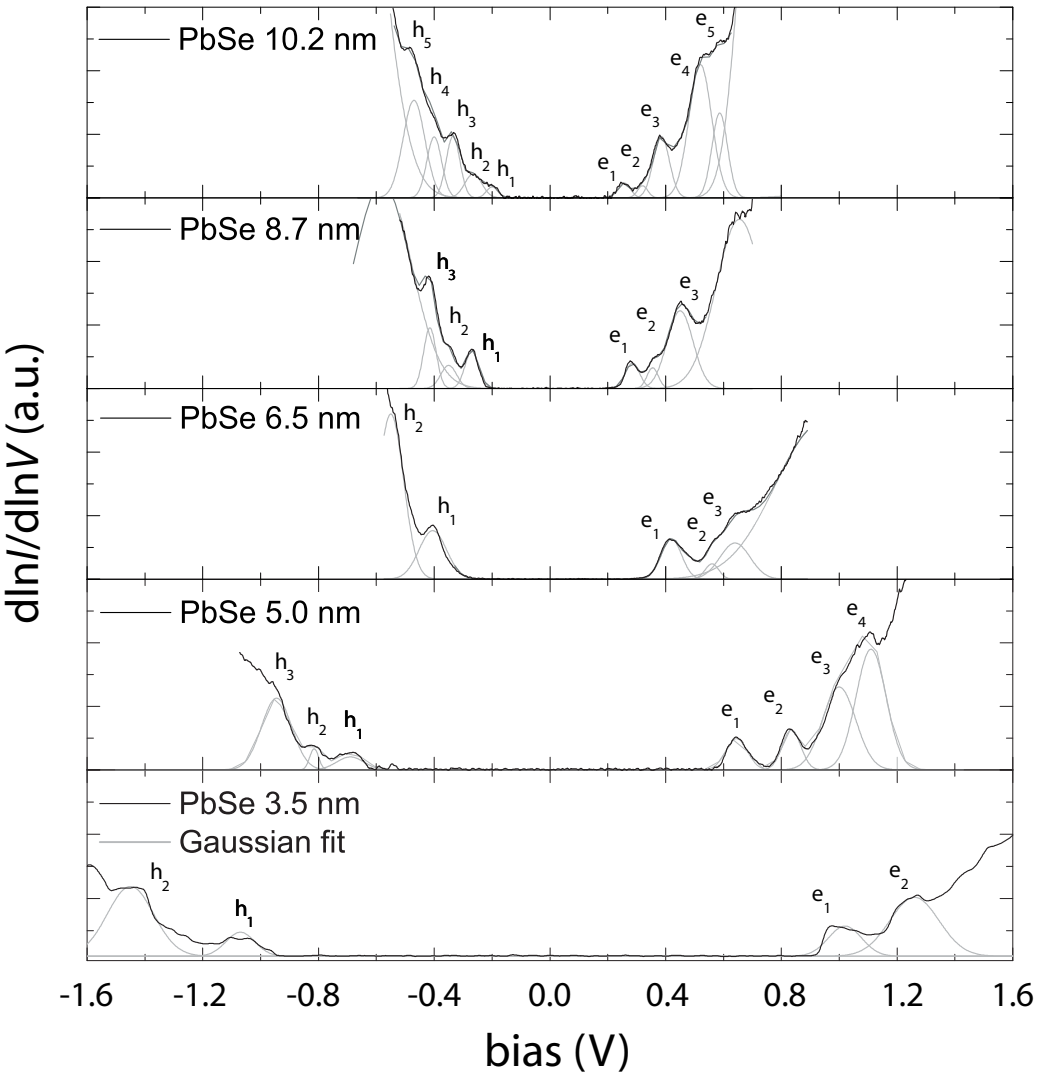

Figure 3.4: Tunneling spectrum measured at 5 K on PbSe QDs chemically linked to Au(111) with hexanedithiol for PbSe QDs with STM heights between 3.5 nm and 10.2 nm. Set-point currents 50-500 pA and bias voltage range between 0.5-1.6 V. The spectra are fitted with Gaussian distributions and the resonances are denoted h_1 to h_5 for valence levels and e_1 to e_5 for the conduction levels. The zero-conductance gap and the energy level separations (e.g. e_1 to e_2) increases as the size of the QDs is decreased from 10.2 to 3.5 nm due to quantum confinement.

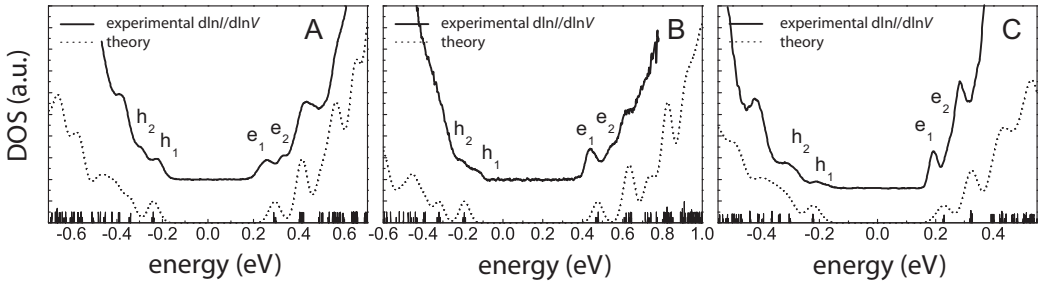

Figure 3.5: Comparison between measured dlnI/dlnV (black line) and the density of states calculated by TB (dashed lines), obtained by broadening each level (solid vertical lines) by 25 meV for different QD sizes: (A) STM height 5.8 nm, (B) 7.8 nm and (C) 9.9 nm. The TB calculations have been performed for dots with diameters of (A) 6.11 nm (B) 7.94 nm and (C) 9.77 nm; the STM spectra were converted to an energy scale using $\eta = 0.75$ and $\epsilon_{out}^{eff} = 3$. The assignment of the first two resonances (e_1, e_2, h_1 and e_2) are indicated in the figure as vertical lines.

In figure 3.5 we show $d\ln I/d\ln V$ curves proportional to the local density of states of states,[27] for three PbSe QDs with STM heights of 5.8 nm, 7.8 nm and 9.9 nm. The bias voltage has been converted to energy scale using η=0.75 and polarization energies were calculated with ε_{out}=3. Figure 3.5 also shows the energy levels calculated by tight binding (TB, dashed lines) obtained by broadening each level (vertical black lines) by a 25 meV Gaussian distribution. The TB calculations show a group of eight S-type conduction levels, followed by 24 P-type levels, and a quasicontinuum of closely spaced energy levels at higher energy. The energy spread within a group increases up to 50 meV for the S-levels due to inter valley coupling when the diameter of the QD decreases from 10 to 3 nm. The valence hole levels consist of a group of eight S-type levels, the group of P-levels is split into two. The first two resonances on each side of the STM gap (e_1, h_1 and e_2, h_2) are assigned to the S_e-, S_h- and P_e-, P_h-levels respectively. The resonances at higher energy are often considerable broader, they correspond to the group of D-levels.[4] The magnitude of the HOMO-LUMO gap ($S_e - S_h$) is in agreement with the TB calculations as was also confirmed for optical experiments on PbSe QDs;[12] however, the energy level separations between the LUMO S_e- and P_e-group and HOMO S_h- and P_h-group are overestimated by TB. We find this deviation to be systematic by inspecting a large data set. This result has implications for the assignment of the higher energy levels.

3.3.3 Hole transport on both sides of the zero-conductance gap

In a minority of the STS experiments on single PbSe QDs, we observe spectra which show transport of holes through the valence levels on both sides of the zero-conductivity gap.

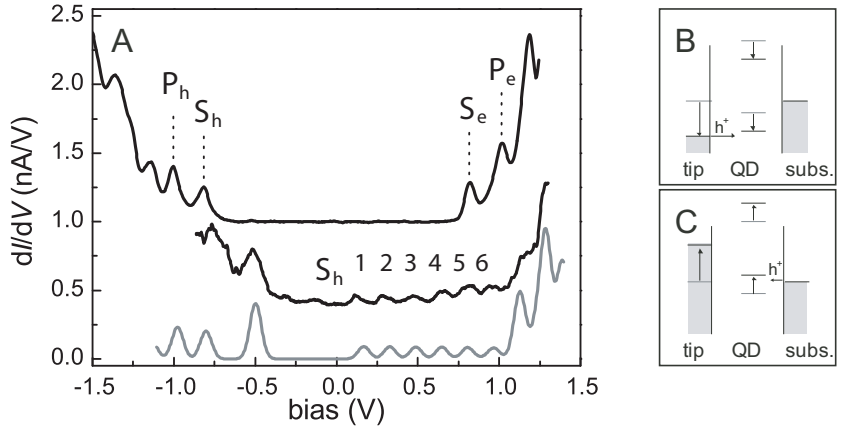

Figure 3.6: (A) Tunnelling spectroscopy of 4 nm diameter PbSe nanocrystals (black lines) and a simulated tunneling spectrum (grey line) where holes tunnel at positive bias. STS settings in both experimental spectra were bias 1.2 V and set-point 100 pA. (B) Schematics of tunnelling of holes through the S_h valence energy levels at negative bias and (C) at positive bias. In the schematic diagrams, the position of the Fermi level of the substrate is kept constant.

This requires QDs with higher lying energy levels, so that the first valence level is close to the Fermi levels (E_F) of the tip and the substrate.

Figure 3.6A shows an example of tunnelling spectroscopy on two PbSe nanocrystals with a diameter of $ca.$ 4 nm (black lines). The top spectrum is measured on a nanocrystal that exhibits a "normal" spectrum with the conduction levels appearing at positive bias and the valence levels at negative bias. This is the most common spectrum observed experimentally.[4,35] In contrast, the middle spectrum shows distinctly different behaviour: the first valence level is close to zero bias. At positive bias, there is a series of equally spaced peaks of the same amplitude. We observe this type of spectra in a significant minority of cases. These spectra can be understood by considering the schematics shown in figure 3.6B and C. At negative bias, we observe normal hole tunnelling through the valence levels. These processes occur in the shell-tunnelling regime, i.e. the tunnelling rate between the tip and the QD is much smaller than the tunnelling rate between the dot and the substrate. At positive bias, the six peak of equal intensity result also from tunneling through the valence levels. In this case however, tunneling of holes into the QD is much faster than tunneling out; i.e. the holes accumulate in the QD and occupy the 8-fold degenerate S_h-level (see section 2.3.5).

The reason for the difference between the two experimental spectra shown in figure 3.6A (black lines) could be that nanocrystals on the surface can have different binding geome-

tries that may alter the voltage distribution over them. In addition, the local environment (trapped charges etc.) can induce an electrostatic shift of all the energy levels that can vary from QD to QD. Variation of these factors can lead to the conditions required for hole tunnelling at both negative and positive bias: relatively symmetric potential distribution over the double-barrier tunnel junction and high-lying energy levels with the first valence level close to the Fermi levels of the tip and the substrate.

The higher multiplicity of the energy levels of PbSe is confirmed by our observation of six equally spaced resonances at positive bias, indicating nearly complete filling of the first, 8-fold degenerate hole level. Based on the master equation approach[29,35,36] simulations (figure 3.6A, grey line), we can extract a hole-hole interaction energy of 120 meV. There is good agreement with the calculated interaction energy for a PbSe QD of 4 nm (section 2.4). The ratio of the tunnelling rates used in the simulation was Γ_{in}/Γ_{out} = 0.1, confirming the shell-tunnelling conditions for electrons tunneling from tip to substrate. The strong increase of conductance at higher positive bias ($V_{bias} > 1$ V) is due to concomitant electron and hole tunneling. Under such conditions, electrically induced exciton luminescence from a single QD can be expected.

3.3.4 Linewidth of resonances in STS

The tunneling spectra measured on single PbSe QDs show broad resonances much larger than anticipated from temperature broadening at T=5 K or lifetime broadening, < 1 meV. We study the contribution of the different processes involved in the linewidth broadening in STS experiments. We focus on the linewidths of the first peaks/resonances on both sides of the zero-conductance gap (h_1 and e_1) as these resonances are most clearly resolved. To determine the full-width at half maximum (FWHM) of the tunneling resonances we fitted the shell-tunneling spectra with Gaussian distributions, one for each resonance (figure 3.4). As in tunneling experiments the applied bias voltage between the tip and the gold substrate does not completely drop over the tip-QD junction, the measured zero-conductance gap is always larger than the quasi particle gap by a factor $1/\eta$. Similarly to the quasi-particle gap, the width of the peaks associated with the quantized states in the QD are also broadened by a factor $1/\eta$. The FWHM of h_1 and e_1 are corrected for the potential distribution over the DBTJ (η=0.75).

Figure 3.7A and B shows the linewidths (black circles) of resonances h_1 and e_1 as a function of the PbSe QD diameter. We find that the FWHM of the conduction level increases from 24 meV to 110 meV when the diameter of the PbSe QD decreases from 10 to 3 nm. The same holds for the FWHM of the valence levels: the FWHM of h_1 increases from 23 meV to 100 meV. The linewidth of h_1 and e_1 shows a smooth increase when the QD becomes smaller. Below a diameter of 6 nm, the increase of the linewidth becomes

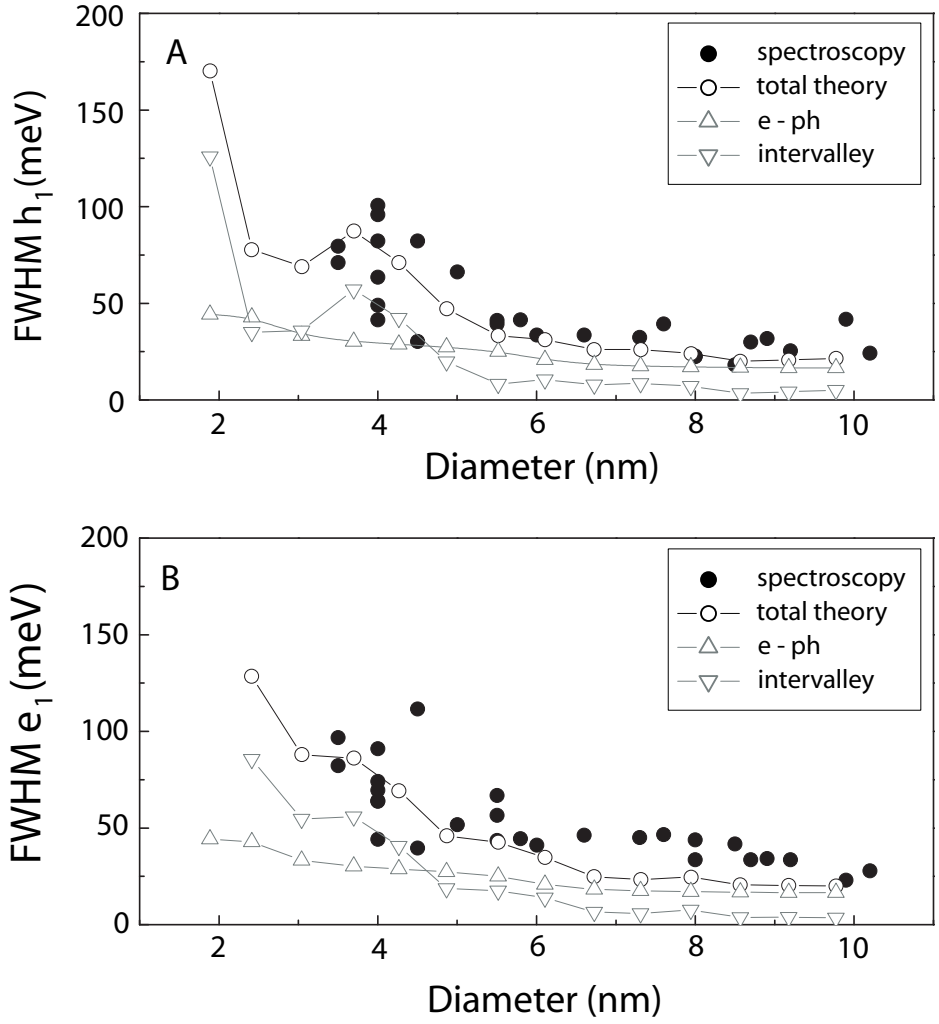

Figure 3.7: (A) and (B) FWHM of e_1 and h_1 peaks measured for PbSe QDs of different diameters (•). The FWHM is corrected for the effect of the potential distribution in the DBTJ, η=0.75. The open symbols are obtained from calculations for the width of the resonances (total FWHM ○) due to intervalley coupling (▽) and electron-phonon coupling (△).

stronger with decreasing diameter.

We have investigated in detail the contribution of different processes involved in linewidth broadening for CdSe QDs,[30] where it was found that electron-phonon coupling forms the largest contribution. The fluctuations of the current, caused by fluctuations of charges around the QD, lead to an additional broadening of the peaks. The influence of local heating due to inelastic tunneling could be neglected as increasing set-point current had no effect on the broadening of the peaks. The latter also holds for PbSe QDs as is shown in figure 3.3, where an increase in set-point current has no measurable effect on the broadening of the peaks.

In PbSe, there is an additional source of broadening of the e_1 and h_1 resonances as discussed in section 2.3.6. The fundamental bandgap of PbSe is at the L-point of the Brillouin zone, and the intervalley coupling can cause substantial splitting of the energy levels of the QD when the diameter becomes smaller. In order to determine the influence of energy level splitting due to intervalley coupling on the linewidth, the electronic structure of spherical PbSe QDs was calculated. The results are presented in figure 3.7A and B as downward triangles. The calculations were performed for QDs in the range of 3 to 10 nm. From the TB calculations, the energy level splitting (related to the FWHM of the resonances) was determined by the difference between the highest and lowest of the 4-fold degenerate energy level. In the case of spherical QDs, the linewidth e_1 increased monotonically with smaller QD sizes. The results indicate that splitting of the energy level due to intervalley coupling alone can clearly not explain the measured FWHM of the peaks.

Therefore, we also calculated the effect of electron-phonon coupling on linewidth following the procedure in reference.[30] The results are presented in figure 3.7A and B as upward triangles for valence and conduction energy levels, respectively. A gradual increase of the linewidth is predicted as the QD decreases in size. The contribution of both electron-phonon coupling and intervalley splitting are shown in figure 3.7A and B as open circles. These results can be compared to the FWHM of the resonances measured in STS. We find a strong correlation between theory and experiment indicating that the two mechanisms discussed above are the main contributions to the broadening of the resonances observed in STS experiments on PbSe QDs. The contribution of electron-phonon coupling is more pronounced for PbSe QDs larger than 5 nm and energy level splitting due to intervalley coupling is the main contribution in linewidth broadening for PbSe QDs smaller that 5 nm.

In STS experiments on CdSe QDs, the fluctuation of the current (noise) caused by fluctua-

tions of charges around the QD was found to be a second factor for linewidth broadening. In the experiments performed on PbSe QDs, the noise in the current was low and did not result in an additional broadening of the resonances. This is most probably due to the low bias voltage used in the experiments on PbSe, since the zero-conductance gap for PbSe QDs is much smaller than for CdSe dots.

3.3.5 STS versus optical absorption spectroscopy

In this section, we highlight why STM is an attractive technique to obtain detailed quantitative information on the energy level structure of semiconductor QDs. We make a comparison between optical transition energies and the energy level separations measured with STS on isolated QDs with sizes ranging between 3 and 10 nm. In both experiments, PbSe QDs from the same synthesis were used. Figure 3.8A shows an optical absorbance spectrum[12] measured on a dispersion of 6.8 nm PbSe QDs in tetrachloroethylene (TCE). To obtain quantitative information on the transitions in the absorbance spectrum, the spectrum was fitted to a sum of Gaussian distributions. Details on the fitting procedure can be found in reference 12. The absorption spectrum shows three clear excitonic transitions which are labeled α, β and γ. An extra transition which was previously not assigned in literature is the $*$-transition. This transition is weak and was reproducibly observed in the second derivative of the optical spectra.

We plot the energy of a given transition $i-j$ scaled by the confinement energy of the first transition as a function of the confinement energy of the first transition: $(\Delta E_{i-j} - E_{gap})/(\Delta E_{S_e-S_h} - E_{gap})$ versus $\Delta E_{S_e-S_h} - E_{gap}$, where E_{gap} is is the bulk bandgap of PbSe at a given temperature.[9] For the optical transitions, these scaled transition energies have been shown to be approximately temperature independent. For QDs with a high dielectric constant, the optical gap is expected to be nearly equal to the HOMO-LUMO gap.[25,33,37]

In figure 3.8B, the confinement energies of the second (β) and third (γ) optical transitions have been plotted as a function of the confinement energy of the first (α) optical transition. These are compared with energy levels derived from the resonant tunneling spectra: the $P_e - P_h$, $D_e - D_h$, and $S_e - P_h$ and $P_e - S_h$ energy levels separation (figure 3.8B •, ▲ and ■ respectively). It is evident that the second excitonic transition corresponds to the $P_e - P_h$ energy level separation measured by STS. This assignment is consistent with the expected selection rules for interband transitions in PbSe QDs.[3,15] The agreement with the third optical transition (γ) suggests that the third transition in absorption spectra involves levels of the D_e- and D_h-groups.[38]

In figure 3.8C we plot the confinement energy of the $S_e - P_h$ and $P_e - S_h$ separations

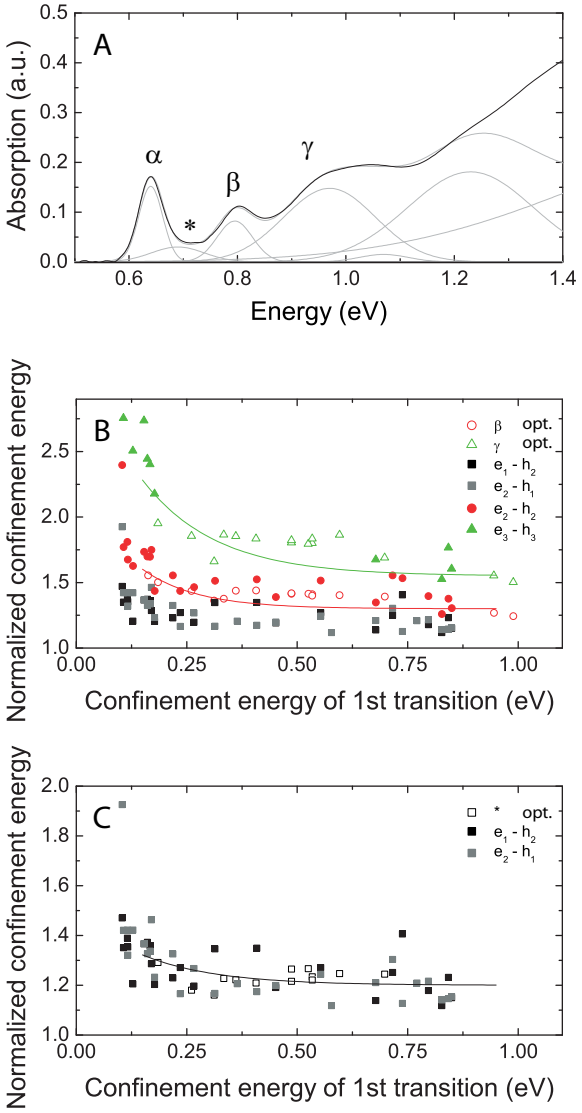

Figure 3.8: Comparison between optical absorption and scanning tunneling spectra on PbSe QDs. (A) Optical absorption spectrum of a dispersion of PbSe QDs in tetrachloroethylene (black solid line). The spectrum is fitted with a sum of Gaussians for each optical transition (gray solid lines[12]). (B) Comparison between the observed first and second optical transition and the energy level separation measured by resonant tunneling spectroscopy. Normalized confinement energy of a transition $i - j$, $(\Delta E_{i-j} - E_{gap})/(\Delta E_{e_1-h_1} - E_{gap})$ as a function of the first transition $\Delta E_{e_1-h_1} - E_{gap}$. Filled symbols from STM measurements, open symbols from optical data. (C) Normalized confinement energy of the optical $*$-transition compared to the normalized $e_1 - h_2$ and $e_2 - h_1$. Lines are drawn as guide to the eye.

derived from the tunneling spectra (■). The $S_e - P_h$ and $P_e - S_h$ separations derived from the tunneling spectra are significantly below the optical (β) transition energy. The comparison between the optical $*$-transition (□) and the $S_e - P_h$ and $P_e - S_h$ energy level separation from STS experiments (■) indicates that this less pronounced feature in the optical absorption spectrum results from the $S_e - P_h$ and $P_e - S_h$ transition. Although the $S_{e,h}$-$P_{h,e}$ transition is parity forbidden, tight binding calculations predicted a relaxation of the selection rules for PbSe QDs lacking spherical or cubic symmetry. The forbidden $S_e - P_h$ and $P_e - S_h$ gain some oscillator strength, but are still orders of magnitude weaker than the allowed $S_e - S_h$ and $P_e - P_h$ transitions. A lowering of the nanocrystal symmetry could thus explain the observed optical $*$-transition.

3.4 Conclusions

STM combines topography measurements with the possibility of carrying out electronic spectroscopy with extremely high spatial resolution. Our experiments show that STM/STS is able to provide detailed information on the electronic structure of semiconductor QDs.

We have investigated in detail the size dependence of the quantum confined levels in colloidal PbSe QDs with diameters ranging from 3-10 nm using scanning tunneling microscopy and spectroscopy. We prepared high quality samples with stable attached single PbSe QDs and determined their diameter by measuring the height profiles in the topographic images and related this to QD diameter measured by TEM. In the shell-tunneling regime, the complete single-particle density of states can be measured in the absence of selection rules. The features in the measured spectra, i.e. band-gap, groups of S_e-, S_h-, P_e- and P_h-energy levels agree semiquantitatively with TB calculations.

Occasionally we observed bipolar transport, i.e., tunneling through the same energy levels at both positive and negative bias. In addition, electron and hole transport through the QD can occur simultaneously at higher bias which may give rise to single-photon emission. Further support for the observed spectra was provided by the master equation approach by simulating the tunneling processes through a QD. The calculated spectra agree with the experimentally obtained spectra and we could extract a hole-hole interaction energy of 120 meV for a PbSe QD with a diameter of 4 nm.

We have investigated the contributions of different factors involved in the linewidth broadening of the resonance associated with the single-particle S_e-level. The measurements revealed that the linewidth of the resonances in STS experiments increases as the QDs become smaller. Theoretical calculations showed that the two main contributions to the linewidth measured in STS experiments on PbSe QDs result from electron-phonon cou-

pling and intervalley splitting. For PbSe QDs smaller than 5 nm, the main contribution results from intervalley splitting whereas for PbSe QDs smaller than 5 nm, electron-phonon coupling gives the main contribution.

The STS experiments have also been used to reappraise the optical absorbance spectra of PbSe NCs: the second transition (β-transition) in the optical absorbance spectrum can be assigned to the allowed transitions between the group of conduction and valence levels with P-type symmetry. Furthermore, a transition which was previously not assigned in literature, the $*$-transition, can be assigned to the parity forbidden $S_e - P_h$ and $P_e - S_h$ transition.

This work highlights the possibilities offered by STM in measuring the complete density of states function, in the absence of selection rules, of individual QDs over a large size range and relating it to the simultaneously measured geometry.

References

[1] Wise, F.W. "Lead salt quantum dots: the limit of strong quantum confinement" Acc. Chem. Res. 2000, 33, 773-780.

[2] Andreev, A.D.; Lipovskii, A.A. "Anisotropy-induced optical transitions in PbSe and PbS spherical quantum dots" Phys. Rev. B 1999, 59, 15402-15404.

[3] Allan, G.; Delerue, C. "Confinement effects in PbSe quantum wells and nanocrystals" Phys. Rev. B 2004, 70, 245321/1-9.

[4] Liljeroth, P.; Zeijlmans van Emmichoven, P.A.; Hickey, S.G.; Weller, H; Grandidier, B.; Allan, G.; Vanmaekelbergh, D. "Density of states measured by scanning tunneling spectroscopy sheds new light on the optical transitions in PbSe nanocrystals" Phys. Rev. Lett. 2005, 95, 086801/1-4.

[5] Murray, C.B.; Sun, S.H.; Gaschler, W.; Doyle, H.; Betley, T.A.; Kagan, C.R. "Colloidal synthesis of nanocrystals and nanocrystal superlattices" IBM J. Res. Dev. 2001, 45, 47-56.

[6] Sashchiuk, A.; Amirav, L.; Bashouti, M.; Krueger, M.; Sivan, U.; Lifshitz, E. "PbSe nanocrystal assemblies: synthesis and structural, optical, and electrical characterization" Nano Lett. 2004, 4, 159-165.

[7] Schaller, R.D.; Klimov, V.I. "High Efficiency Carrier Multiplication in PbSe Nanocrystals: Implications for Solar Energy Conversion" Phys. Rev. Lett. 2004, 92, 186601/1-4.

[8] Hens, Z.; Vanmaekelbergh, D.; Kooij, E.S.; Wormeester, H.; Allan, G.; Delerue, C. "Effect of Quantum Confinement on the Dielectric Function of PbSe" Phys. Rev. Lett. 2004, 92, 026808/1-4.

[9] Wehrenberg, B.L.; Wang, C.; Guyot-Sionnest, P. "Interband and Intraband Optical Studies of PbSe Colloidal Quantum Dots" J. Phys. Chem. B 2002, 106, 10634-10640.

[10] Wehrenberg, B.L.; Guyot-Sionnest, P. "Electron and Hole Injection in PbSe Quantum Dot Films" J. Am. Chem. Soc. 2003, 125, 7806-7807.

[11] Kang, I.; Wise, F.W. "Electronic structure and optical properties of PbS and PbSe quantum dots" J. Opt. Soc. Am. B 1997, 14, 1632-1646.

[12] Koole, R.; Allan, A.; Delerue, C.; Meijerink, A; Vanmaekelbergh, D.; Houtepen, A.J. "Optical investigation of quantum confinement in PbSe nanocrystals at different points in the brilloin zone" Small 2008, 4, 127-133.

[13] Zhuravlev, K.K.; Pietryga, J.M.; Sander, R.K.; Schaller, R.D. "Optical properties of PbSe nanocrystal quantum dots under pressure" Appl. Phys. Lett. 2007, 90, 043110/1-4.

[14] Olkhovets, A.; Hsu, R.C.; Lipovskii, A.; Wise, F.W. "Size-dependent temperature variation of the energy gap in lead-salt quantum dots" Phys. Rev. Lett. 1998, 81, 3539-3542.

[15] Du, H.; Chen, C.; Krishnan, R.; Krauss, T.D.; Harbold, J.M.; Wise, F.W.; Thomas, M.G.; Silcox, J. "Optical Properties of Colloidal PbSe Nanocrystals" Nano Lett. 2002, 2, 1321-1324.

[16] Schaller, R.D.; Pietryga, J.M.; Goupalov, S.V.; Petruska, M.A.; Ivanov, S.A.; Klimov, V.I. "Breaking the phonon bottleneck in semiconductor nanocrystals via multiphonon emission induced by intrinsic nonadiabatic interactions" Phys. Rev. Lett. 2005, 95, 196401/1-4.

[17] Trinh, M.T.; Houtepen, A.J.; Schins, J.M.; Piris, J.; Siebbeles, L.D.A. "Nature of the second optical transition in PbSe nanocrystals" Nano Lett. 2008, 8, 2112-2117.

[18] Ellingson, R.J.; Beard, M.C.; Johnson, J.C., Yu, P.; Micic, O.I., Nozik, A.J.; Shabaev, A.; Efros, A.L. "Highly efficient multiple exciton generation in colloidal PbSe and PbS quantum dots" Nano Lett. 2005, 5, 865-871.

[19] An, J.M.; Franceschetti, A.; Dudly, S.V.; Zunger, A. "The peculiar electronic structure of PbSe quantum dots" Nano Lett. 2006, 6, 2728-2735.

[20] Harbold, J.M.; Du, H.; Krauss, T.D.; Cho, K.-S; Murray, C.B.; Wise, F.W. "Time-resolved intraband relaxation of strongly confined electrons and holes in colloidal PbSe nanocrystals" Phys. Rev. B 2005, 72, 195312/1-6.

[21] Banin, U.; Cao, Y.; Katz, D.; Millo, O. "Identifcation of atomic-like electronic states in indium arsenide nanocrystal quantum dots" Nature 1999, 400, 542-544.

[22] Millo, O.; Katz, D.; Cao, Y.; Banin,U. "Scanning tunneling spectroscopy of InAs nanocrystal quantum dots" Phys. Rev. B 2000, 61, 16773-16777.

[23] Millo, O.; Katz, D.; Cao, Y.; Banin, U. "Imaging and Spectroscopy of Artificial-Atom States in Core-Shell Nanocrystal Quantum Dots" Phys. Rev. Lett. 2001, 86, 5751-5754.

[24] Maltezopoulos, T.; Bolz, A.; Meyer, C.; Heyn, C.; Hansen, W.; Morgenstern, M.; Wiesendanger, R. "Wave-function mapping of InAs quantum dots by scanning tunneling spectroscopy" Phys. Rev. Lett. 2003, 91, 196804/1-4.

[25] Bakkers, E.P.A.M.; Hens, Z.; Zunger, A.; Franceschetti, A; Kouwenhoven, L.P.; Gurevich, L.; Vanmaekelbergh, D. "Shell-tunneling spectroscopy of the single-particle energy levels of insulating quantum dots" Nano Lett. 2001, 1, 551-556.

[26] Hens, Z.; Vanmaekelbergh, D.; Stoffels, E.J.A.J.; van Kempen, H. "Effects of crystal shape on the energy levels of zero-dimensional PbS quantum dots" Phys. Rev. Lett. 2002, 88, 236803/1-4.

[27] Hens, Z.; Grandidier, B.; Deresmes, D.; Allan, G.; Delerue, C.; Stiévenard, D.; Vanmaekelbergh, D. "Evolution of the density of states on going from a two- to a zero-dimensional semiconductor" Europhys. Lett. 2004, 65, 809-815.

[28] Liljeroth, P.; Zeijlmans van Emmichoven, P.A.; Hickey, S.G.; Weller, H; Grandidier, B.; Allan, G.; Vanmaekelbergh, D. "Density of states measured by scanning-tunneling spectroscopy sheds new light on the optical transitions in PbSe nanocrystals" Phys. Rev. Lett. 2005, 95, 086801/1-4.

[29] Niquet, Y.M.; Delerue, C.; Allan, G.; Lannoo, M. "Interpretation and theory of tunneling experiments on single nanostructures" Phys. Rev. B 2002, 65, 165334/1-14.

[30] Jdira, L.; Overgaag, K.; Stiufiuc, R.; Grandidier, B.; Delerue, C.; Speller, S.; Vanmaekelbergh, D. "Linewidth of resonances in scanning tunneling spectroscopy" Phys. Rev. B 2008, 77, 205308/1-11.

[31] Colvin, V.L.; Goldstein, A.N.; Alivisatos, A.P. "Semiconductor nanocrystals covalently bound to metal surfaces with self-assembled monolayers" J. Am. Chem. Soc. 1992, 114, 5221-5230.

[32] de Mello Donegá, C.; Hickey, S.G.; Wuister, S.F.; Vanmaekelbergh, D.; Meijerink, A. "Single-step synthesis to control the photoluminescence quantum yield and size dispersion of CdSe nanocrystals" J. Phys. Chem. B 2003, 107, 489-496.

[33] Delerue, C.; Lannoo, M. ”Nanostructures; theory and modelling” Springer-Verlag 2004, Berlin.

[34] Lannoo, M.; Delerue, C.; Allan, G. ”Screening in semiconductor nanocrystallites and its consequence for porous silicon” Phys. Rev. Lett. 1995, 74, 3415-3418.

[35] Liljeroth, P.; Jdira, L.; Overgaag, K.; Grandidier, B.; Speller, S.; Vanmaekelbergh, D. ”Can Scanning Tunnelling Spectroscopy Measure the Density of States of Semiconductor Quantum Dots?” Phys. Chem. Chem. Phys. 2006, 8, 3845-3850.

[36] Averin, D.V.; Korotov, A.N.; Likharev, K.K. ”Theory of single-electron charging of quantum wells and dots” Phys. Rev. B 1991, 44, 6199-6211.

[37] Franceschetti, A.; Williamson, A.; Zunger, A. ”Addition spectra of quantum dots: the role of dielectric mismatch” J. Phys. Chem. B 2000, 104, 3398-3401.

[38] Care should be taken here as the D-levels are spread over a considerable energy range and all of these levels are not expected to contribute equally to the tunnel current or to the optical transition.

Chapter 4

Individual PbSe quantum dots and molecular quantum dot aggregates stabilized in a matrix of CdSe quantum dots

The electronic local density of states (LDOS) of single PbSe quantum dots (QDs) and QD molecules is explored using low-temperature scanning tunneling microscopy (STM) and spectroscopy (STS). Both individual and molecular aggregates of PbSe QDs (dimers, trimers, . . .) are mechanically stabilized in a two-dimensional superlattice of wide band-gap CdSe QDs acting as an inert matrix. The LDOS measured at individual QDs dispersed in the matrix is identical to that of single isolated QDs chemically linked to a substrate. We investigate the degree of quantum mechanical coupling between the PbSe QDs in molecular aggregates by comparing the LDOS measured at each site in the aggregates to that of an individual PbSe QD. We observe a variable broadening of the resonances indicating a spatially dependent degree of electron delocalization in the molecular aggregates.

4.1 Introduction

Colloidal nanocrystalline quantum dots (QDs) play a key role in current nanoscience. These semiconductor nanocrystals, 1-10 nm in size, show strong quantum confinement resulting in size-tunable optical and electrical properties. There is a strong belief that such semiconductor nanocrystals will form the building blocks for QD solids with novel optical or electrical properties.[1–5] These properties will depend on the nature of the QD building blocks and the degree of electronic coupling between them. Optical and electrical spectroscopies have been used to characterize nanostructures; however, they can only measure sample-averaged properties. These techniques cannot answer an important question regarding nanostructured materials: the relation between the local atomic and electronic structure and the macroscopic (system-averaged) properties. This implies that the local interactions between the nanoscale building blocks should be measured.

This can be reached through the use of local probes, in particular scanning tunneling microscopy (STM) and spectroscopy (STS), which can measure topography and electronic structure with very high spatial resolution. The combination of STM and STS has already proved very useful in probing the geometry and electronic structure of individual atoms and molecules, and molecular aggregates at the atomic scale.[6–12] Furthermore, these techniques have been successfully used for the investigation of individual InAs, CdSe, and PbSe QDs (chapter 3),[13–17] as well as their two-dimensional arrays.[18,19]

In order to study a single, isolated QD or small aggregates of QDs with STM, they have to be immobilized on a conducting substrate. This is typically achieved using functionalized organic molecules to chemically link nanocrystal QDs to the substrate. A good control of the surface chemistry is required to get stable substrate/QD/tip junctions. Moreover, some uncertainty remains concerning the extent to which covalent linking to a conducting substrate influences the electron and hole energy levels and electron and hole charging energies of the QDs.

Here, we propose an alternative method of stabilizing individual QDs, QD molecules and larger aggregates by embedding the QDs of interest in a monolayer-matrix of wider band gap nanocrystals of about the same size. We demonstrate this approach by studying PbSe QDs embedded in a monolayer of CdSe nanocrystals where the PbSe QDs can be identified by both topographic (STM) and spectroscopic (STS) measurements. The tunneling processes that occur during resonant tunneling spectroscopy for an isolated PbSe QD chemically linked to a substrate and a QD dispersed in a matrix are shown in figure 4.1A and B, respectively. In the first case, electrons injected from the tip into the QD can only tunnel out to the substrate. On the other hand, in an array, the injected electrons can tunnel out to the substrate or to the neighboring QDs in the matrix. This has an effect

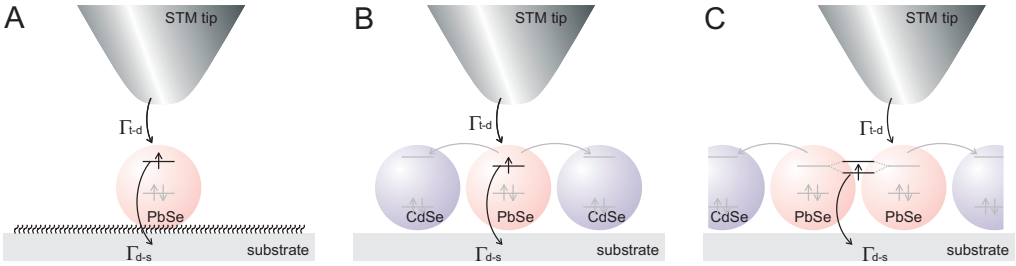

Figure 4.1: Scheme of the tunneling processes (denoted by arrows) that are possible with isolated PbSe QDs and QDs embedded in a matrix of CdSe QDs. (A) A single PbSe QD chemically linked to the substrate with hexanedithiol. (B) An isolated PbSe QD surrounded by CdSe QDs. The incoming electron can tunnel either directly or via neighboring CdSe QDs to the substrate. (C) The electronic levels in a PbSe QD dimer can be strongly coupled and the electron can delocalize over the two QDs. The subscripts t, d, s stand for tip, dot, substrate and Γ corresponds to the tunneling rate.

on the accessible regimes in tunneling spectroscopy, i.e. shell-tunneling vs. shell-filling conditions.[15,16]

As the PbSe QDs are dispersed in the CdSe monolayer, there is a distribution of monomers, dimers, and larger aggregates of PbSe QDs. This opens the possibility to study electronic interactions between the PbSe QD building blocks in small "molecules". We observe significant quantum mechanical coupling between QDs and probe this coupling at the single QD level by performing STS on the different QD sites in the molecular aggregates. This gives information on the local variations of the quantum mechanical coupling resulting from disorder. In addition, the study of these systems complements the study of more extended 2D QD arrays.[18,19]

4.2 Experimental details

The CdSe QDs served as a stabilizing matrix to investigate the electronic structure of single and aggregates of two or more PbSe QDs. The CdSe QDs were stabilized by organic ligands (TOPO and HDA) and had a core diameter of 6.1 nm.[20] We used two different sizes of PbSe quantum dots (diameters 7.1 nm and 9.8 nm) capped with oleic acid.[2,21] The average diameter, shape and size distribution ($5-10$ %) of the QDs were determined by transmission electron microscopy (TEM) and optical spectroscopy.

Two-dimensional arrays were prepared by self-assembly: CdSe and PbSe nanocrystals dispersed in chloroform were drop-casted on a flame annealed Au(111) substrate. Con-

trol over the concentration ratio CdSe:PbSe lead to monolayers of CdSe with dispersed individual PbSe QDs and also aggregates of two or more PbSe QDs.

Immediately after sample preparation (carried out under oxygen and water-free conditions), the sample was inserted into the ultra-high vacuum (UHV) system. Prior to the STM experiments, the samples were annealed in UHV up to 110°C. Low-temperature STM (LT-STM Omicron Technology) operated at T = 5 K in UHV (base pressure $5 \cdot 10^{-11}$ mbar) was used to investigate the topography and electronic structure of these self-assembled structures. We used electrochemically etched tungsten tips and the topography images were acquired in constant current mode, with typical imaging parameters being set-point current of 10 - 50 pA at a bias voltage (applied to the sample) of 2.5 V. The electronic density of states was obtained by positioning the STM tip above the center of the QD of interest and disconnecting the feedback loop. The tunnel current I was measured as a function of the bias V between the tip and the substrate. The conductance $\mathrm{d}I/\mathrm{d}V$ was measured simultaneously using a lock-in amplifier (rms modulation 10 mV at 500 Hz) or by numerically differentiating the experimental $I-V$ curves. Typically, a large number of spectra ($\sim$100) were acquired above an individual QD in the QD monolayer. In general, the measured spectra were reproducible, although discrete shifts of the spectra along the bias axis were observed in some cases. Sets of reproducible $I-V$ and $\mathrm{d}I/\mathrm{d}V$ spectra were averaged to increase the signal to noise ratio which did not affect the width of the resonances in the spectra. We carried out a detailed set of experiments on 11 monomers, 4 dimers, 2 trimers, 2 tetramers and 1 larger assembly where seven QDs were investigated.

4.3 Results and discussion

We first discuss how PbSe QDs dispersed in a CdSe matrix can be detected with STM and STS. We then present spectroscopy of the energy levels of single PbSe QDs dispersed in an inert CdSe QD matrix and finally we discuss how electronic coupling in PbSe QD "molecules" can be quantified with STS.

4.3.1 Topographic measurements of mixed PbSe and CdSe QD arrays

Figure 4.2A shows a topographic image of a self-assembled monolayer of CdSe QDs with an average diameter of 6.1 nm on a Au(111) substrate. The QD monolayers are very stable under STM imaging conditions (10-50 pA at 2.5 V). The monolayer shows local hexagonal packing, but lacks true long range order due to size, shape and orientational disorder of the CdSe QDs. Mixing CdSe and PbSe QDs with a suitable concentration ratio results in PbSe nanocrystals dispersed in a matrix of CdSe. Figure 4.2B shows an STM image of 7.1 nm PbSe QDs dispersed in a CdSe matrix at a ratio of 1:30. The diameter

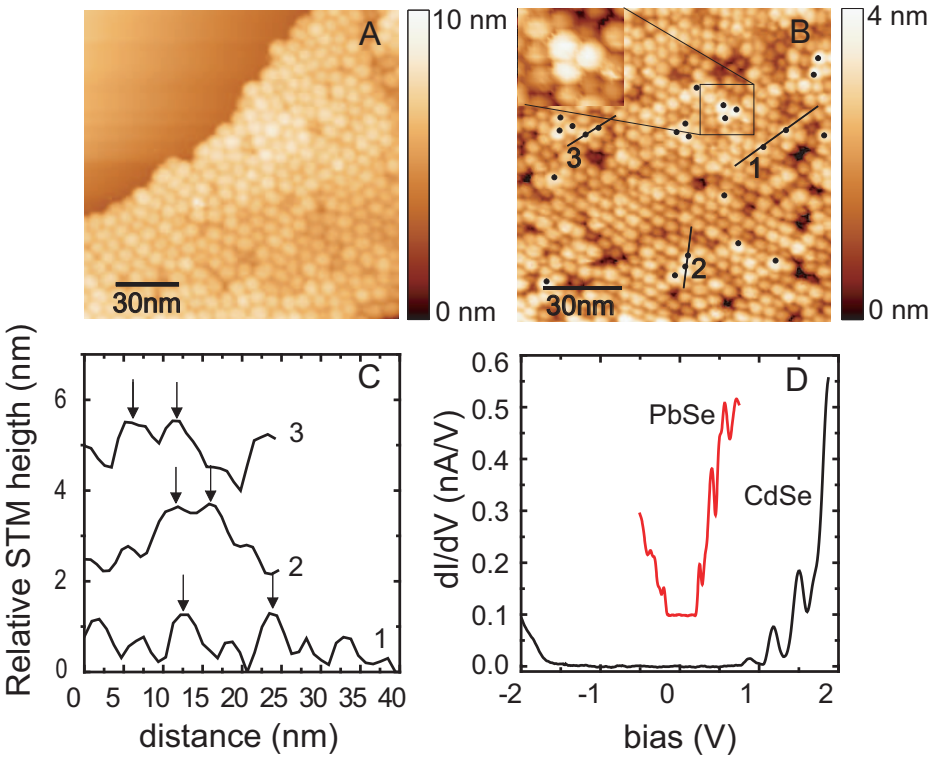

Figure 4.2: Topographic and spectroscopic identification of PbSe QDs in a CdSe QD matrix. (A) Large scale STM image of a hexagonally packed monolayer of CdSe QDs with an average diameter of 6.1 nm. Set-point current 10 pA and bias voltage 2.0 V. (B) STM image of 7.1 nm PbSe QDs marked with black circles) dispersed in a matrix of 6.1 nm CdSe QDs, set-point current 30 pA at 2.5 V. (C) Height profiles along the lines denoted in (B); arrows indicate the PbSe nanocrystals. (D) Examples of measured tunneling spectra (dI/dV vs. V) at T= 5K taken on an individual PbSe QD in a CdSe matrix (upper spectrum, off-set for clarity) and of a CdSe QD in the matrix (lower spectrum). STS feedback settings 50 pA at 0.8 V (PbSe) and 150 pA at 2.0 V (CdSe).

of individual QDs chemically linked to an Au(111) substrate can be measured $insitu$ by the STM height;[17] however this is not possible for QDs in an array. We therefore use the average diameter of the PbSe QDs determined from TEM measurements. We were able to distinguish between the two types of QDs: the PbSe QDs (indicated by black dots in figure 4.2B) appear higher than CdSe QDs. The height difference is not only due to the size difference between the different QDs because STM topography is also sensitive to electronic effects. However, due to the exponential dependence of the tunneling current on distance, the measured height difference is mostly due to the size difference between the QDs. The inset of figure 4.2B shows an aggregate of three PbSe QDs in a matrix

Table 4.1: Experimental (f_{exp}) and simulated (f_{rand}) fractions of 9.8 nm diameter PbSe QDs in monomers, dimers etc. (N_{QD}) in a matrix of 6.1 nm CdSe QDs for a PbSe:CdSe ratio of 1:10. The simulated values assume completely random assembly.

N_{QD}	f_{exp}	f_{rand}
1	0.086	0.536
2	0.064	0.266
3	0.046	0.122
4	0.033	0.054
5	0.058	0.023
6	0.038	0.008
7	0.036	0.005
8	0.020	0.001
9	0.017	0.000
10	0.026	0.000
$>$10	0.576	0.000

of CdSe QDs. Again, PbSe QDs appeared clearly higher (brighter) than the surrounding CdSe QDs. Figure 4.2C shows height profiles along the lines indicated in figure 4.2B: there is a difference of about 1 nm between the larger PbSe (indicated with arrows) and smaller CdSe QDs, which is consistent with the difference in the core sizes measured with TEM. Comparison with the pure CdSe layer indicates that the size difference is sufficiently small not to perturb the local hexagonal ordering in the array.

The PbSe and CdSe QDs also have strikingly different LDOS, in particular in terms of the band gap. This allows us to easily identify the QDs by performing tunnelling spectroscopy on them, as illustrated in figure 4.2D, where the difference in the electronic structure is apparent. For instance, the PbSe QDs have a much smaller zero-conductivity gap (related to the HOMO-LUMO band gap) than CdSe QDs. The interesting details of the electronic structure of individual PbSe QDs will be discussed in the following section.

Self-assembly of mixed QDs results in a distribution of monomers, dimers and larger aggregates of PbSe QDs in a CdSe QD matrix. We have analyzed in more detail the distribution of PbSe QDs in a series of STM images of 9.8 nm diameter PbSe QDs in a matrix of 6.1 nm CdSe QDs. Table 4.1 shows the results for a PbSe:CdSe ratio of 1:10. Comparison of the experimental and simulated (assuming completely random assembly) fractions shows that there are significant interactions between the PbSe QDs. Based on random assembly, we would expect a much larger fraction of monomers. In addition, we observe roughly half of the PbSe QDs to phase separate from the CdSe nanocrystals.

4.3.2 Spectroscopy on single PbSe QDs in a CdSe array

We studied the electronic spectra of single PbSe QDs embedded in a CdSe matrix. Figure 4.3A and B show two typical spectra obtained on single PbSe QDs with diameters of 7.1 nm and 9.8 nm embedded in a CdSe matrix. For comparison, figure 4.3C presents a spectrum acquired over an individual isolated PbSe QD chemically anchored to the substrate. The spectra measured on these individual PbSe QDs show resonances from tunneling through valence (negative bias) and conduction levels (positive bias) separated by the zero-conductance gap. As expected, the zero-conductance gap and the level separations (e.g. e_1 to e_2) decrease as the size of the QDs was increased from 7.1 to 9.8 nm. The spectra shown in figure 4.3 were acquired at low set-point currents. However, the spectra remained unaffected while decreasing the tip/QD distance. It was possible to increase the current up to 2000 pA without any changes in the energy of the resonances.

Based on this result and earlier findings,[14–16,18] we can conclude that the spectra shown in figure 4.3 are shell-tunnelling spectra, i.e. the overall tunnelling rate is limited by the tunnelling rate between the tip and the QD. In this regime, electrons tunnel through the QD one-by-one, Coulomb interactions are absent and the measured $\mathrm{d}I/\mathrm{d}V$ spectrum directly reflects the single-particle LDOS of the QD. This is different from the spectroscopy on single CdSe nanocrystals chemically linked to a Au substrate where shell-tunneling spectra evolve into (partial) shell-filling when the current is increased.[14–16,22,23] The difference can be rationalized by two effects: Due to the low effective masses of the carriers, the electronic orbitals of PbSe are more extended compared to CdSe, which results in larger tunneling coupling (tunneling rate Γ_{d-s}) between the QD and the substrate. In addition, the neighboring QDs can act as additional tunneling channels for electrons to escape. In the case of an single QD chemically linked to a substrate (figure 4.1A), the system can be described as a QD in a double barrier tunnel junction (DBTJ). This means that the injected electron (rate $\Gamma_{in} = \Gamma_{t-d}$) can only leave the QD by tunneling from the dot into the gold substrate (rate: $\Gamma_{out} = \Gamma_{d-s}$). The electron occupation is given by $\Gamma_{in}/(\Gamma_{in} + \Gamma_{out})$. It has been shown that this occupation factor can significantly differ from zero at high injection currents.[13,16] In the case of an individual QD in a matrix (figure 4.1B), the rate of electron injection remains as $\Gamma_{in} = \Gamma_{t-d}$, while the rate of electron extraction is $\Gamma_{out} = \Gamma_{d-s} + n\Gamma_{d-d}$ (n is the number of nearest neighbors). As a result, shell-filling was not observed even for high set-point currents; i.e. $\Gamma_{in} \ll \Gamma_{out}$ for all injection currents.

Another remarkable difference in microscopy of an isolated QD chemically anchored to a substrate and a PbSe QD in an array is the stability of the DBTJ. Isolated dots on a Au(111) substrate became unstable at high currents or voltages.[24] In contrast, the QDs in an array remained stable even when tunneling spectroscopy is performed at high set-point currents. The difference can be explained by the mechanisms of stabilization: in the case

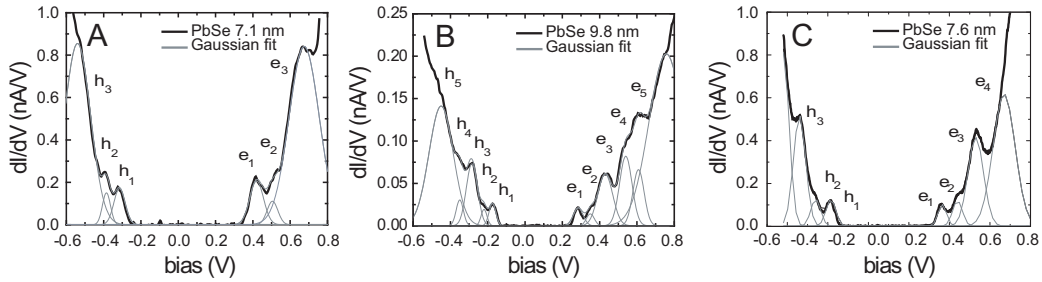

Figure 4.3: Spectroscopy on single PbSe QDs. Isolated PbSe QDs with diameters of (A) 7.1 nm and (B) 9.8 nm embedded in a CdSe QD matrix. STS settings are 200 pA, 0.8 V and 50 pA, 0.8 V, respectively. (C) Tunneling spectrum measured at 5 K on a single isolated PbSe nanocrystal (diameter 7.6 nm) chemically linked to Au(111) with hexanedithiol, set-point 200 pA and bias 0.8 V. The spectra are fitted with Gaussians and the resonances are denoted h_1 to h_5 for valence levels and e_1 to e_5 for the conduction levels. All spectra are measured at T = 5 K.

of a single dot chemically linked to the substrate, some of the chemical bonds between the QD or the substrate and the bifunctional linker molecules can be broken or weakened due to inelastic scattering of the tunneling electrons or the occupation of antibonding orbitals.[24] On the other hand, the QDs in an array are stabilized by the sum of the van der Waals interactions between the nanocrystal under the tip and its neighbors and the gold substrate; these interactions are not affected by the bias voltage or tunneling events.

The spectra in figure 4.3 have been fitted with a sum of Gaussians, one for each resonance. The resonances are labeled h_1 to h_5 at negative bias (hole levels) and e_1 to e_5 at positive bias (electron levels). The resonances e_1 and h_1 stand for the lowest electron and hole level, respectively, with S-type envelope symmetry. The widths of the resonances (corrected for the effect of the potential distribution in the DBTJ[16,22,23,25]) increase considerably with decreasing QD size (e_1: 34 meV for 9.8 nm diameter and 55 meV for 7.1 nm).

There are several factors that contribute to the energy level broadening (section 2.3.6). Temperature and life-time (controlled by the tunnelling rate out of the QD) are obvious factors; however, these both are negligibly small ($<$ 1 meV) at T = 5 K and for the experimental junction geometry. Other factors include electron-phonon coupling and local heating effects. The former involves coupling of the tunnelling electrons to either optical phonons of the nanocrystal core or vibrational modes of the capping molecules. The latter is proportional to the rate of inelastic tunnelling events. In PbSe, there is an additional source of broadening for the tunnelling resonances. The fundamental gap is at the L-point of the Brillouin zone and hence four-fold degenerate.[26,27] However, the different

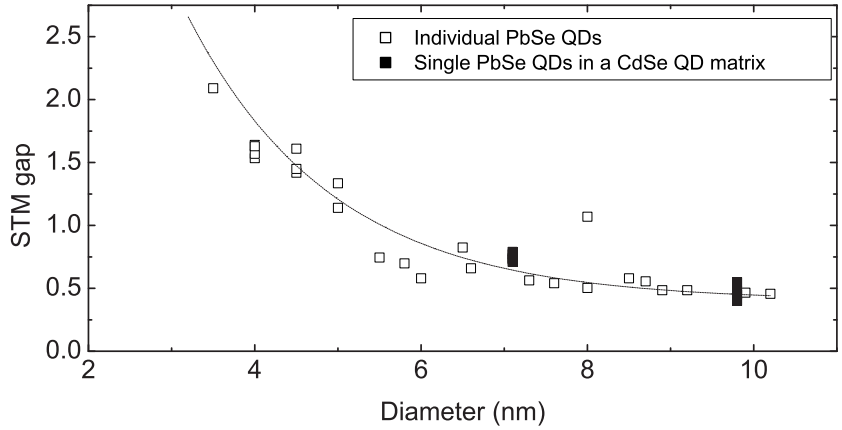

Figure 4.4: Comparison between the observed STM gap ($e_1 - h_1$) as function of PbSe QD diameter for individual QDs chemically linked to a Au(111) substrate (□) and single PbSe QDs in a CdSe matrix (■). The diameter of the individual PbSe QDs is determined from the STM height. For the single PbSe QDs in the CdSe matrix, an average diameter of the PbSe QDs is determined from TEM images.

valleys in the Brillouin zone are coupled ("inter-valley coupling") and this lifts the four-fold degeneracy of the S-states for electrons and holes and the levels split. This splitting depends on the size of the crystal and is larger for smaller nanocrystals (section 3.3.4). Tight-binding and pseudopotential calculations predict splittings in the order of a few tens of meV depending on the size of the QDs.[26,27] In tunnelling spectroscopy, the intrinsic linewidth (given by the other effects discussed above) is larger than this splitting and hence, the different S-levels cannot be observed as separate resonances.

The resonances e_3 and h_3 correspond to the P-type or D-type levels. The width of these resonances is considerably larger compared to e_1 and h_1. It is likely that the splitting of the P-levels is further increased due to the crystal dipole moment in PbSe.[21,28] It seems feasible that the weak but reproducible resonance e_2 corresponds to the lowest P-level. The spectra measured on individual PbSe nanocrystals in a CdSe matrix are very similar to the spectra measured on individual PbSe nanocrystals chemically linked to a Au(111) substrate with hexanedithiol (figure 4.3C),[17] as discussed in section 3.3.4. In both cases, we obtained consistent results on the energy level positions as well as the line-widths of the peaks in the conductance spectrum as is shown in figure 4.4. This means that tunneling coupling between the PbSe QD and the surrounding CdSe QDs is sufficiently weak not to affect the tunnelling spectra. Hence, immobilization of PbSe QDs by a CdSe QD matrix proves to be a valuable method to study individual QDs and QD molecules of interest.

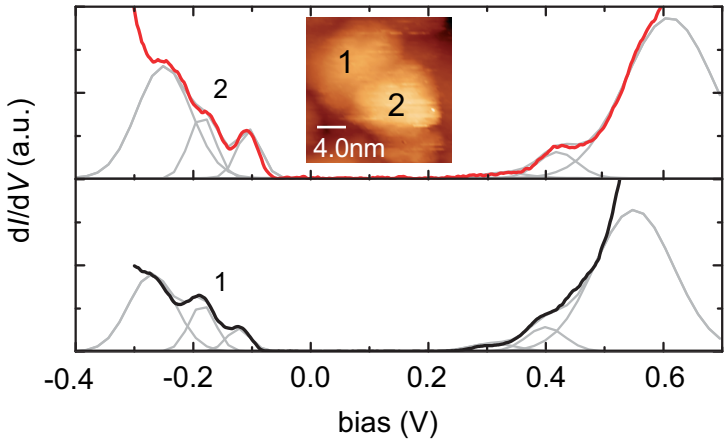

Figure 4.5: Spectroscopy on 9.8 nm PbSe dimer embedded in a CdSe matrix, The thin lines represent Gaussian distributions fitted to the resonances. Spectra measured at T= 5 K, set-point current 70 pA, bias 0.7 V (QD1) and 150 pA; 0.6 V (QD2).

4.3.3 Spectroscopy on PbSe aggregates in a CdSe array

In addition to investigating individual QDs, embedding PbSe QDs in an inert matrix allows us to study possible quantum mechanical coupling effects in small molecular aggregates of PbSe QDs stabilized in the matrix. We will focus on 9.8 nm PbSe QDs: a dimer, a chain of four and a larger aggregate of PbSe QDs as shown in the insets of figures 4.5 and 4.6. First we investigate in more detail the LDOS measured on a dimer, two neighboring QDs of 9.8 nm embedded in a CdSe matrix (figure 4.5, inset). The spectra measured on this dimer are qualitatively similar to those measured on isolated PbSe QDs: zero-conductance gap and resonances at positive and negative bias resulting from tunneling through the valence and conductance levels. The resonance energy level positions did not change for set-point currents between 50 and 600 pA and bias 0.6 to 0.8 V. The full width at half maximum (FWHM) of the resonances corresponding to the hole levels (negative bias) is 35 - 40 meV, unchanged with respect to those of individual PbSe QDs in a CdSe matrix. At positive bias however, the line-width of the first electron resonance is 70 meV for QD1 and 75 meV for QD2, hence considerably broadened with respect to that of the individual PbSe QD in a matrix (see figure 4.3B).[29] The broadening of the resonances is most likely caused by quantum mechanical interaction between PbSe QDs.[30] In a simple picture, this additional broadening of ca. 30 meV reflects the splitting of the conduction levels induced by coupling between the QDs. We use an elementary tight-binding scheme to compare the coupling in the QD dimer to the larger aggregates: the splitting of 30 meV corresponds to a value of $t_{d-d} =$ 15 meV of the QD-QD coupling matrix element.[31]

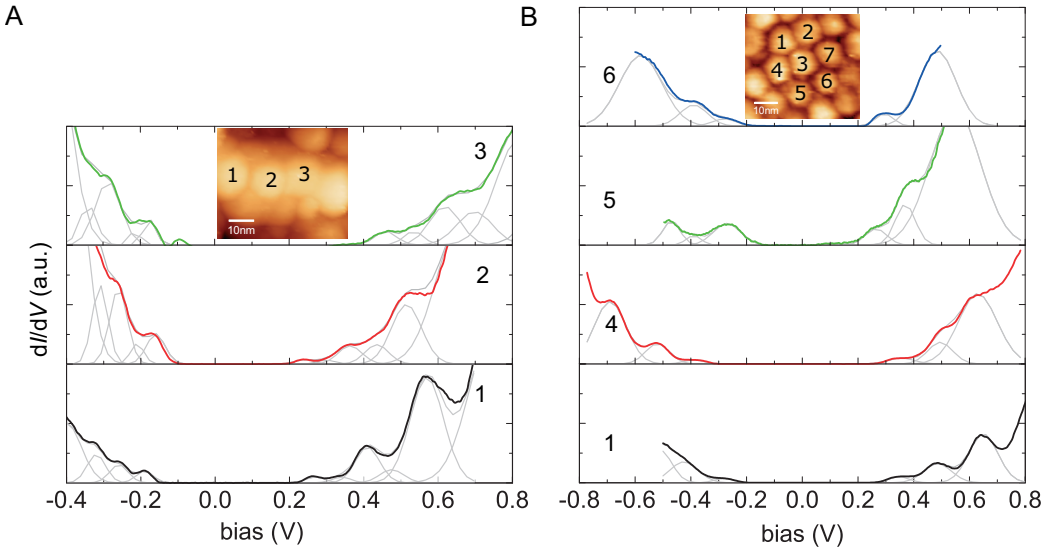

Figure 4.6: Spectroscopy on PbSe aggregates embedded in a CdSe matrix. (A) Spectra measured on three QDs on a chain of four 9.8 nm diameter PbSe QDs. The thin solid lines represent Gaussian distributions fitted to the resonances. Set-point current 100-350 pA and bias 0.7-1.8 V. (B) Representative spectra on QDs part of a larger aggregate of 9.8 nm diameter PbSe QDs. Set-point current 100-350 pA and bias 0.7-1.8 V. All spectra are measured at T= 5K.

Next we concentrate on two examples of larger aggregates of PbSe QDs shown in figure 4.6. The spectra in a linear aggregate of four PbSe QDs (figure 4.6A) show that the line width of the first electron resonance of QD 1, 2 and 3 are 53, 59 and 65 meV, respectively. This is again considerably broadened with respect to that of a single PbSe QD in an array of CdSe QDs (figure 4.3B) that has a width of 35 meV. There is an extra peak in the dI/dV spectrum 3 in figure 4.6A (at -0.17 V); the origin of this resonance is not yet clear. The feature is not visible for the other QDs in the same assembly and hence, it is not included in the fitting of the resonances. Quantum mechanical coupling in this linear chain is smaller than in the dimer shown in figure 4.5; tight-binding calculations (equal coupling between all the QDs in the chain) gives $t_{d-d} \approx 10$ meV in this case.

In addition to small aggregates, we also investigated seven neighboring PbSe QDs in the middle of a larger aggregate containing only PbSe QDs, see figure 4.6B. The PbSe QDs show a hexagonal packing, as shown in the STM topography (inset). It is clear that the spectra differ from QD to QD. Again we focus on the width of the first electron resonance; QD1: 70 meV, QD2: 94 meV, QD3: 81 meV, QD4: 88 meV QD5: 87 meV, QD6: 78 meV and QD7: 93 meV. From the above, it is clear that the electron resonances of PbSe QDs in a molecule show a variable broadening with respect to that of a single PbSe

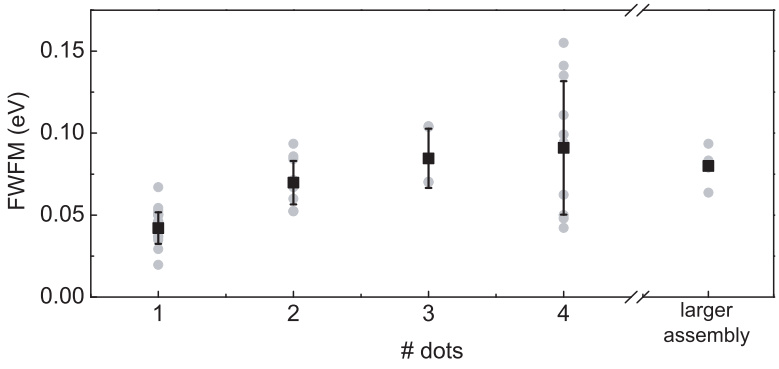

Figure 4.7: The measured FWHM (gray circles) of the tunneling resonance corresponding to the first conduction level as a function of the size of the PbSe QD aggregate. The average values with error bars (except for the larger assembly; we only have a data-set for one aggregate and hence not sufficient statistics for an error estimate) are shown by black squares.

QD. In this larger structure, we can estimate an average coupling based on tight-binding, $t_{d-d} \approx 7$ meV. This assumes an infinite system, equal coupling between the QDs, and that the peak broadening is equal to the width of the band in tight binding. In only a few cases, the resonances of the valence hole levels are additionally broadened with respect to that of a single PbSe QD (see for instance figure 4.6B QD5 and 6).

In figure 4.7 we show the measured FWHM for the first conduction level resonance for a number of monomers, dimers etc. We can make the following conclusions based on this figure: (i) the line-width increases when the number of PbSe QDs in the aggregate increases, (ii) the line-width seems to saturate at approximately 90 meV, and (iii) there is considerable spread in the measured values from QD to QD in a given aggregate and from aggregate to aggregate. While (i) and (iii) are rather obvious (more coupled QDs implies larger splitting of the levels), point (ii) gives valuable insight about the nature of coupling. It seems that the coupling strength is mainly determined by nearest-neighbor coupling and that disorder limits the size of the strongly coupled regions in larger assemblies. We can convert the measured FWHM to the QD-QD coupling matrix element t_{d-d}, and we find the following values: 14 meV for dimers, 14 meV for trimers, 12 meV for tetramers, and 6 meV for the larger assembly.

Despite electrons and holes having very similar effective masses in PbSe, we observe stronger coupling of the electron energy levels. This can be understood by considering the influence of the effective barrier height on the coupling strength: a difference of 2 eV for

the electrons and holes is sufficient to accommodate the present results.[18] In the present system, the tunneling barrier is formed by the capping ligands. The barrier height for the electrons can be defined as the energy difference between the LUMO of the capping molecules and the first conduction level of the QDs, while for the holes, it is the energy difference between the HOMO of the capping ligands and the first valence level of the QDs. Exact values for these barrier heights are unknown. However, lead chalcogenide materials are known to have low ionization potentials which makes it more likely that the barrier height for electrons is lower than for the holes.[32] This band-selective coupling is consistent with earlier obtained results on extended arrays of InAs QDs.[18,19] The variable broadening of the resonances observed from site to site indicates that the degree of quantum mechanical coupling is strongly site-dependent. It is likely that in extended arrays strong coupling only prevails over areas of a few QDs. It should be realized that colloidal nanocrystals are facetted and are hence not perfectly spherical. This leads to several types of disorder; for instance, there might be variations in the orientation of the nanocrystals with respect to each other or small variations in the distance between the facets of the neighboring nanocrystals resulting in a variable degree of electronic coupling.

4.4 Conclusions

We have shown that we can prepare PbSe QD monomers, dimers and larger islands dispersed in a matrix of CdSe QDs. Both CdSe and PbSe nanocrystals can be identified by scanning tunneling microscopy and spectroscopy. The CdSe QD array can be considered as an inert matrix stabilizing the dispersed PbSe QDs. The spectra of single PbSe QDs in the CdSe matrix are nearly identical to those of isolated PbSe QDs chemically anchored to the substrate. Small ”molecules” of PbSe QDs dispersed in the CdSe matrix can also be investigated. We observe a variable degree of electron delocalization in the small aggregates with typical coupling strengths of 10 - 20 meV. The results in this paper show that QD arrays with two different types of building blocks can be quantitatively studied. It is possible to measure the local atomic configuration together with the LDOS. This is a promising prospect for further study of ordered binary QD solids, systems that are the focus of intense current interest.[33,34]

References

[1] Redl, F.X.; Cho, K.S.; Murray, C.B.; O’Brien, S. ”Three-dimensional binary superlattices of magnetic nanocrystals and semiconductor quantum dots” Nature 2003, 423, 968-971.

[2] Murray, C.B.; Sun, S.; Gaschler, W.; Doyle, H.; Betley, T.A.; Kagan, C.R. ”Colloidal synthesis of nanocrystals and nanocrystal superlattices” IBM J. Res. Dev. 2001, 45, 47-56.

[3] Vanmaekelbergh, D.; Liljeroth, P. "Electron-conducting quantum dot solids: novel materials based on colloidal semiconductor nanocrystals" Chem. Soc. Rev. 2005, 34, 299-312.

[4] Yin, Y.; Alivisatos, A. P.; "Colloidal nanocrystal synthesis and the organic inorganic interface" Nature 2005, 437, 664-670.

[5] Murray, C.B.; Kagan, C.R. "Synthesis and characterisation of monodisperse nanocrystals and close-packed nanocrystal assemblies" Annu. Rev. Mater. Sci. 2000, 30, 545-610.

[6] Olsson, F.E.; Persson, M.; Borisov, A.G.; Garyacq, J.P.; Laqoute, J.; Fölsch, S. "Localization of the Cu(111) surface state by single Cu adatoms" Phys. Rev. Lett. 2004, 93, 206803/1-4.

[7] Repp, J.; Meyer, G.; Paavilainen, S.; Olsson, F.E.; Persson, M. "Scanning tunneling spectroscopy of Cl vacancies in NaCl films: strong electron-phonon coupling in double-barrier tunneling junctions" Phys. Rev. Lett. 2005, 95, 225503/1-4.

[8] Qiu, X.H.; Nazin, G.V.; Ho, W. "Vibronic states in single molecule electron transport" Phys. Rev. Lett. 2004, 92, 206102/1-4.

[9] Silien, C.; Pradhan, N.A.; Ho, W.; Thiry, P.A. "Influence of adsorbate-substrate interaction on the local electronic structure of C60 studied by low-temperature STM" Phys. Rev. B 2004, 69, 115434/1-5.

[10] Lu, X.; Grobis, M.; Khoo, K.H.; Louie, S.G.; Crommie, M.F. "Charge transfer and screening in individual C60 molecules on metal substrates: a scanning tunneling spectroscopy and theoretical study" Phys. Rev. B 2004, 70, 115418/1-8.

[11] Liljeroth, P.; Repp, J.; Meyer, G. "Current-induced hydrogen tautomerization and conductance switching of naphthalocyanine molecules" Science 2007, 317, 1203-1206.

[12] Venema, L.C.; Wildoer, J.W.G.; Tans, S.J.; Janssen, J.W.; Temminck Tuinstra, H.L.W.; Kouwenhoven, L.P.; Dekker, C. "Imaging electron wave functions of quantized energy levels in carbon nanotubes" Science 1999, 283, 52-55.

[13] Banin, U.; Cao, Y.; Katz, D.; Millo, O. "Identification of a atomic-like electronic states in Indium Arsenide nanocrystal quantum dots" Nature 1999, 400, 542-544.

[14] Banin, U.; Millo, O. "Tunneling and optical spectroscopy of semiconductor nanocrystals" Annu. Rev. Phys. Chem. 2003, 54, 465-492.

[15] Bakkers, E.P.A.M.; Hens, Z.; Zunger, A.; Franceschetti, A.; Kouwenhoven, L.P.; Gurevich, L.; Vanmaekelbergh, D. "Shell-tunneling spectroscopy of the single-particle energy levels of insulating quantum dots" Nano Lett. 2001, 1, 551-556.

[16] Jdira, L.; Liljeroth, P.; Stoffels, E.; Vanmaekelbergh, D.; Speller, S. "Size-dependent single-particle energy levels and interparticle coulomb interactions in CdSe quantum dots measured by scanning tunneling spectroscopy" Phys. Rev. B 2006, 73, 115305/1-6.

[17] Liljeroth, P.; Zeijlmans van Emmichoven, P.A.; Hickey, S.G.; Weller, H.; Grandidier, B.; Allan, G.; Vanmaekelbergh, D. "Density of states measured by scanning-tunneling spectroscopy sheds new light on the optical transitions in PbSe nanocrystals" Phys. Rev. Lett. 2005, 95, 086801/1-4.

[18] Liljeroth, P.; Overgaag, K.; Urbieta, A.; Grandidier, B.; Hickey, S.G.; Vanmaekelbergh, D. "Variable orbital coupling in a two-dimensional quantum-dot solid probed on a local scale" Phys. Rev. Lett. 2006, 97, 096803/1-4.

[19] Steiner, D.; Azulai, D.; Aharoni, A.; Banin, U.; Millo, O. "Level structure of InAs quantum dots in two-dimensional assemblies" Nano Lett. 2006, 6, 2201-2205.

[20] de Mello Donegá, C.; Hickey, S.G.; Wuister, S.F.; Vanmaekelbergh, D.; Meijerink, A. "Single-step synthesis to control the photoluminescence quantum yield and size dispersion of CdSe nanocrystals" J. Phys. Chem. B 2003, 107, 489-496.

[21] Houtepen, A.J.; Koole, R.; Vanmaekelbergh, D.; Meeldijk, J.; Hickey, S.G. "The hidden role of acetate in the PbSe nanocrystal synthesis" J. Am. Chem. Soc. 2006, 128, 6792-6793.

[22] Liljeroth, P.; Jdira, L.; Overgaag, K.; Grandidier, B.; Speller, S.; Vanmaekelbergh, D. "Can scanning tunnelling spectroscopy measure the density of states of semiconductor quantum dots?" Phys. Chem. Chem. Phys. 2006, 8, 3845-3850.

[23] Niquet, Y.M.; Delerue, C.; Allan, G.; Lannoo, M. "Interpretation and theory of tunneling experiments on single nanostructures" Phys. Rev. B 2002, 65, 165334/1-14.

[24] Hens, Z.; Talapin, D.V.; Weller, H.; Vanmaekelbergh, D. "Breaking and restoring a molecularly bridged metal/quantum dot junction" Appl. Phys. Lett. 2002, 81, 4245-4247.

[25] For PbSe QDs in a matrix of CdSe QDs, we estimate that $\eta = (V_{dot} - V_{tip})/V_{bias}$=0.85 based on the solution of the Laplace equation for the tip/QD/substrate configuration (section 2.3.2). This means that the bias scale can be converted to an energy scale by multiplying with 0.85.

[26] Allan, G.; Delerue, C. "Confinement effects in PbSe quantum wells and nanocrystals" Phys. Rev. B 2004, 70, 245321/1-9.

[27] An, J. M.; Franceschetti, A.; Dudiy, S.V.; Zunger, A. "The peculiar electronic structure of PbSe quantum dots" Nano Lett. 2006, 6, 2728-2735.

[28] Shevchenko, E.V.; Talapin, D.V.; Murray, C.B.; O'Brien, S. "Structural characterization of self-assembled multifunctional binary nanoparticle superlattices" J. Am. Chem. Soc. 2006, 128, 3620-3637.

[29] The fitting procedure for the dI/dV spectra of the PbSe QD aggregates started with the number and position of Gaussian peaks used to fit the spectra of isolated PbSe QDs. As there is some uncertainty in fitting the higher order resonances, we only used the first resonance in determining the coupling strength.

[30] The factors contributing to the intrinsic line-width of the transitions in the tunnelling spectra, namely strong electron-phonon coupling or local heating effects, should diminish with increasing size of the system as we discussed in section 3.3.4. Hence, they are not responsible for the broadening that we observe with the coupled PbSe QDs.

[31] Aschcroft, N.W.; Mermin, N.D. "Solid state physics" Saunders College Publishing: Fort Worth 1976.

[32] McDonald, S.A.; Konstantatos, G.; Zhang, S.; Cyr, P.W.; Klem, E.J.D.; Levina, L.; Sargent, E.H. "Solution-processed PbS quantum dot infrared photodetectors and photovoltaics" Nature Mat. 2005, 4, 138-142.

[33] Shevchenko, E.V.; Talapin, D.V.; Kotov, N.A.; O'Brien, S.; Murray, C.B. "Structural diversity in binary nanoparticle superlattices" Nature 2006, 439, 55-59.

[34] Urban, J.J.; Talapin, D.V.; Shevchenko, E.V.; Kagan, C.R.; Murray, C.B. "Synergism in binary nanocrystal superlattices leads to enhanced p-type conductivity in self-assembled PbTe/Ag_2Te thin films" Nature Mat. 2007, 6, 115-121.

Chapter 5

Variable orbital coupling in a two-dimensional quantum-dot solid probed on a local scale

The opto-electronic properties of semiconductor quantum-dot (QD) solids depend on the electronic structure of the building blocks and their interactions. Disorder may affect coupling on a local scale. We have measured the local density of states of 2D arrays of PbSe QDs site by site using scanning tunneling spectroscopy (STS). The electronic structure of PbSe QDs in an array markedly differs from that of isolated QDs due to electronic coupling in the array. We observe strong local variations in the coupling strength with two prototypical cases: delocalization of the conduction electrons only, and full coupling with both hole and electron delocalization over the QD sites in the array.

5.1 Introduction

Extended systems formed by self-assembly of colloidal semiconductor nanocrystals are often compared to solids built from ordinary atoms.[1–6] Strong confinement of electrons and holes within an isolated nanocrystal host leads to widely spaced, discrete energy levels with atomic like symmetries (S, P, etc.). Such quantum dots (QDs) can self-assemble to give extended arrays, called nanocrystal superlattices or QD solids,[2,7,8] in which the confinement of carriers can be relaxed by quantum mechanical coupling between the QDs.[4,9,10] The optical and electrical properties of these systems are determined by the electronic structure of the nanocrystal building blocks and their mutual interactions; this offers enormous versatility in the design of novel materials with tailored optical, electrical, and magnetic properties. However, unlike ordinary atoms, nanocrystal building blocks suffer from an inherent variation in their size and shape, and are furthermore faceted.[2,11] Unavoidably, there is a loss of translational and orientational order in QD solids,[12] which will cause local variations in the electronic coupling. In fact, this is very similar to ordinary glasses where the local structure strongly influences the optical and electrical properties. Macroscopic properties of QD solids, such as electronic conductivity, reflect a system average and overlook microscopic variations.[4,5,9,13,14] Hence, there is a need for measurement of the local electronic structure of the solid on the relevant length scale.

Scanning tunneling microscopy (STM) and spectroscopy (STS) can measure the density of states (DOS) at extremely high spatial resolution and they have been extensively used to measure the electronic structure of single semiconductor QDs and molecules.[15–21] Prior to the experiments presented in this chapter, in coupled arrays, only 2D superlattices of Ag nanocrystals have been studied. In that case, the 'atoms' have a high DOS at the Fermi energy; quantum mechanical coupling is revealed by the disappearance of single-electron charging (Coulomb blockade).[8,22] In contrast, semiconductor QDs in the strong confinement regime have widely spaced, discrete energy levels; quantum mechanical coupling should markedly affect the DOS. In addition, a reduction in the band gap due to electron and hole delocalization is expected. Superlattices of semiconducting PbSe QDs are good candidates for observing quantum mechanical coupling due to the low effective masses of both the electron and hole.[23–25] This leads to an increased spatial extension of the wave functions of the carriers outside the nanocrystal host, enhancing the electronic coupling between adjacent QDs.

In this chapter, we investigate the local density of states (LDOS) of 2D arrays of semiconductor PbSe QDs by low temperature STM and STS. The research is an extension of chapter 4 where the effect of quantum mechanical coupling in small aggregates of PbSe QDs was discussed. The LDOS measured at different sites in the QD lattice is markedly

different from that of a single, isolated PbSe QD due to electronic coupling in the array. We report strong microscopic variations in the degree of electronic coupling with two prototypical cases: (i) band-selective coupling, with electron delocalization over neighboring QDs but hole localization, and (ii) full coupling with both electron and hole delocalization and a strongly reduced gap between the highest occupied (HOMO) and lowest unoccupied (LUMO) molecular orbitals. Since the publication of our work, Millo et al. have found similar results for arrays of InAs QDs.[27] In addition to the STS experiments, optical absorption experiments on these 2D arrays of PbSe QDs are presented and discussed.

5.2 Experimental details

The sample preparation procedure for the STS measurements on 2D arrays of PbSe QDs is based on the same method described in section 4.2. The PbSe QDs are self-assembled in a 2D array by drop-casting a dispersion of PbSe QDs from chloroform ($\sim$5-10 μl $CHCl_3$) on a flame-annealed Au(111) substrate. The substrate was held under an angle of 5 -10° to obtain a concentration gradient of PbSe QDs on the substrate. The procedure was performed under water and oxygen free conditions. Immediately after sample preparation, the sample was inserted in the UHV-STM and vacuum annealed to 120-150 °C overnight prior to STM experiments.[7] Vacuum annealing leads to interdigitation of the capping molecules as evidenced by the very good stability of the QD arrays under STM imaging and the small interparticle separation.[4]

For the study presented in this chapter, we investigated PbSe QDs capped with oleic acid (OA, molecular length ca. 2 nm). The average core diameters and size dispersion of the 5.3 nm and ($\pm$10 %), 7.3 nm ($\pm$5 %) PbSe QDs were determined by transmission electron microscopy (TEM).

All STM measurements were carried out at 5 K with an UHV STM (Omicron LT-STM). Typical imaging parameters for topography (STM) are 30 pA set-point current at a bias voltage of 2.5 V and a set-point current of 150 pA at bias voltage 1.2 V for STS. The spectral features were independent of the set-point confirming shell-tunneling conditions.[17,26] As described in section 3.2, the dI/dV conductance spectra were acquired directly with lock-in detection and also obtained by numerical differentiation of the IV-curves. The spectra were checked for reproducibility and the signal to noise ratio was improved by averaging $\sim$ 100 IV and dI/dV spectra.

Samples for the optical experiments were prepared in a similar way as the samples prepared for STM. Details of the chemicals used, are given in appendix B. Multilayers of PbSe QDs were prepared by drop-casting a dispersion of PbSe quantum dots in chloro-

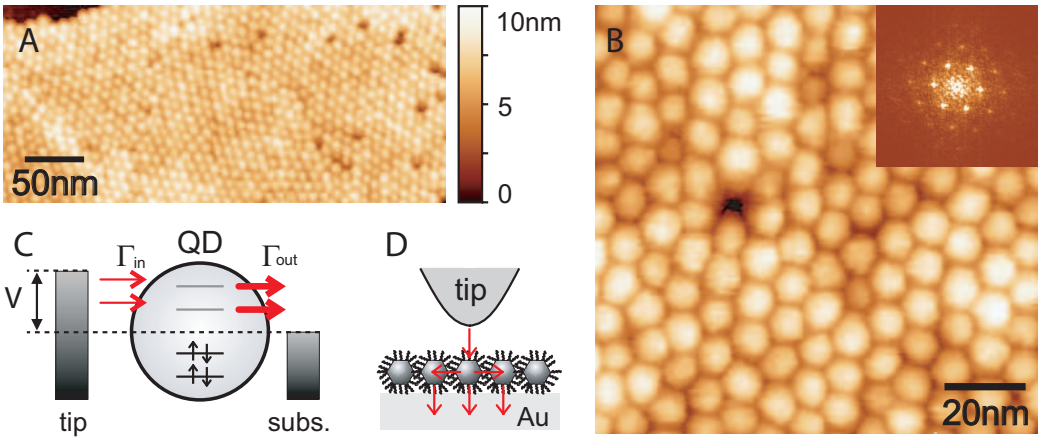

Figure 5.1: (A) Typical large-scale STM topography of 7.3 nm diameter PbSe QDs (sample 1). (B) A zoom-in on a domain with quasi-hexagonal order. Inset: Fourier-transform of the data. (C) Schematic of resonant tunneling spectroscopy in the shell-tunneling regime: the tunneling rate into the QD, Γ_{in}, is much smaller than the tunneling rate out of the QD, Γ_{out}. (D) Relevant tunneling processes in the experiments involving coupled QDs in an array.

form on a quartz substrate. Multilayers of PbSe QDs were needed to improve the signal to noise ratio in the absorption experiments. Prior to optical absorption experiments, the sample was vacuum annealed to 150 °C as was done for all samples used in our STS experiments.

5.3 Results and discussion

5.3.1 Topography of PbSe quantum dots on a gold substrate

Figure 5.1A shows a topographic image of a 2D array of 7.3 nm PbSe QDs on a Au(111) substrate (sample 1). The layer shows local hexagonal packing, but lacks true long-range order due to size and shape dispersion of the nanocrystal building blocks and probably also due to orientational disorder of the individual QDs. Figure 5.1B shows a higher magnification image displaying a typical crystalline defect (vacancy) that we often observe in these arrays. The fast fourier transform (FFT, inset in figure 5.1B) confirms the presence of quasi-hexagonal ordering (broadened points in the FFT) and gives 8.6 nm as the center-to-center spacing corresponding to $\sim$1 nm spacing between the QDs. After the topographic imaging, we can select any QD site in the array for tunneling spectroscopy.

5.3.2 Spectroscopy of PbSe quantum dots on a gold substrate

In shell-tunneling spectroscopy, figure 5.1C, the tunneling rate into the PbSe QD (Γ_{in}) is much smaller than the rate of tunneling out (Γ_{out}) of the PbSe QD.[15,17] The electrons tunnel through the QD one-by-one, charging effects are absent and the measured dI/dV spectrum directly reflects the LDOS at the position of the STM tip. Figure 5.1D shows the relevant tunneling processes in STS experiments on coupled QDs as is also discussed in chapter 4, figure 4.1A. In order to observe quantum mechanical coupling between the QDs in the monolayer, this coupling must be stronger than the tip-dot or dot-substrate tunneling coupling. In the shell-tunneling regime, Γ_{in} is determined by the set-point current I; for typical current values, the resulting coupling energy $\hbar\Gamma_{in}$ is very small, $\sim \mu$eV. The coupling of the QD to the substrate is of the same order of magnitude and thus STS should be able to measure even modest coupling between PbSe QDs.

A topographic image of an array of 5.3 nm diameter PbSe QDs is shown in figure 5.2A (sample 2). The order is less prominent than in figure 5.1, but locally the particles show hexagonal order with an average center-to-center distance of 6.7 nm. The tunneling spectra shown in figure 5.2B were measured on three neighboring QDs (inset). The spectra exhibit a zero-conductance gap and resonances resulting from tunneling through valence (negative bias) and conduction energy levels (positive bias). These spectra can be compared to the spectrum obtained on an isolated PbSe QD depicted in figure 5.2C.[24] While the peak at negative bias corresponding to tunneling through the valence S_h-level is also observed in the array, the resonances at positive bias on QD sites in the array are significantly broader. This is not due to coupling between the QDs and the gold substrate: an additional self-assembled monolayer (SAM) (hexane- or octanethiol) on Au, to increase the distance between the QDs and the substrate, did not affect the observed broadening in the spectra. These results indicate quantum mechanical coupling between the PbSe QDs in the array. Spectra on neighboring QDs in figure 5.2B show very similar features, with only quantitative differences. Such a correlation between the measured spectra can be expected if these QDs each form a lattice site in a quantum mechanically coupled island in the array.

We have performed STS experiments on three different samples, one with monolayers (arrays) of 7.3 nm PbSe QDs (sample 1), one with monolayers of 5.3 nm PbSe QDs (sample 2) and one with monolayers of 5.3 nm PbSe QDs on Au(111) with an additional octanethiol in between (sample 3). On each sample we have measured the LDOS on neighbouring QD lattice cites and we have also inspected different regions in each array. In general we have observed qualitative and quantitative differences in the LDOS with two prototypical cases. Three examples of the more commonly case measured on the three different samples are shown in figure 5.3A (three lower spectra). They show peaks

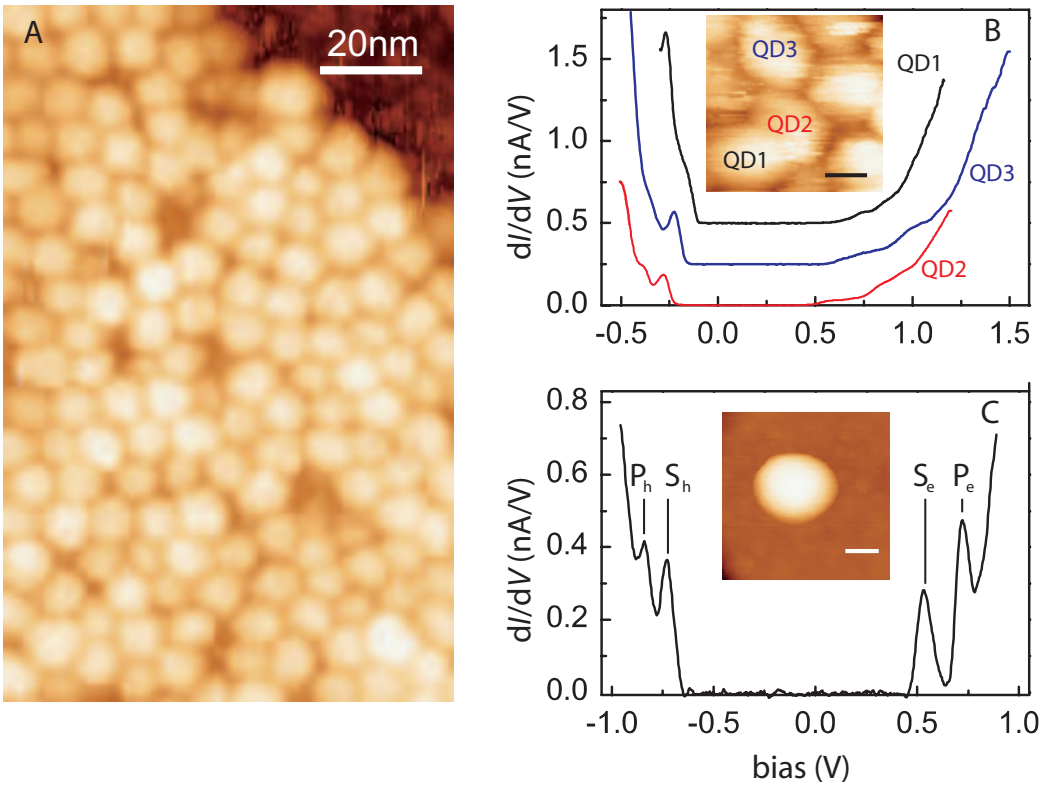

Figure 5.2: Examples of measured dI/dV spectra on neighboring QDs. (A) Large-scale topographic image of 5.3 nm diameter PbSe QDs (sample 2). (B) Experimental dI/dV spectra measured on the three neighboring QDs (inset). (C) Spectrum of an isolated PbSe QD (5.3 nm diameter) linked to Au(111) using hexanedithiol. The quantum-confined energy levels corresponding to the tunneling resonances are indicated. Scale bar 5 nm (insets).

at negative bias corresponding to tunneling through the discrete valence levels, while features at positive bias are significantly broadened. The second case, shown in figure 5.3B, is characterized by steplike features at both positive and negative bias and a significantly reduced width of the zero-conductance gap. Sites in a region with long-range order (sample 1) did not show a significantly different spectroscopic response compared to those in regions with only local order (sample 2). This indicates that the changes in the density of states are mostly due to coupling between nearest neighbors.

Gaussian distributions have been fitted to the band edge features of the spectra in figure 5.3A to get a quantitative measure of the linewidth of the resonances in the spectra. The full width at half maximum (FWHM) for the isolated QD is 65 meV for S_e and

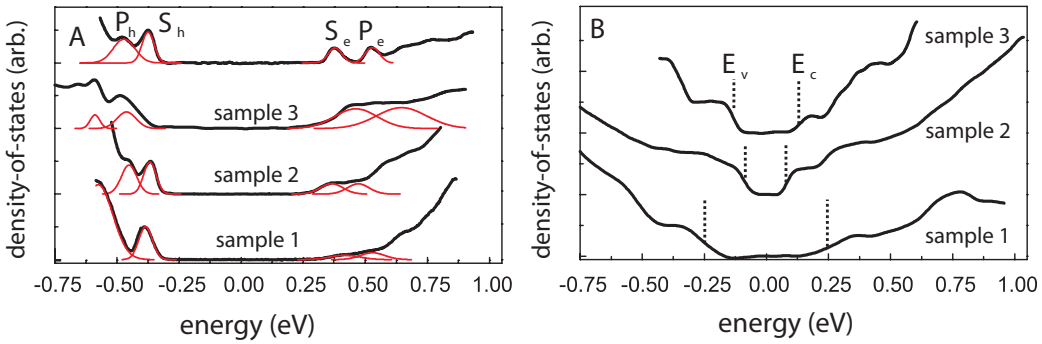

Figure 5.3: Prototypical LDOS measured on PbSe QD sites in an array. (A) Most commonly observed case (three lower spectra). The spectra were measured on three different samples, 7.3 nm diameter QDs (sample 1), 5.3 nm QDs (sample 2), and 5.3 nm QDs with an additional octanethiol SAM in between the PbSe QDs and the gold substrate (sample 3). The top spectrum is that of an isolated 5.3 nm diameter PbSe QD linked to Au(111) using hexanedithiol. The thin lines are Gaussian fits to the first two conduction and valence band features. (B) Examples of spectra in the full coupling regime. Spectra were measured on the same samples as in (A). The conduction and valence band edges are labeled by E_c and E_v, respectively. Bias voltage, V, converted to energy scale using $\eta = (V_{QD} - V_{tip})/V$=0.85 and the DOS taken as the normalized differential conductance $dlnI/dlnV$ and normalized with respect to the height of the first valence level (band).

59 meV for S_h. This linewidth is partly due to the lifting of the degeneracy of $S_{e/h}$-states in PbSe QDs.[23,24] The PbSe QDs in the array have similar widths for the first valence energy level; however, the first conduction energy level has a significantly larger FWHM: 206 (sample 3), 106 (sample 2), and 138 meV (sample 1). We will consider the coupling strength in more detail and compare it with quantum mechanical calculations below. The spectra shown in figure 5.3A implicate that band-selective coupling between the PbSe QDs predominates in arrays: valence energy levels are not - or only weakly - coupled, while the conduction energy levels couple with a strength (defined as the extra broadening of the DOS features) of 50 - 150 meV.

On a considerable minority of the lattice sites in an array (monolayer) the LDOS is qualitatively different, see figure 5.3B. The tunneling spectra show step-like features at positive and negative bias voltage. The steps in the LDOS are a signature of a two-dimensional semiconductor and indicate strong quantum mechanical coupling between both electron and hole energy levels in neighboring PbSe QDs in the array. Because of the delocalization of the electron and hole wave functions in the plane of the array, the confinement energy is strongly reduced, which is seen as a considerable reduction of the single-particle (HOMO-LUMO) gap compared with respect to that of a single, isolated PbSe QD. From these spectra reflecting full-coupling, on average, a bandgap of 300 meV is obtained. The

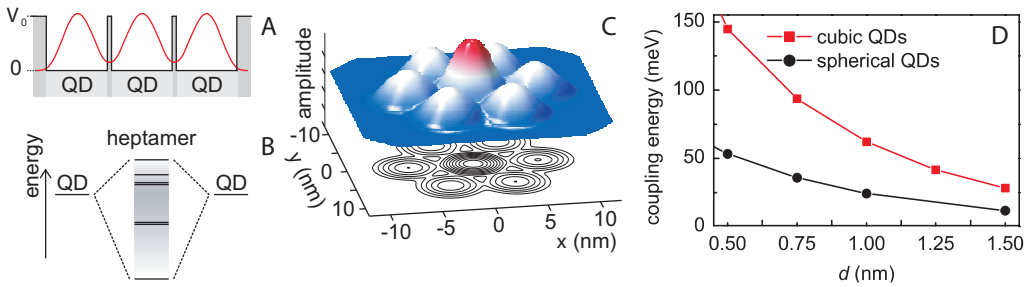

Figure 5.4: Schematic of the level hybridization and results from effective-mass calculations of the ground-state molecular orbital in a QD heptamer. (A) A cross section of the potential energy landscape used in the model along the center of the QD heptamer. (B) Splitting of the QD levels due to quantum mechanical coupling between the QDs: lines indicate the energy level positions in a QD heptamer. In the limit of a large number of coupled QDs, a miniband would be formed. (C) The amplitude of the ground-state wave function in a QD heptamer showing delocalization and formation of a molecular orbital. (D) Calculated coupling energy (defined as the splitting between the most bonding and antibonding orbital) as a function of the nanocrystal edge-to-edge separation for both spherical (black spheres) and cubic QDs (red boxes). The effective mass was 0.05, the barrier height between the QDs 2 eV and the diameter of the spherical QDs was 6 nm; the size of cubic QDs (5 nm) was adjusted to give similar confinement energy.

band gap of isolated PbSe QDs of this size is ∼750 meV (see chapter 3[24]). Since the band gap of bulk PbSe at T=5 K is 145 meV, the confinement energy is reduced from 600 meV in a single PbSe QD to ca. 150 meV in a PbSe QD in a monolayer. Approximately $2/3$ of the confinement energy is lost due to delocalization of the electron and hole wave functions. This is consistent with the formation of a 2D electronic system from zero-dimensional building blocks.

The LDOS measured at the QD sites in an array is essentially different from that of isolated PbSe QDs. We offer further support for these findings with quantum mechanical calculations on the PbSe QDs placed in an array. In figure 5.4 we consider a QD heptamer, with seven spherical (or cubic) PbSe QDs separated by an energy barrier (figure 5.4A). We solve the Schrödinger equation in the effective mass approximation and concentrate on the seven lowest energy eigenstates which arise from the quantum confined energy levels with S-type envelope symmetry. The individual QD wave functions overlap and this results in the formation of molecular orbitals (section 2.4).[28,29] Figure 5.4B shows the resulting energy level structure where the original eigenstates are split due to coupling. Bonding and antibonding molecular (superlattice) orbitals are formed: the ground-state wave-function is shown in figure 5.4C. The orbital is delocalized over all the QDs in the heptamer. Figure 5.4D shows the calculated coupling energy, defined as the splitting between the most bonding and antibonding orbitals. The nanocrystal symmetry is impor-

tant: for spherical QDs, the effect of quantum mechanical coupling is weaker than for cubic QDs. The calculated coupling energy is a factor of 3 higher for cubic nanocrystals. This is due to the enhanced wave-function overlap between the neighboring QDs due to the nanocrystal facets.

From the topography image (section 5.3.1), we measured an average distance of 1 nm between the QDs. For spherical QDs, this means a calculated coupling energy of 25 meV and for cubic QDs a coupling energy of 70 meV. Our experiments were performed on faceted nanocrystals with an overall spherical shape, the coupling strength is most likely to be intermediate between the values calculated for spherical an cubic QDs, on the order of 50 meV. In addition, we have found that rotation of the central nanocrystal in the heptamer of cubic QDs (while keeping the nanocrystal edge-to-edge separation constant) can lead to a reduction of the coupling energy of up to 75%. Finally calculations on larger assemblies (up to 7×7 with a fixed edge-to-edge separation of 1 nm) allow extrapolation of the coupling energy to infinitely large monolayers. This gives 38 meV and 99 meV for hexagonally packed spherical and cubic PbSe QDs respectively and 132 meV for square arrays of cubic QDs.

As the effective masses of the electrons and holes are very similar in PbSe, the observed band-selective orbital coupling is surprising. The most plausible explanation for the band-selective coupling is a variation in the potential landscape experienced by electrons and holes. It has been observed that non-resonant LUMO (HOMO) orbitals levels of the barrier material can have a strong influence on the effective barrier height for electron (hole) tunneling.[30] It is possible that the LUMO orbitals of the capping molecules (OA) enhance electron tunneling between neighboring QDs more than the HOMO orbitals do for holes. We remark that Talapin and Murray performed long-range transport measurements on PbSe QD solids and report a sixfold higher mobility for electrons than for holes, in qualitative agreement with our results.[14] According to the calculations, a difference of 1 - 2 eV in the effective barrier height is sufficient to explain the observed difference in the coupling strength. The simple model used here can explain qualitatively the coupling strength that is measured in most regions in the array. Moreover, local variations (even on an atomic scale) can influence the coupling strength. However, more realistic models such as tight-binding or pseudo-potential calculations will be required for a full understanding of our experiments.

5.3.3 STS versus optical experiments

We used a different measurement technique i.e. optical absorption spectroscopy to study the effects of quantum mechanical coupling in multilayers of PbSe QDs. Figure 5.5A shows an optical absorption spectrum measured on a dispersion of spherical PbSe QDs

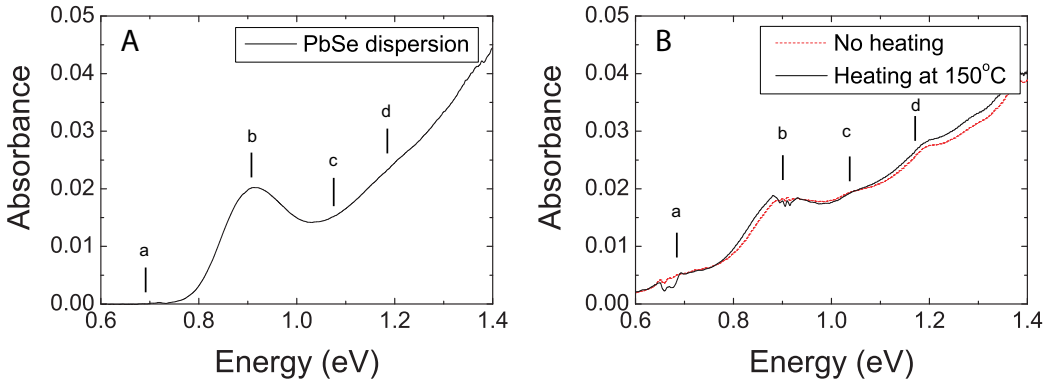

Figure 5.5: Optical absorption spectra of 5.3 nm spherical PbSe QDs (A) in tetrachloroethylene (B) multi-layers on a quartz substrate before and after vacuum annealing at 150^{o}C.

with an average diameter of 5.3 nm deduced from TEM. The absorption spectrum shows a strong excitonic transition at 0.9 eV and less pronounced transitions at higher energy. Figure 5.5B shows two absorption spectra measured on multilayers (superlattices) of PbSe QDs of the same size, one before (dashed line) and one after vacuum annealing at 150 °C over night (solid line). Both spectra show similar features. While the first excitonic transition in both spectra occurs at 0.9 eV, at an energy below 0.8 eV we only observe strong absorbance in the multilayers. Furthermore, the relative absorbance intensity at higher energies in the multilayers (figure 5.5B, d/b) is higher than in the dispersion of PbSe QDs (figure 5.5A, d/b) which indicate a reduction of absorbance of the first excitonic transition.

The reduction of the first excitonic transition and the non-zero absorbance below 0.8 eV can be tentatively assigned to quantum mechanical coupling. Similar position of the peak b in both spectra is an indication that weakly coupled QDs are also present in the multilayer. This is consistent with the variable quantum mechanical coupling observed in STS experiments. Finally, it should be noted that full interpretation of these optical absorbance measurements has to consider effects of scattering in the layer, which could also result in background absorbance below 0.8 eV.

5.4 Conclusions

We have shown that measurements on a local scale are of utmost importance in providing detailed knowledge on the strength and nature of quantum mechanical coupling in inherently disordered monolayers of PbSe QDs. STS measurements on 2D array of PbSe QDs show that the individual QDs are predominantly coupled in a band-selective fashion with a coupling strength of 50-150 meV between the conduction energy levels. In addition,

some regions of array display strong coupling of both the conduction and valence energy levels.

Preliminary optical absorbance measurements on multilayers of PbSe QDs support the picture of variable quantum mechanical coupling in the arrays. However, complete interpretation of the optical experiments requires careful elimination of scattering as a possible source of background absorbance below 0.8 eV.

In conclusion, our STS experiments show that local variations in the electronic structure should not be overlooked in the design of QD materials with tailored properties.

References

[1] Kastner, M.A. "Artificial atoms" Phys. Today 1993, 46, 24-31.
[2] Murray, C.B.; Kagan, C.R.; Bawendi, M.G. "Synthesis and characterization of monodisperse nanocrystals and close-packed nanocrystal assemblies" Annu. Rev. Mater. Sci. 2000, 30, 545-610.
[3] Redl, F.X.; Cho, K.S.; Murray, C.B.; O'Brien, C.B. "Three-dimensional binary superlattices of magnetic nanocrystals and semiconductor quantum dots" Nature 2003, 423, 968-971.
[4] Romero, H.E.; Drndic, M. "Coulomb blockade and hopping conduction in PbSe quantum dots" Phys. Rev. Lett. 2005, 95, 156801/1-4.
[5] Yu, D.; Wang, C.; Guyot-Sionnest, P. "n-Type conducting CdSe nanocrystal solids" Science 2003, 300, 1277-1280.
[6] Shevchenko, E.V.; Talapin, D.V.; Kotov, N.A.; O'Brien, S; Murray, C.B. "Structural diversity in binary nanoparticle superlattices" Nature 2006, 439, 55-59.
[7] Murray, C.B.; Sun, S.; Gaschler, W.; Doyle, H.; Betley, T.A.; Kagan, C.R. "Colloidal synthesis of nanocrystals and nanocrystal superlattices" IBM J. Res. Dev. 2001, 45, 47-56.
[8] Markovich, G.; Collier, C.P.; Henrichs, S.; Remacle, F.; Levine, R.; Heath, J.R. "Architectonic quantum dot solids" Acc. Chem. Res. 1999, 32, 415-423.
[9] Yu, D.; Wang, C.; Wehrenberg, B.L.; Guyot-Sionnest, P. "Variable range hopping conduction in semiconductor nanocrystal solids" Phys. Rev. Lett. 2004, 92, 216802/1-4.
[10] Artemyev, M.V.; Bibik, A.I.; Gurinovich, L.I.; Gaponenko, S.V.; Woggon, U. "Evolution from individual to collective electron states in a dense quantum dot ensemble" Phys. Rev. B 1999, 60, 1504-1506.
[11] Alivisatos, A.P. "Perspectives on the physical chemistry of semiconductor nanocrystals" J. Phys. Chem. 1996, 100, 13226-13239.
[12] Dullens, R.P.A.; Mourad, M.C.D.; Aarts, D.G.A.L.; Hoogenboom, J.P.; Kegel, W.K. "Shape-induced frustration of hexagonal order in polyhedral colloids" Phys. Rev. Lett. 2006, 96, 028304/1-4.
[13] Roest, A.L.; Kelly, J.J.; Vanmaekelbergh, D.; Meulenkamp, E.A. "Staircase in the electron mobility of a ZnO quantum dot assembly due to shell filling" Phys. Rev. Lett. 2002, 89, 036801/1-4.
[14] Talapin, D.V.; Murray, C.B. "PbSe nanocrystal solids for n- and p-channel thin film field-effect transistors" Science 2005, 310, 86-89.
[15] Banin, U.; Millo, O. "Tunneling and optical spectroscopy of semiconductor nanocrystals." Annu. Rev. Phys. Chem. 2003, 54, 465-492.
[16] Banin, U.; Cao, Y.; Katz, D.; Millo, O. "Identification of atomic-like electronic states in indium arsenide nanocrystal quantum dots" Nature 1999, 400, 542-544.

[17] Bakkers, E.P.A.M.; Hens, Z.; Zunger, A.; Franceschetti, A.; Kouwenhoven, L.P.; Gurevich, L.; Vanmaekelbergh, D. "Shell-tunneling spectroscopy of the single-particle energy levels of insulating quantum dots" Nano Lett. 2001, 1, 551-556.

[18] Maltezopoulos, T.; Bolz, A.; Meyer, C.; Heyn, C.; Hansen, W.; Morgenstern, M.; Wiesendanger, R. Wave-function mapping of InAs quantum dots by scanning tunneling spectroscopy"" Phys. Rev. Lett. 2003, 91, 196804/1-4.

[19] Nazin, G.V.; Qiu, X.H.; Ho, W. "Charging and interaction of individual impurities in a monolayer organic crystal" Phys. Rev. Lett. 2005, 95, 166103/1-4.

[20] Wachowiak, A.; Yamachika, R.; Khoo, K.H.; Wang, Y.; Grobis, M.; Lee, D.H. Louie, S.G.; Crommie, M.F. "Visualization of the mlecular Jahn-Teller effect in an insulating K_4C_{60} monolayer" Science 2005, 310, 468-470.

[21] Steiner, D.; Mokari, T.; Banin, U.; Millo, O. "Electronic structure of metal-semiconductor nanojunctions in gold CdSe nanodumbbells" Phys. Rev. Lett. 2005, 95, 056805/1-4.

[22] Kim, S.H.; Medeiros-Ribeiro, G.; Ohlberg, D.A.A.; Stanley Williams, R.; Heath, J.R. "Individual and collective electronic properties of Ag nanocrystals" J. Phys. Chem. B 1999, 103, 10341-10347.

[23] Allan, G.; Delerue, C. "Confinement effects in PbSe quantum wells and nanocrystals" Phys. Rev. B 2004, 70, 245321/1-9.

[24] Liljeroth, P.; Zeijlmans van Emmichoven, P.A.; Hickey, S.G.; Weller, H; Grandidier, B.; Allan, G.; Vanmaekelbergh, D. "Density of states measured by scanning-tunneling spectroscopy sheds new light on the optical transitions in PbSe nanocrystals" Phys. Rev. Lett. 2005, 95, 086801/1-4.

[25] Wise, F.W. "Lead salt quantum dots: the limit of strong quantum confinement" Acc. Chem. Res. 2000, 33, 773-780.

[26] Jdira, L.; Liljeroth, P.; Stoffels, E.; Vanmaekelbergh, D.; Speller, S. "Size-dependent single-particle energy levels and interparticle Coulomb interactions in CdSe quantum dots measured by scanning tunneling spectroscopy" Phys. Rev. B 2006, 73, 115305/1-6.

[27] Steiner, D.; Azulai, D.; Aharoni, A.; Banin, U.; Millo, O. "Level structure of InAs quantum dots in two-dimensional assemblies" Nano Lett. 2006, 6, 2201-2205.

[28] Bayer, M.; Hawrylak, P.; Hinzer, K.; Fafard, S.; Korkusinski, M.; Wasilewski, Z.R.; Stern, O.; Forchel, A. "Coupling and entangling of quantum states in quantum dot molecules " Science 2001, 291, 451-453.

[29] Bester, G; Shumway, J.; Zunger, A. "Theory of excitonic spectra and entanglement engineering in dot molecules" Phys. Rev. Lett. 2004, 93, 047401/1-4.

[30] Wang, W.; Lee, T.; Reed, M.A. "Electron tunnelling in self-assembled monolayers" Rep. Prog. Phys. 2005, 68, 523-544.

Chapter 6

STS of arrays of CdSe quantum dots: Response of wavefunctions to local electric fields

We use scanning tunneling microscopy (STM) to controllably contact individual CdSe quantum dots (QDs) in a multilayer array to study electrical contacts to a model QD solid. The probability of electron injection into the QD array depends strongly on the symmetry of the QD wavefunctions and their response to the local electric field. Quantitative spectroscopy of the QD energy levels is possible if the potential distribution in the STM tip-QD array-substrate system is taken into account.

6.1 Introduction

Colloidal semiconductor nanocrystals are one of the most actively studied components of modern nanoscience. The high degree of control over their size and shape makes it possible to accurately tune their opto-electronic properties through quantum confinement.[1–5] In the strong confinement regime, individual semiconductor QDs have widely spaced, discrete energy levels with atom-like envelope wavefunctions (S, P, D etc). Semiconductor QDs can be used as building blocks for more complex architectures, such as two- and three-dimensional superlattices.[2,6,7] This gives the opportunity to combine the quantum confinement in the individual QDs with the cooperative effects of a solid, with potential applications for novel optical and electronic devices.

With the size of the prospective devices shrinking rapidly, the drive to further miniaturize the active area to only a few QDs requires rethinking of the electrical contacts.[8,9] The characteristics of the electrical contacts to the QD layer, i.e. the tunnelling contact between a macroscopic metal and a quantum system, are likely to be crucial in determining the device performance. The electric field due to the applied bias between the contacts gives rise to the (quantum confined) Stark effect which will naturally affect the energies of the electronic levels.[10–14] In addition, the electric field will affect the spatial shape and extension of the wavefunctions in the nanocrystal host, and thus the tunneling contact. Depending on direction of the electric field, it may also lift the degeneracy of the energy levels. The central questions are: (i) what is the role of the electric field distribution over the active device volume, and (ii) how does the symmetry of the quantum confined energy levels of the individual QDs affect the current transport in the device. It should be clear that these questions are equally relevant to the field of molecular devices.

In this chapter, we use low-temperature scanning tunnelling microscopy (STM) and spectroscopy (STS) on multilayer arrays of colloidal CdSe QDs as a model system to controllably contact individual QDs in the first or second layer with the STM tip. The effects due to the field distribution can be probed locally and with high energy resolution. STS has been extensively used to measure the electronic spectrum of single, isolated semiconductor QDs, QD-metal heterostructures, and molecular QD aggregates.[15–20] In addition, studies of quantum mechanical coupling between QDs in self-assembled monolayers have been reported.[21,22] Prior to the present measurements, it was not clear whether a quantitative measurement of the local density of states (LDOS) is possible on arrays thicker than a monolayer: a QD bilayer already consists of an insulating film of >10 nm in thickness, seriously questioning the assumptions behind the simple field-over-tunnel barrier model that is commonly used in interpreting electron tunneling spectroscopy.[23] We will show here that the QD energy levels can be measured qualitatively on both mono- and bilayers once the effect of the potential distribution over the tunnel barriers and the QD layer has

been taken into account. Furthermore, we establish "selection rules" for STS in a double-barrier tunnelling junction based on the spatial symmetries of the orbitals that are involved in the tunnelling processes. Finally, this understanding will be used to elucidate the effect of the electronic spectrum of an asymmetric electric field occurring at a step-edge of the QD layer.

6.2 Experimental details

CdSe QDs (diameter 6.1 nm with a size distribution $<10\%$) were synthesized according to literature methods.[24,25] Hexagonal close-packed arrays were prepared allowing a drop consisting of CdSe QDs dissolved in chloroform solution to slowly dry on an atomically flat HOPG substrate. A second drop-cast allows the QDs to self-organize into a double-layered QD structure. The interdot distance is determined by the organic ligands (tetraoctylphosphine oxide, TOPO) that terminates the QD surface. The samples were annealed up to $150^{\circ}C$ in ultra-high vacuum (UHV) overnight prior to STM experiments. Vacuum annealing leads to interdigitation of the capping molecules as evidenced by the stability of the QD arrays under STM imaging and small interparticle separation[26] (section 3.2). All STM experiments were carried out at 4.8 K with an UHV STM (LT-STM, Omicron Nanotechnology). STM images were taken in the constant-current mode using W and PtIr tips (typical bias voltage of 2-2.5 V and set-point current of 5-20 pA). The tunnelling spectra were acquired by choosing a QD of interest in the array and stabilizing the STM tip above its center. We performed STS at different locations within the assembly, on QDs in the first and second layer, in the middle of the array and at the step-edges.

6.3 Results and discussion

6.3.1 Topography

A topography image of a double-layered structure of CdSe QDs (6.1 nm diameter) is shown in figure 6.1A. The layers show local hexagonal packing but lacks true long range order due to size and shape dispersion of the nanocrystal building blocks. The height profile (figure 6.1B) taken along the line in the topography image gives an average center-to-center spacing of $\sim$7 nm. The inter-particle separation is $\sim$1 nm. We note that this interdot spacing is consistent with the QD separation measured using a small-angle X-ray scattering on close-packed CdSe QD arrays capped with the same capping molecules.[27] To examine the electronic structure, we can select any QD of interest for tunneling spectroscopy.

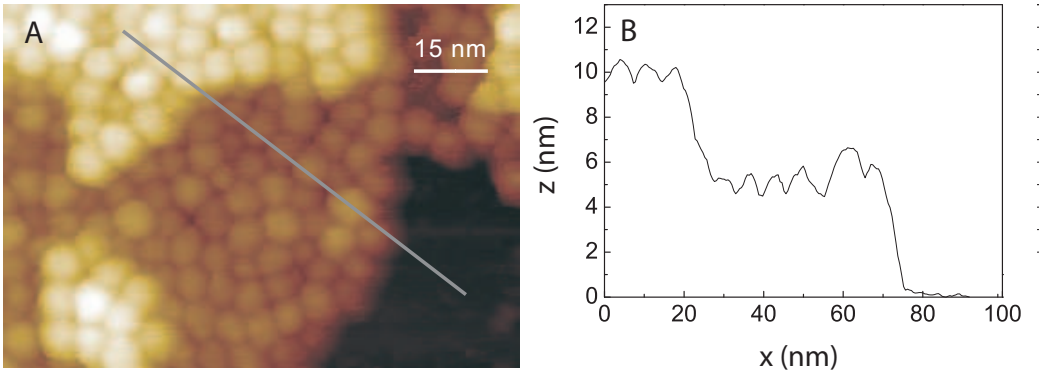

Figure 6.1: (A) Large scale topography image of a hexagonally packed double layered structure of CdSe QDs with an averaged diameter of 6.1 nm on a HOPG substrate. Set-point current 5 pA and bias voltage 2.5 V. (B) Height profile taken along the line denoted in the topography image.

6.3.2 Spectroscopy

Figure 6.2A shows the relevant tunnelling processes in STS experiments involving QDs located in the first and second layer. The current response is mainly determined by the following factors: the tunnelling rate into (Γ_{in}) and out (total rate Γ_{out}) of the QD under investigation, the bias voltage distribution over the tunnelling junctions and the QD layer, and the interdot quantum mechanical coupling (covalent interactions). If Γ_{in} is smaller than Γ_{out} (shell-tunnelling spectroscopy), the electrons tunnel one-by-one through the QD and charging effects are absent.[17,28,29] The bias distribution over the tunnelling junctions and the QD layer influences the measured zero-conductivity gap and the separations between the resonances in the tunnelling spectra.[28,29] This effect has to be taken into account in converting the measured dI/dV spectra from the bias scale to the true energy scale. Strong quantum mechanical coupling between QD wavefunctions in arrays affects the widths of the tunnelling resonances which leads to broadened peaks in the tunnelling spectra.[21,22] On the other hand, if the coupling is weak and the electrons (hole) states are not delocalized over neighbouring QDs, we should observe narrow tunnelling resonances with widths equal to those of individual QDs.

The tunneling spectra measured on CdSe dots in the first layer are shown in figure 6.2B. The dot is indicated in the inset. The spectra exhibit a zero-conductance gap (difference between the highest occupied molecular orbital, HOMO, and the lowest unoccupied molecular orbital, LUMO) with resonances at negative and positive bias voltage corresponding to the valence (hole) and conduction (electron) levels, respectively. Increasing the set-point current from 0.4 nA to 1.6 nA has no effect on the bias position of the resonances, only the intensity of the peaks is increased by decreasing the tip-dot separation

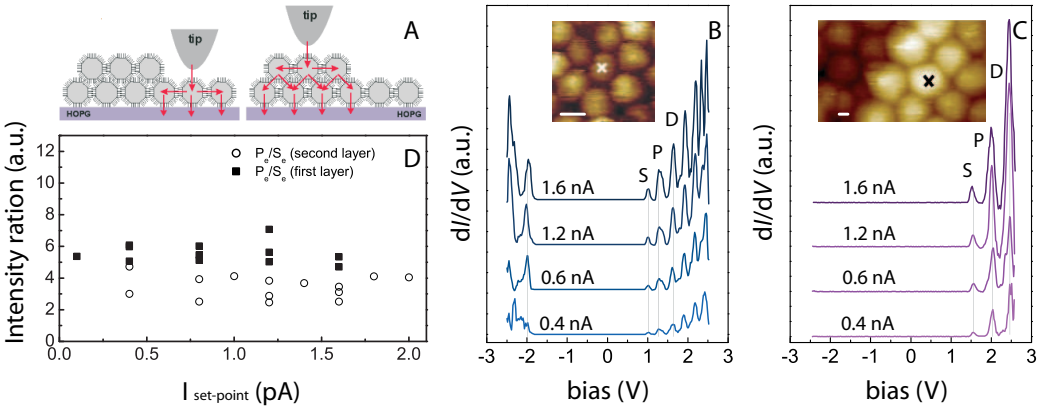

Figure 6.2: STS experiments on CdSe QDs in double layered structure (A) Schematic of the relevant tunneling processes (denoted by arrows) in STS for QDs located in the first (on the left) and the second layer (on the right). (B) and (C) Measured tunneling spectra (dI/dV vs. V) at 5K on a CdSe QD in the first (B) layer and in the second (C) layer. The spectra measured on the QDs are indicated in the inset. layer as denoted in the topography image in the inset. The spectra measured on CdSe dots in the first and second layer are taken at set-point currents 400, 800, 1200 and 1600 pA at bias voltage 2.5V. (D) The P_e-to-S_e peak intensity ratio as function of set-point current for QDs located in the first (○) and second layer (■).

(increasing set-point current), confirming shell-tunneling conditions.[17,28]

Figure 6.2C shows tunneling spectra measured on a dot located in the second layer (the dot is indicated in the inset). Resonances are only observed at positive bias, corresponding to tunneling through conduction levels. In an attempt to access the valence hole levels, we found that at biases exceeding -2.5 V, the tunnelling conditions become unstable. In the following, we only consider electron injection from the STM tip into the QD conduction levels. As for the tunnelling spectra on QDs in the first layer, the spectral features were independent of the tip-QD distance, confirming shell-tunnelling conditions. This implies that we measure single electron energy levels and hence, electron-electron repulsion is absent. The tunnelling spectra measured on CdSe QDs in the first and second layer exhibit the signature of zero-dimensional density of states, with peak widths comparable to isolated CdSe QDs.[26] This indicates weak quantum mechanical coupling between QDs in the monolayer and multilayer arrays. Thus, we ascribe the resonances in the dI/dV spectra to quantum confined energy levels with atom-like envelope wavefunctions: S (LUMO), P, D etc. The absence of quantum mechanical coupling is consistent with the results reported by Kim et. al who found no evidence for interdot wavefunction coupling in CdSe QD assemblies under elevated pressure.[30]

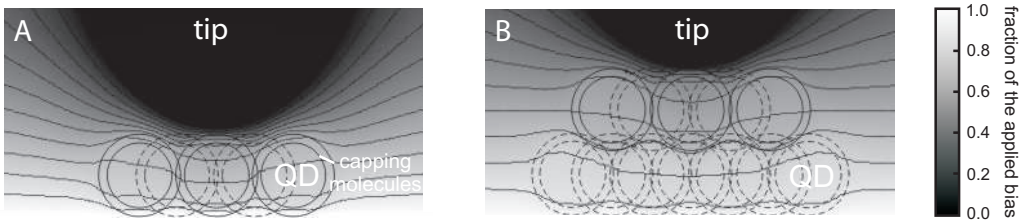

Figure 6.3: Potential distribution in the tip-QD-substrate junction calculated by the solution of Laplace equation in a realistic geometry with 6 nm diameter QD (A) and (B), organic ligands with a length of 0.5 nm and a typical tip-QD vacuum separation of 1.0 nm: a monolayer (A) and bilayer (B) of CdSe QDs. The dielectric constants used in calculations are: 10 for CdSe, 3 for capping molecules.

The spectra recorded on QDs in the second layer show resonances located at higher bias than on QDs in the first layer. To understand this, we have to consider the bias voltage distribution between the STM tip and the substrate. In STS experiments, the applied bias between tip and substrate does not drop completely across the tip-QD junction (section 2.3.2), thus the bias voltage at a resonance in the tunnelling spectrum is related to the QD energy levels (E_i) through: $\eta V_{bias} = E_i + \Sigma_i$, where Σ_i is the polarization energy and η corresponds to the ratio between the potential drop in the tip-QD junction and the applied bias.[29] As a result, the measured zero-conductivity gap is always larger than the quasi-particle gap by a factor $1/\eta$. We estimate η by solving the Laplace equation for a realistic tip-QD-substrate geometry (figure 6.3A and B, with tip radius of 10 nm and tip-to-dot distance of 1 nm) with 6 nm diameter QD and dielectric constants of 10 for CdSe and 3 for organic molecules. The results are shown in figures 6.3C and D. Depending on the exact shape of the tip and the tip-to-dot and dot-to-substrate distance, we found that η is on average 0.70$\pm$0.05 and 0.55$\pm$0.05 for a QD in the middle of the first and second layer, respectively. Multiplying the measured S-to-P peak separation by this factor finally yields an energy difference between the S- and the P-levels of 0.22$\pm$0.02 eV and 0.26$\pm$0.02 eV for QDs in the first and second layer, respectively. Tight-binding calculations predict an S-to-P energy level separation of 0.230 eV for this QD size.[12] These results show that it is still possible to obtain quantitative information on the energy level positions on QD multilayers if an independent estimate of the bias distribution over the entire system is available. This is an important result for future experiments on three-dimensional binary superlattices.

In figure 6.2D, we plot the intensity ratio of the P-to-S resonances for shell-tunneling spectra measured on several QDs in the first and second layer. Interestingly, the ratio measured on CdSe QDs located in the first and second layer differs by almost a factor of

two. In the shell-tunneling regime, the total current is limited by tunneling from the tip into the QD. Hence the tunneling current is $I = e\sum_i \Gamma_{in,i}$, where $\Gamma_{in,i}$ is the tunneling rate from the tip to the level i in the QD. Consequently it might be expected that the P-to-S intensity ratio is proportional to the degeneracy of the energy levels, i.e. an amplitude ratio of 3 for QDs in the first and second layer. However, experimental evidence does not confirm these expectations. We found the P-to-S peak intensity ratio to be on average 3.4±0.7 for spectra measured on QDs in the first layer and 5.7±0.6 for spectra measured on QDs in the second layer. In addition, the P-to-S intensity ratio does not depend on the tip-QD distance in the investigated set-point current range (figure 6.2D). In order to understand the failure of the intuitive reasoning, the symmetry of the P-orbitals and the effect of the electric field have to be taken into account.

In STS experiments, due to the applied bias over the tip-QD-substrate junction, the QD is exposed to a considerable electric field. It is well-know based on theory and experiment that both the energies and electronic densities of the QD eigenstates are affected due to the quantum confined Stark effect (QCSE).[4, 10, 11, 29, 31, 32] Consequently, the electric field can influence the tip-QD wavefunction overlap resulting in different current intensities for orbitals with different symmetries. We estimate these effects by solving the Schrödinger equation for CdSe QDs in an electric field, based on the solution of the Laplace equation in a realistic tip-QD-substrate configuration. The particle-in-a-sphere eigenfunctions in the absence of an electric field are plotted in figure 6.4A, left. The first eigenvalue corresponds to the envelope wavefunction having S-type symmetry (n=1, l=0). The first excited state has P-type symmetry (n=1, l=1) and is three-fold degenerate (P_x, P_y and P_z with m=0, ±1). Resonant tunnelling from the tip into the QD depends on the overlap between the tip and QD wavefunctions;[23] if the tip is positioned directly above the center of the QD, tunnelling through P_x- and P_y-levels has a very low probability (nodal plane). Hence, in the absence of a lateral electric field (vide infra), only the P_z-state contributes to the tunnelling current. Next we will consider in detail how the S and P_z-states respond to the electric field in the STM-substrate junction and how this depends on whether we carry out the measurement on the first or second QD layer.

The response of wavefunctions with S-, $P_{x,y}$- and P_z-envelope symmetry to the electric field under the STM tip is shown in figure 6.4A, right. In the calculation, we neglect quantum mechanical coupling between the QDs, i.e. we only consider the QD directly under the tip in the solution of the Schrödinger equation. As a result of the potential distribution in the STM tip-substrate junction, the wavefunctions respond to the electric field by moving along the field direction. Two consequences emerge from this effect. First, energy is gained by moving the electronic densities in the electric field, i.e. Stark shift. For 6 nm diameter CdSe QDs, the calculated Stark shift is roughly 10 meV for the S-state.

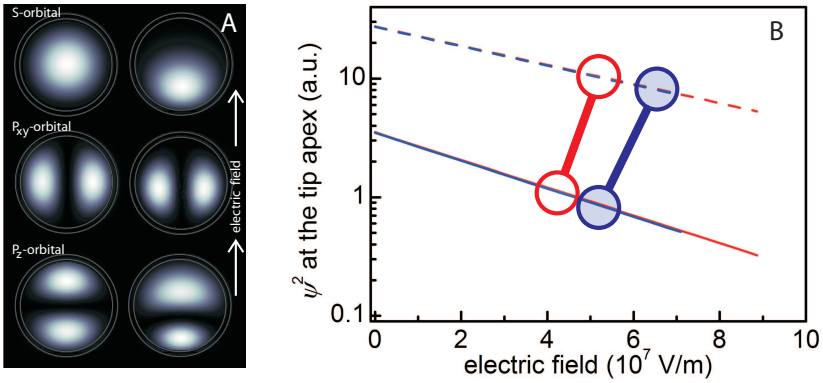

Figure 6.4: Solution of the Schrödinger equation in the field set up in the STM tip-substrate junction. (A) Plots of the squares of the wavefunctions S-, $P_{x,y}$- and P_z-envelope symmetry in the absence (left) and presence (right) of an electric field. (B) Ψ^2 at the tip apex for the S- (solid lines) and P_z-states (dashed lines) on a QD in a monolayer and a bilayer as a function of the average electric field in the QD. The circles indicate the electric fields corresponding to the bias voltage of the S and P resonances in the experiment of the monolayer (white) and bilayer (gray), respectively.

Observing this shift quantitatively in our experiment is not possible due to the QD size and shape distribution. The second consequence of the response of the wavefunctions to the field is that this makes the overlap between the QD and tip wavefunctions smaller and hence affect the resonant tunnelling probability, i.e. the amplitude of the dI/dV signal in the experiment.

In the Tersoff-Hamann formalism,[23] the tunnelling current (and hence the dI/dV signal) is proportional to the square of the wavefunction of a given state at the position of the STM tip and thus depends on how the QD wavefunctions extend outside the nanocrystal (section 2.2). As a result of the electric field, the electron density shifts away from the tip and the ψ^2 at the tip apex is reduced with increasing bias (figure 6.4B). According to our calculations, the ψ^2 at the tip apex for the S- and P_z-states is only a function of the electric field in the QD and does not depend on whether the dot is in the mono- or bilayer. In addition, at a given bias, the average electric field in the QD directly under the STM tip is roughly equal for a QD in the first and second layer. However, due to the voltage distribution in the STM junction, the bias voltage at resonance and hence the electric field is larger on a bilayer compared to a monolayer (open and closed circles in figure 6.4B). Theoretically, we find roughly 20% increase in the P_z-to-S intensity ratio, confirming that the difference in the measured tunneling spectra for CdSe is not an intrinsic effect, but simply the change in the electric field distribution going from the first to the second

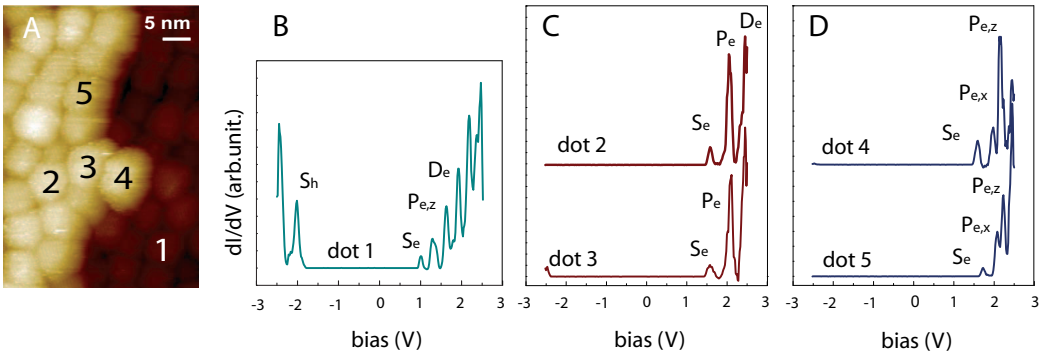

Figure 6.5: Dependence of the STS response on the location of the QDs in the assembly. (A) Topographic image of the 6.1 nm CdSe QDs at a set-point current 5 pA and bias 2.5 V. Examples of dI/dV spectra measured on (B) a QD in the first layer, (C) QDs in the second layer and (D) QDs at the periphery of the second layer. The spectra were obtained at set-point current 1200 pA and bias voltage 2.5V.

layer. The fair correspondence between theory and experiment also supports our idea that only one of the P-orbitals (P_z) is involved in electron tunneling. In order to quantitatively relate the measured intensity of the resonances in the dI/dV spectra to the true LDOS, it is necessary to consider in detail the spatial extension of the wavefunctions involved in the tunneling processes.

Figure 6.5 presents correlated topography-spectroscopy results acquired on QDs at different locations of the double-layer structure. The investigated QDs are labelled in Figure 6.5A. The spectrum measured on QDs in the first layer (QD1) shows resonances at both positive and negative bias (figure 6.5 B) in agreement with previous measurements shown in figure 6.2B. Similarly to the results shown in figure 6.2C, the spectra measured on QDs located well in the array in the second layer (QD2 and QD3) show three peaks at positive bias corresponding to the tunnelling through S-, P_z- and D-states in the shell-tunnelling regime (figure 6.5C). Surprisingly, the spectra measured on QDs at the periphery of the second layer (QD4 and QD5) show an additional peak, as illustrated in figure 6.5D. Which tunnelling processes are responsible for this additional resonance? Varying the set-point current between 0.1 and 0.8 nA shows that these spectra are also measured under shell-tunnelling conditions, i.e. the additional resonance is not related to a lifting of the level degeneracy by Coulomb interactions. A possible hypothesis is that the two closely spaced resonances correspond to tunnelling through the different P-levels; on the other hand, QCSE alone is not sufficient to explain the experimental energy separation (after correcting for the bias distribution) of ca. 100 meV between the two peaks at a bias of ca. 2V in figure 6.5D. There has to be another physical reason for the magnitude of the

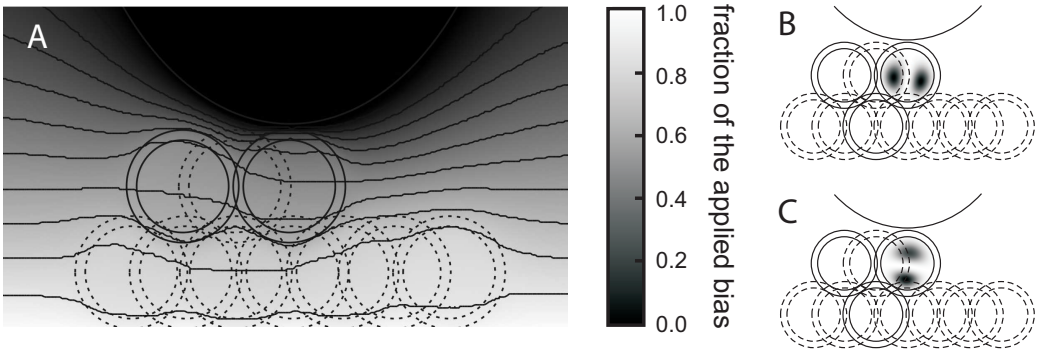

Figure 6.6: (A) Calculation of the electric potential distribution when the STM tip is positioned on a QD at the periphery of the second layer. Response of the wavefunctions to this potential distribution (B) for the P_x- and (C) P_z-orbitals.

observed splitting of the P-levels. It is well-known that the typical synthesis conditions yield CdSe QDs that are slightly prolate due to the wurtzite crystal structure of CdSe. The long axis of the QD corresponds to the c-axis of the crystal (typical aspect ratio of ca. 1.2) and is oriented parallel to the substrate.[2,33] Based on effective mass calculations, the expected energy splitting between the P-levels due to the non-spherical shape of the QD is indeed of the order of 100 meV, in good agreement with the peak separation in the tunnelling spectra in figure 6.5D. It is thus reasonable to assign the two peaks in the spectra in figure 6.5D to the tunnelling through P_x- (parallel to the c-axis, lower bias) and P_z-states (perpendicular to the c-axis, higher bias). The remaining challenge is to explain how tunnelling through the P_x-level (oriented along the c-axis of the QD crystal, i.e. parallel to the substrate) has a much higher probability for a QD at the periphery compared to a QD located in the middle of the array.

In figure 6.6A, we show the potential distribution calculated by solving the Laplace equation in a realistic tip-QD-substrate geometry, for a QD at a periphery of the second layer. Due to the asymmetry of the geometry at the periphery of the layer, there is also a lateral component of the electric field within the QD directly under the STM tip. This asymmetric electric field deforms the QD wavefunctions; we show the calculated results for the P_x- and P_z-orbitals in figures 6.6B and C. In particular, the orientation of the P_x-orbital is lifted from the xy-plane. This reorientation of the wavefunction makes it possible to have tunnelling through this orbital even though the STM tip is located over the center of the QD resulting in an additional peak in tunnelling spectra. While the calculations predict orders of magnitude increase in the tunneling probability through the P_x-level due

to the lateral field, they still cannot fully account for the experimental magnitude of the P_x-resonance. The remaining discrepancy might be due to for example the presence of a permanent crystal dipole. The lateral electric field is absent for QDs located well in the array and consequently, the STM tip above the center of the QD is at the nodal plane of the P_x- and P_y-wavefunctions.

6.4 Conclusions

We have demonstrated how STM and STS can be used to controllably contact and probe QDs in multilayer assemblies. Quantitative spectroscopy of the QD energy levels is possible if the potential distribution in the STM tip-substrate junction is properly taken into account. The probability of electron injection into the QD assembly depends strongly on the symmetry of the QD wavefunctions and their response to the local electric field set-up by the contacts. In particular, the presence of an asymmetric electric field at the step-edge of the QD array can break the symmetry of the wavefunctions and open tunneling channels that otherwise have zero transmission probability. Our results are also important for understanding how the electrical contacts between a macroscopic metal and a QD solid work. We show that an electric field can affect the carrier wavefunctions in QDs in several ways and hence, influence the performance of opto-electronic devices based on QD solids.[9,34,35] Future devices will require control of the tunnel contacts in terms of energy and wavefunction symmetry, and should not overlook irregularities in the QD array.

References

[1] Alivisatos, A.P. "Perspectives on the physical chemistry of semiconductor nanocrystals" J. Phys. Chem. 1996, 100, 13226-13239.

[2] Murray, C.B.; Kagan, C.R.; Bawendi, M.G. "Synthesis and characterization of monodisperse nanocrystals and close-packed nanocrystal assemblies" Annu. Rev. Mater. Sci. 2000, 30, 545-610.

[3] Manna, L.; Scher, E.C.; Alivisatos, A.P. "Synthesis of soluble and processable rod-, arrow-, teardrop-, and tetrapod-shaped CdSe nanocrystals" J. Am. Chem. Soc. 2000, 122, 12700-12706.

[4] Müller, J.; Lupton, J.M.; Lagoudakis, P.G.; Schindler, F.; Koeppe, R.; Rogach, A.L.; Feldmann, J.; Talapin, D.V.; Weller, H. "Wave function engineering in elongated semiconductor nanocrystals with heterogeneous carrier confinement" Nano. Lett. 2005, 5, 2044-2049.

[5] Murray, C.B.; Sun, S.; Gaschler, W.; Doyle, H.; Betley, T.A.; Kagan, C.R. "Colloidal synthesis of nanocrystals and nanocrystal superlattices" IBM J. Res. Dev. 2001, 45, 47-56.

[6] Redl, F.X.; Cho, K.S.; Murray, C.B.; O'Brien, S. "Three-dimensional binary superlattices of magnetic nanocrystals and semiconductor quantum dots" Nature 2003, 423, 968-971.

[7] Chen, Z.; O'Brien, S. "Structure direction of II-VI semiconductor quantum dot binary nanoparticle superlattices by tuning radius ratio" ACS Nano 2008, 2, 1219-1229.

[8] Klein, D.L.; Roth, R.; Lim, A.K.L.; Alivisatos, A.P.; McEuen, P.L. "A single-electron transistor made from a cadmium selenide nanocrystal" Nature 1997, 389, 699-701.

[9] Talapin, D.V.; Murray, C.B. "PbSe nanocrystal solids for n- and p-channel thin film field-effect transistors" Science 2005, 310, 86-89.
[10] Empedocles, S.A.; Bawendi, M.G. "Quantum-Confined Stark Effect in Single CdSe Nanocrystallite Quantum Dots" Science 1997, 278, 2144-2117.
[11] Tews, M.; Pfannkuche, D. "Stark effect in colloidal indium arsenide nanocrystal quantum dots: consequences for wave-function mapping experiments" Phys. Rev. B 2002, 65, 073307/1-4.
[12] Delerue, C.; Lannoo, M. "Nanostructures, theory and modelling" Springer-Verlag, Berlin, 2004.
[13] Wen, G.W.; Lin, J.Y.; Jiang, H.X. "Quantum confined Stark effect in semiconductor quantum dots" Phys. Rev. B 1995, 52, 5913-5922.
[14] Li, S.S.; Xia, J.B. "Quantum-confined Stark effects of InAs/GaAs self-assembled quantum dot" J. Appl. Phys. 2000, 88, 7171-7174.
[15] Banin, U.; Cao, Y.W.; Katz, D.; Millo, O. "Identification of atomic-like electronic states in indium arsenide nanocrystal quantum dots" Nature 1999, 400, 542-544.
[16] Banin, U.; Millo, O. "Tunneling and optical spectroscopy of semiconductor nanocrystals" Annu. Rev. Phys. Chem. 2003, 54, 465-492.
[17] Bakkers, E.P.A.M.; Hens, Z.; Zunger, A.; Franceschetti, A.; Kouwenhoven, L.P.; Gurevich, L.; Vanmaekelbergh, D. "Shell-tunneling spectroscopy of the single-particle energy levels of insulating quantum dots" Nano Lett. 2001, 1, 551-556.
[18] Liljeroth, P.; Zeijlmans van Emmichoven, P.A.; Hickey, S.G.; Weller, H.; Grandidier, B.; Allan, G.; Vanmaekelbergh, D. "Density of states measured by scanning-tunneling spectroscopy sheds new light on the optical transitions in PbSe nanocrystals" Phys. Rev. Lett. 2005, 95, 086801/1-4.
[19] Steiner, D.; Mokari, T.; Banin, U.; Millo, O. "Electronic Structure of Metal-Semiconductor Nanojunctions in Gold CdSe Nanodumbbells" Phys. Rev. Lett. 2005, 95, 056805/1-4.
[20] Overgaag, K.; Liljeroth, P.; Grandidier, B.; Vanmaekelbergh, D. "Scanning tunneling spectroscopy of individual PbSe quantum dots and molecular aggregates stabilized in an inert matrix" ACS Nano 2008, 2, 600-606.
[21] Liljeroth, P.; Overgaag, K.; Urbieta, A.; Grandidier, B.; Hickey, S. G.; Vanmaekelbergh D. "Variable orbital coupling in a two-dimensional quantum-dot solid probed on a local scale" Phys. Rev. Lett. 2006, 97, 096803/1-4.
[22] Steiner, D.; Aharoni, A.; Banin, U.; Oded, M. "Level structure of InAs quantum dots in two-dimensional assemblies" Nano Lett. 2006, 6, 2201-2205.
[23] Tersoff, J.; Hamann, D.R. "Theory of the scanning tunneling microscope" Phys. Rev. B 1985, 31, 805-813.
[24] Murray, C.B.; Norris, D.J.; Bawendi, M.G. "Synthesis and characterization of nearly monodisperse CdE (E=S, Se, Te) semiconductor nanocrystallites" J. Am. Chem. Soc. 1993, 115, 8706-8715.
[25] de Mello Donegá, C.; Hickey, S.G.; Wuister, S.F.; Vanmaekelbergh, D.; Meijerink, A. "Single-Step Synthesis to Control the Photoluminescence Quantum Yield and Size Dispersion of CdSe Nanocrystals" J. Phys. Chem. B 2003, 107, 489-496.
[26] Jdira, L.; Overgaag, K.; Stiufiuc, R.; Grandidier, B.; Delerue, C.; Speller, S.; Vanmaekelbergh, D. "Linewidth of resonances in scanning tunneling spectroscopy" Phys. Rev. B 2008, 77, 205308/1-11.
[27] Kagan, C.R.; Murray, C.B.; Nirmal, M.; Bawendi, M.G. "Electronic Energy Transfer in CdSe Quantum Dot Solids" Phys. Rev. Lett. 1996, 76, 1517-1520.
[28] Jdira, L.; Liljeroth, P.; Stoffels, E.; Vanmaekelbergh, D.; Speller, S. "Size-dependent single-particle energy levels and interparticle coulomb interactions in CdSe quantum dots measured by scanning tunneling spectroscopy" Phys. Rev. B 2006, 73, 115305/1-6.
[29] Niquet, Y. M.; Delerue, C.; Allan, G.; Lannoo, M. "Interpretation and theory of tunneling experiments on single nanostructures" Phys. Rev. B 2002, 65, 165334/1-14.
[30] Kim, B.S.; Islam, M.A.; Brus, L.E.; Herman, I.P. "Interdot interactions and band gap changes in CdSe nanocrystal arrays at elevated pressure" J. Appl. Phys. 2001, 89, 8127-8140.

[31] Mendez, E.E.; Bastard, G.; Chang, L.L.; Esaki, L.; Morkoc, H.; Fischer, R. ”Effect of electric field on the luminescence of GaAs quantum wells” Phys. Rev. B 1982, 26, 7101-7104.

[32] Kraus, R.M.; Lagoudakis, P.G.; Rogach, A.L.; Talapin, D.V.; Weller, H.; Lupton, J.M.; Feldmann, J. ”Room-temperature exciton storage in elongated semiconductor nanocrystals” Phys. Rev. Lett. 2007, 98, 017401/1-4.

[33] Murray, C.B.; Kagan, C.R.; Bawendi, M.G. ”Self-organization of CdSe nanocrystallites into three-dimensional quantum dot superlattices” Science 1995, 270, 1335-1338.

[34] Coe, S.; Woo, W-K.; Bawendi, M.G.; Bulovic, V. ”Electroluminescence from single monolayers of nanocrystals in molecular organic devices” Nature 2002, 420, 800-803.

[35] Konstantatos, G.; Howard, I.; Fischer, A.; Hoogland, S.; Clifford, J.; Klem, E.; Levina, L.; Sargent, E.H. ”Ultrasensitive solution-cast quantum dot photodetectors” Nature 2006, 442, 180-183.

Chapter 7

Binary superlattices of PbSe and CdSe nanocrystals

In this chapter we show that self-organization of colloidal PbSe and CdSe semiconductor nanocrystals with a size ratio of 0.57 leads to formation of binary structures with a AB_2 or a AB_{13} lattice over large areas. We show that the concentration ratio of CdSe vs PbSe nanocrystals is an important factor for the stoichiometry in the case that two different binary superlattices are thermodynamically stable. The stability of these well ordered binary superlattices should make it possible to further study the electronic properties and the interparticle coupling with scanning tunneling microscopy and spectroscopy and provide possibilities to design meta-materials with new collective properties.

7.1 Introduction

Studies of the self-organization of micrometer-sized colloids have been extended in the last decade to crystalline building blocks with dimensions in the nanometer range. Superlattices containing one type of colloidal nanocrystals (NCs) (metallic, magnetic or semiconductor) have been studied in great detail. These studies have been made possible by the availability of NCs with a small distribution in size and shape and with an excellent control of the surface chemistry. More recently, binary NC superlattices based on metallic,[1] or a combination of metallic and semiconductor building blocks,[2,3] have also been reported. A wide variety in structures, and stoichiometry, and an astounding long-range order have been demonstrated.[4] Despite the obvious importance for the study of colloidal self-organization and possible applications in novel opto-electronic materials, the formation of binary superlattices consisting of two semiconductor NCs has been quite limited. Binary superlattices combining PbTe and Ag_2Te,[5] and CdSe and CdTe NCs[6,7] have been presented recently.

In this chapter, we report on the formation of binary superlattices consisting of PbSe and CdSe NCs of the AB_2 and cuboctahedral AB_{13} (cub-AB_{13}) type (A = PbSe NC, B = CdSe NC). CdSe and PbSe nanocrystalline quantum dots are the work horses of colloidal nanoscience. The synthesis, electronic structure, quantum confinement, and the optical and electrical properties of both types of NCs have been dealt with in numerous studies. Our choice for this particular combination was further motivated by the strong difference in the optical bandgap (PbSe at around 1 eV, CdSe at around 2 eV), which should facilitate the study of collective opto-electronic properties. For instance, such a binary superlattice may show a weakly coupled type II band structure,[8,9] featuring long-lived excitons delocalized over PbSe NC/CdSe NC molecular units, thus opening a venue to novel electrical and optical properties beyond those of the individual NCs. In addition, PbSe and CdSe NCs have different crystalline structures; this prevents atomic diffusion and alloying by thermal treatments.[10]

7.2 Experimental details

CdSe and PbSe nanocrystals were synthesized by methods described previously in the literature.[11,12] The CdSe NCs have a trioctylphosphine oxide and hexadecylamine (TOPO and HDA) capping and an effective diameter of 5.8 ± 0.3 nm (core-diameter: 3.4 ± 0.3 nm). The PbSe NCs have an oleic acid capping (OA) and an effective diameter of 10.3 ± 0.5 nm (core-diameter: 7.3 ± 0.6 nm). The core and effective diameters were obtained from TEM images of single-component monolayers. The center-to-center distance was taken as the effective diameter.

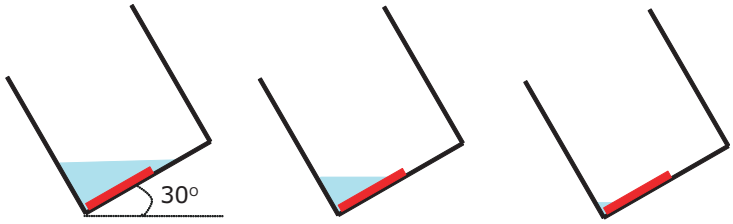

Figure 7.1: Schematic representation of the binary nanocrystal formation. Left: a TEM grid (copper) is placed in a mixed CdSe NC / PbSe NC suspension in a vial with the substrate forming an angle of 30° with the surface of the drying dispersion. Center: evaporation of the solvent from the suspension under reduced pressure at 70°C. Right: the solvent has evaporated, the binary structures are formed on the TEM grid.

Mixed CdSe NC / PbSe NC suspensions were prepared using toluene, chloroform and tetrachloroethylene (TCE) as solvents. The NC concentration ratio c_{CdSe}/c_{PbSe} was varied between 1 and 30. Before the formation of superlattices, the NCs were extracted from the synthesis solution, washed two times and redispersed in the solvent. Colloidal crystallization was achieved by evaporation of the solvent from the suspension under reduced pressure at 70 °C, the substrate forming an angle of 30° with the surface of the drying dispersion[3] (figure 7.1). After evaporation, the TEM grids were dipped in ethanol to remove the excess of NCs not incorporated into the superlattices. The structures formed on the TEM grids were analyzed with a Tecnai 12 and a Tecnai 20 TEM.

In order to reproducibly form binary structures, the concentration ratio of PbSe and CdSe nanocrystals is of utmost importance. The concentration of PbSe nanocrystals in suspension with TCE as solvent was determined using the method of Moreels at al.[13] In this method, the concentration of nanocrystals in a suspension was measured by inductively coupled plasma mass spectrometry (ICP-MS) combined with a TEM analysis of the size and shape of the nanocrystals. In a second step, the absorbance of the suspension was measured and related to the nanocrystal concentration. More specifically, they used the integrated absorbance $\int AdE = -\int log(I/I_0)dE$ of the first exciton transition to determine the integrated molar extinction coefficient as a function of the nanocrystal diameter d, yielding:

$$\varepsilon_{gap,eV} = 3.1d^{0.9}(cm^{-1}\mu M^{-1}meV) \tag{7.1}$$

By using the absorbance integrated over the inhomogeneously broadened first exciton transition, effects of a variation in size-dispersion can be eliminated. We have determined the core diameter of the PbSe nanocrystals used in the crystallization experiments from

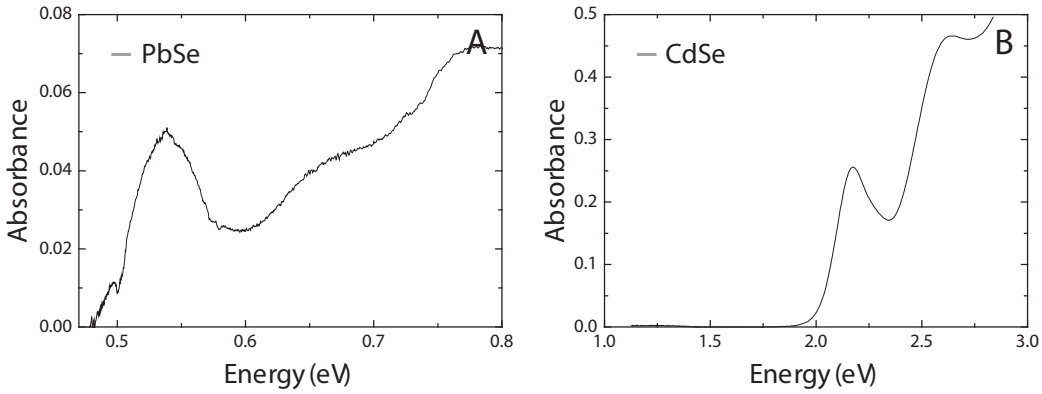

Figure 7.2: Absorption spectrum of (A) a dispersion of quasi spherical PbSe NCs in TCE with an average core diameter of 7.3 nm obtained from TEM, (B) a dispersion of quasi spherical CdSe NCs in TCE with an average core diameter of 3.4 nm.

TEM analysis (7.3 nm), and used this value to calculate $\varepsilon_{gap,eV}$ from equation 7.1. From the absorbance (absorption spectrum presented in figure 7.2A) measured trough a suspension (thickness l) of the PbSe nanocrystals in TCE we obtained the integrated absorbance and used this to determine the PbSe nanocrystal concentration c via the Lambert-Beer law: $\int AdE = -\int log(I/I_0)dE = \varepsilon_{gap,eV}cl$.

The concentration of CdSe nanocrystals in a TCE suspension was determined following the method of Yu et al.[14] Yu et al. determined the molar extinction coefficient for CdSe suspension of known concentrations at the maximum of the first exciton absorption peak, yielding:

$$\varepsilon = 5857d^{2.65}(cm^{-1}M^{-1}) \tag{7.2}$$

In order to determine the concentration c of the CdSe nanocrystals in diluted TCE suspensions, we have measured the absorbance at the first exciton transition (absorption spectrum presented in figure 7.2B). The concentration of the diluted stock-suspension is then calculated from the Lambert-Beer law $A = -log(I/I_0) = \varepsilon cl$ and equation 7.2, applied to nanocrystals with a core diameter d of 3.4 nm as obtained from TEM.

7.3 Results and discussion

The structure and stoichiometry of the deposited NC layers depended strongly on the solvent of the dispersion. Solvent evaporation from toluene and chloroform suspensions

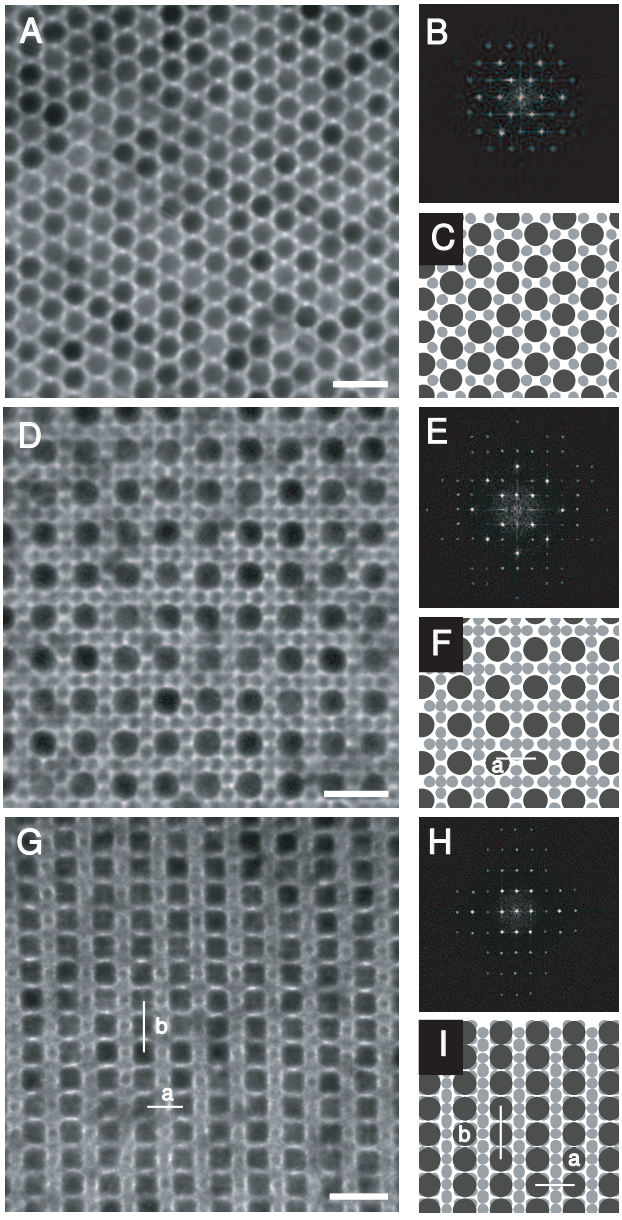

Figure 7.3: TEM images of binary structures formed with CdSe and PbSe nanocrystals. (A): an AB_2 structure representing the (0001) plane (compare with the same projection of a model structure in (C)), (B) is the FFT; (D): AB_{13} representing the (100) plane (cub-AB_{13} model presented in (F)), the FFT is presented in (E); (G): AB_{13} with (110) PbSe termination, (cub-AB_{13} model presented in (I)), the FFT is presented in (H). All scale bars represent 20 nm.

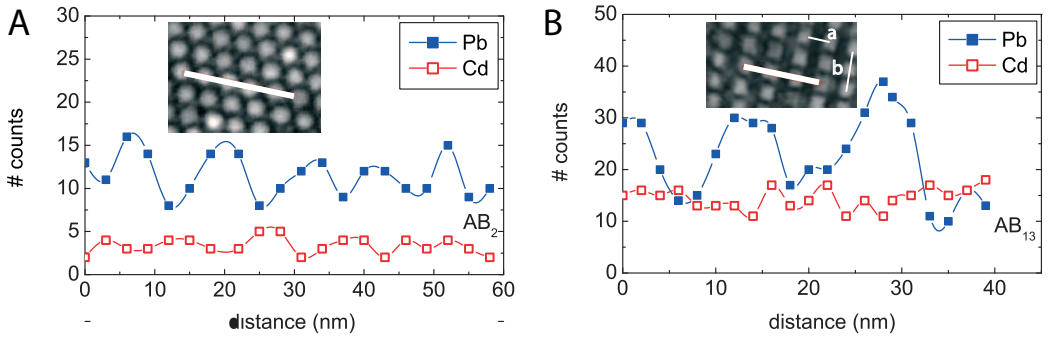

Figure 7.4: Scanning TEM (STEM) with EDX Cd and Pb element analysis to locate the CdSe and PbSe nanocrystals in binary superlattices. (A) AB_2; line scan in the (0001) plane showing an alternation of maxima in the Pb (■) and Cd (□) amounts, indicating alternating PbSe and CdSe nanocrystals with a period of 11.2 nm. (B) AB_{13} (with (110) plane parallel to the substrate), scanned along a, showing the positions of the PbSe nanocrystals, the positions of the CdSe nanocrystals are not fully resolved.

resulted in a deposit that consisted of single-component hexagonally ordered PbSe, CdSe NC superlattices and disordered structures, with only a small percentage ($< 1\%$) of binary superlattices. In contrast, dispersions of mixed PbSe and CdSe NCs in TCE resulted in deposits with a considerable fraction of binary PbSe-CdSe NC superlattices exhibiting long-range order over micrometers. Here we only consider the results obtained with TCE.

Figure 7.3 presents the observed binary superlattices, AB_2 and AB_{13}, in more detail. The preferential orientation of the AB_2 structure (figure 7.3A-C) is with the (0001) plane parallel to the substrate. This was confirmed by the same projection of a model AB_2 structure (figure 7.3C). AB_2 consists of a simple hexagonal arrangement of large A (PbSe) particles, with the smaller B (CdSe) particles filling all the interstices between the A layers (honeycomb pattern). The nature of the nanocrystals in the binary structures was confirmed by elemental analysis along the line (figure 7.4A) using STEM-EDX. This shows a clear modulation in the amount of Pb (the maxima indicating the PbSe NCs) in anti-phase with the amount of Cd (indicating the CdSe NCs), in agreement with an AB_2 lattice. The PbSe center-to-center distance in the (0001) plane is 11.2 nm. The Fast-Fourier Transformation (FFT) of the TEM image (figure 7.3B and figure 7.5) is indicative of long-range hexagonal order. The PbSe NC center-to-center distance is 10.4 nm, which is in reasonable agreement with the STEM center-to-center distance. Note that the STEM-EDX measurement is prone to thermal drifts.

For the AB_{13} structures (figures 7.3D-F and G-I), the preferential crystal orientation is with the (100) plane parallel to the substrate (figure 7.3D) with a minor fraction of the

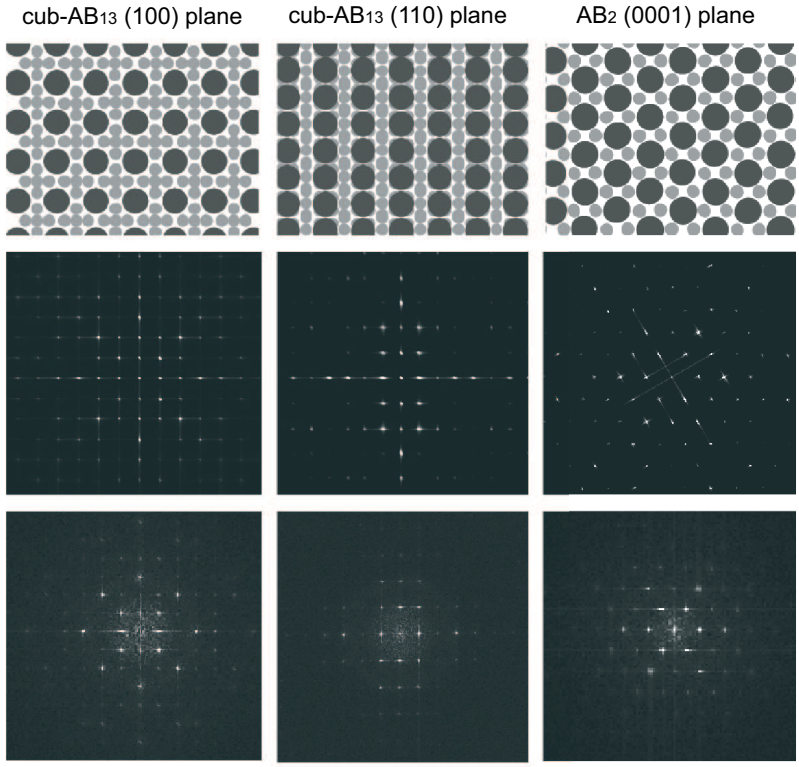

Figure 7.5: Comparison between the FFT of the obtained AB_2 and AB_{13} superlattices and model structures. Top: model planes; Center: their FFT; Bottom: the experimentally obtained FFT.

lattices showing the (110) plane (figure 7.3I). Comparison with the same projections of cuboctahedral AB_{13} model structures presented in figure 7.3F and I shows that the TEM images are in close agreement with the model structure. The cub-AB_{13} structure consists of a simple cubic lattice of large spheres A (PbSe) with a cuboctahedral cluster of 13 B particles (CdSe) in the body-center of each unit cell. The high degree of order in the AB_{13} structures is obvious from the FFT (figures 7.3E and H). The FFT of the cub-AB_{13} model structure show strong resemblance to the experimental data (figure 7.5). Figure 7.3D shows the (100) plane with a measured PbSe NC center-to-center distance of 12.9 nm. Figure 7.3G shows the (110) plane with a termination of PbSe NCs from the next parallel plane. The PbSe-PbSe distance b = 17.4 nm and a = 12.5 nm. The distance $a \simeq 17.4/\sqrt{2}$ confirms the projection of the (110) plane. STEM-EDX used for elemental analysis along the line (a) indicated in figure 7.4B shows clear modulations in the Pb amount, indicating the PbSe NC positions. The resolution was not good enough to resolve the positions of the CdSe NCs.

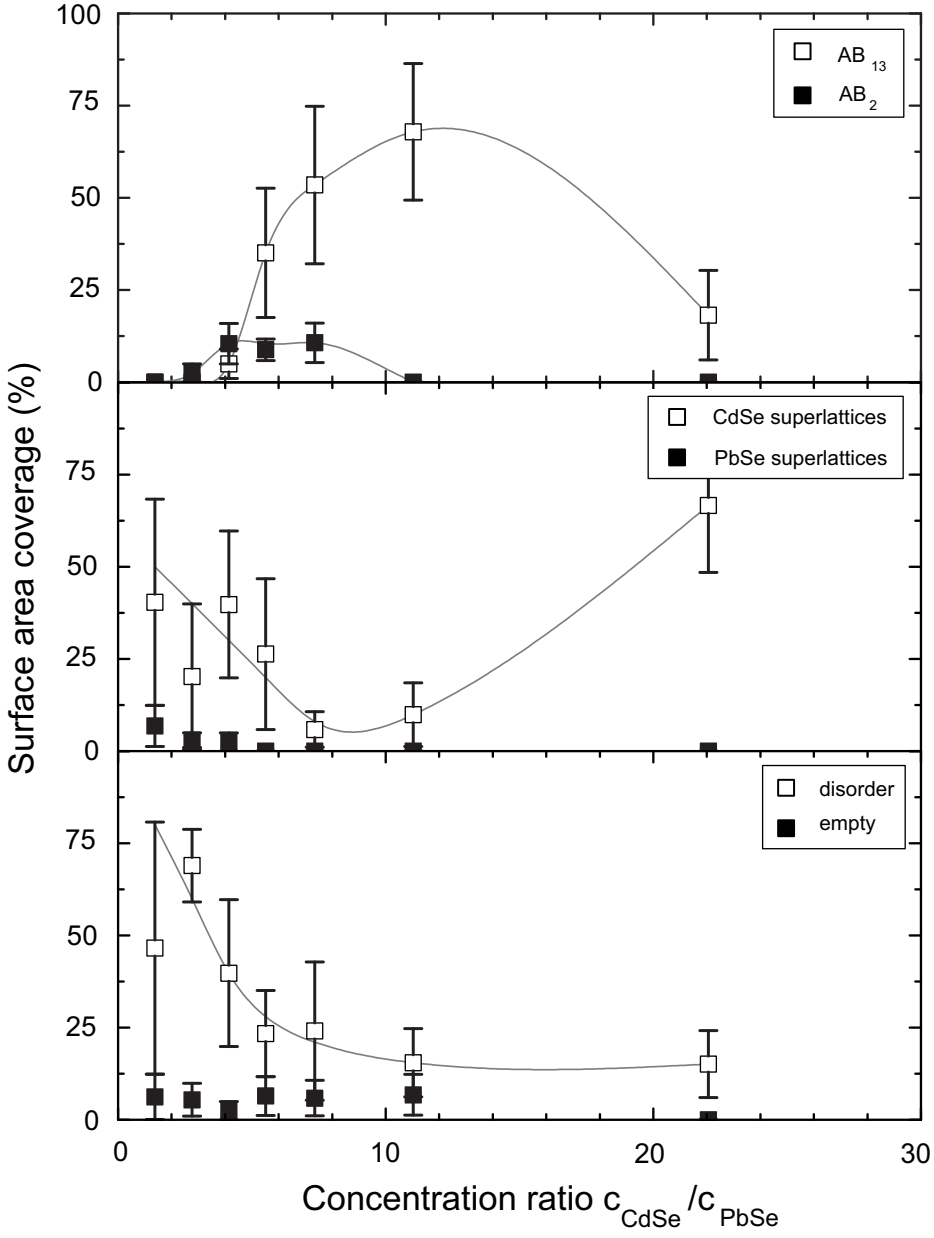

Figure 7.6: The surface area coverage on the TEM grids with (top panel) AB_2, AB_{13} (A=PbSe, B=CdSe) and (middle panel) single-component CdSe and PbSe superlattices as a function of the concentration ratio of CdSe vs. PbSe nanocrystals in the suspensions. The lowest panel shows the relative coverage with disordered layers and the uncovered area. For each concentration ratio, a total area of 4000 μm^2 was analyzed. The gray lines represent a guide to the eye.

From 2-D TEM analysis, it may be concluded that the presented structures are cub-AB_{13},[15] not icosahedral AB_{13}. However, we have to remark that preliminary 3-D TEM (tomography) performed on a few positions in the binary arrays provide evidence for ico-AB_{13}. It is at present not clear whether the AB_{13} structures that we study have the cub- or ico-structure, or both.

We studied the effect of the particle concentration ratio c_{CdSe}/c_{PbSe} varied between 1 and 30 on the composition (binary, mono-component structures and disorder) and the structure of the deposit (figure 7.6). At relatively low concentration ratios, i.e. $1 < c_{CdSe}/c_{PbSe} < 3$, the deposit consisted mainly of disordered layers ($\sim 65\%$ of the total surface area), single-component CdSe superlattices ($\sim 30\%$) and a minor fraction of the PbSe superlattices ($\sim 1\%$). If c_{CdSe}/c_{PbSe} is increased between 2 and 9, AB_2 superlattices occur on the TEM grids and the surface coverage of AB_2 reaches a maximum of 10% at c_{CdSe}/c_{PbSe} = 5 and decreases at larger ratios. The surface coverage of AB_{13} superlattices shows a pronounced maximum between $7 < c_{CdSe}/c_{PbSe} < 20$ with a maximum surface coverage of 60% at c_{CdSe}/c_{PbSe} around 12. If the c_{CdSe}/c_{PbSe} ratio is increased above 20, ordered single-component CdSe structures take over at the expense of the AB_{13} superlattices. Figure 7.6 illustrates that the amounts of binary PbSe $(CdSe)_{13}$ and single-component CdSe NC superlattices are correlated; when the surface coverage of AB_{13} shows a pronounced maximum, the single-component superlattice shows a pronounced minimum. To a certain extent the structure and stoichiometry of the superlattices can be regulated by the relative concentrations of the constituting NCs in the suspension.

The self-organization of micrometer sized colloids into binary superlattices has been successfully explained on the basis of the hard sphere model.[16,17] In this model, only a steep repulsion at short inter-particle distance is assumed, which means that the driving force for crystallization is purely entropic. Interactions between the particles e.g. van der Waals are not taken into account. In the limit of high osmotic pressures, the entropic change is positive and maximum if the crystal has the highest packing density.[17]

It is interesting to consider to what extent the structures that we observe can be explained with the hard-sphere model. The line of reasoning is similar to that of ref. 6 held for superlattices of CdSe and CdTe NCs. The effective diameters of the CdSe and PbSe NCs are 5.8 and 10.3 nm, respectively. For this size ratio (d_{CdSe}/d_{PbSe}) of 0.57 the single-component and the AB_2 structure show a filling factor of $\sim$0.77, while the filling factor of the cub-AB_{13} is $\sim$0.68 and of ico-AB_{13} is $\sim$0.72. On the basis of the hard-sphere model, we must conclude that for a size ratio d_{CdSe}/d_{PbSe} = 0.57, single component and binary AB_2 structure as the most probable structures. This is in agreement with

our large-scale TEM analysis for $1 < c_{CdSe}/c_{PbSe} < 7$ showing mostly single-component superlattices of CdSe and a maximum of 10% AB_2 structure. However, for $7 < c_{CdSe}/c_{PbSe} < 20$, the AB_{13} superlattice dominates with a filling factor of $\sim$0.7. This cannot be explained by the hard-sphere model. Therefore inter-particle interactions, e.g. van der Waals or dipole-dipole interactions must also be important. Van der Waals interactions between the capping molecules increase with the number of nearest neighbors of each PbSe and CdSe nanocrystal. In binary structures, the number of nearest neighbors around the A-site (PbSe) is between 20 (AB_2) and 24 (AB_{13}), hence much larger than for a single-component fcc structure (12), while for the B-site the number is similar to that in a single-component fcc structure (9 for AB_2 or 12 AB_{13}). Therefore, the strong presence of cub-AB_{13} superlattices suggests that van der Waals interactions between adjacent NCs are important for the lattice free energy. The interactions between the capping molecules of adjacent crystals, here OA around PbSe, and TOPO and HDA around CdSe, provide an important contribution to the inter-particle van der Waals pair energy. Calculations show that van der Waals forces between two parallel alkane molecules of 10 units can amount to a pair interaction of about 10 kT at room temperature.[6] It is not yet clear if other origins of inter-particle interactions should also be taken into account. In this respect, we note that recent cryo-TEM experiments displayed strings of PbSe and CdSe particles in suspension pointing to an electric crystal dipole moment.[18,19] We remark that it is not yet understood why AB_5 ($CuAu_5$) structures are not observed in our experiments with PbSe and CdSe NCs while a combination of CdTe and CdSe NCs, binary AB_5 structures have been reported.[6] The $CuAu_5$ structure has almost the same filling factor as the AB_{13} at the present size ratio of 0.57 (section 1.3) and also a similar number of nearest neighbors. In addition, it is also not clear why in our experiments with PbSe and CdSe NCs, the use of solvent TCE leads to reproducible micro-meter sized binary superlattices, while toluene with a two times lower density and similar dielectric constant, and chloroform with a similar density and two times larger dielectric constant, leads to phase segregation. Further research is needed for a deeper understanding of nanocrystal self-organization in binary structures.

7.4 Conclusions

The formation of binary superlattices via colloidal crystallization is the most promising method to realize nanostructured architectures in which different materials are positioned in a well-defined 3-D geometry and where the NCs are in near contact.

In our research, two types of semiconductor NCs with a strongly different optical gap (PbSe NC around 1 eV, CdSe NC around 2 eV) can be assembled in AB_2 and AB_{13} geometries over large areas.

For the size ratio of R_B/R_A=0.57, we showed a relation between the appearance of binary structures and the concentration ratio of CdSe and PbSe NCs. AB_2 structures were mainly formed in concentration ratio's between 3 and 9 and cub-AB_{13} mainly between 7 and 20. The hard sphere model predicts the formation of AB_2 structures but cannot fully explain our observation of cub-AB_{13} structures indicating that inter-particle forces might play a role. The structures that we obtain are mostly three-dimensional and sufficiently thick for optical applications.

References

[1] Kiely, C. J.; Fink, J.; Brust, M.; Bethell, D.; Schiffrin, D. J. "Spontaneous ordering of bimodal ensembles of nanoscopic gold clusters" Nature 1998, 396, 444-446.

[2] Rogach, A. L. "Binary superlattices of nanoparticles: self-assembly leads to metamaterials" Angew. Chem.-Int Ed 2004, 43, 148-149.

[3] Redl, F. X.; Cho, K. S.; Murray, C. B.; O'Brien, S. "Three-dimensional binary superlattices of magnetic nanocrystals and semiconductor quantum dots" Nature 2003, 423, 968-971.

[4] Shevchenko, E. V.; Talapin, D. V.; Kotov, N. A.; O'Brien, S.; Murray, C. B. "Structural diversity in binary nanoparticle superlattices" Nature 2006, 439, 55-59.

[5] Urban, J. J.; Talapin, D. V.; Shevchenko, E. V.; Kagan, C. R.; Murray, C B. "Synergism in binary nanocrystal superlattices leads to enhanced p-type conductivity in self-assembled PbTe/Ag_2Te thin films" Nature Mat. 2007, 6, 115-121.

[6] Chen, Z. Y.; Moore, J.; Radtke, G.; Sirringhaus, H.; O'Brien, S. "Binary nanoparticle superlattices in the semiconductor-semiconductor system: CdTe and CdSe" J. Am. Chem. Soc. 2007, 129, 15702-15709.

[7] Chen, Z.; O'Brien, S. "Structure direction of II - VI semiconductor quantum dot binary nanoparticle superlattices by tuning radius ratio" ACS Nano 2008, 2, 1219-1229.

[8] Kim, S.; Fisher, B.; Eisler, H. J.; Bawendi, M. "Type-II quantum dots: CdTe/CdSe(core/shell) and CdSe/ZnTe(core/shell) heterostructures " J. Am. Chem. Soc. 2003, 125, 11466-11467.

[9] Chin, P. T. K.; de Mello Donegà, C; van Bave, S. S.; Meskers, S. C. J.; Sommerdijk, N. A. J. M.; Janssen, R. A. J. "Highly luminescent CdTe/CdSe colloidal heteronanocrystals with temperature-dependent emission color" J. Am. Chem. Soc. 2007, 129, 14880-14886.

[10] Kudera, S.; Carbone, L.; Casula, M. F.; Cingolani, R.; Falqui, A.; Snoeck, E.; Parak, W. J.; Manna, L. "Selective growth of PbSe on one or both tips of colloidal semiconductor nanorods" Nano Lett. 2005, 5, 445-449.

[11] de Mello Donegà, C.; Hickey, S. G.; Wuister, S. F.; Vanmaekelbergh, D.; Meijerink, A. "Single-step synthesis to control the photoluminescence quantum yield and size dispersion of CdSe nanocrystals" J. Phys. Chem. B 2003, 107, 489-496.

[12] Houtepen, A. J.; Koole, R.; Vanmaekelbergh, D.; Meeldijk, J.; Hickey, S. G. "The hidden role of acetate in the PbSe nanocrystal synthesis" J. Am. Chem. Soc. 2006, 128, 6792-6793.

[13] Moreels, I.; Lambert, K.; de Muynck, D.; Vanhaecke, F.; Poelman, D.; Martins, J.C.; Allan, G.; Hens, Z. "Composition and size-dependent extinction coefficient of colloidal PbSe quantum dots" Chem. Mater. 2007, 19, 6101-6106.

[14] Yu, W.W.; Qu, L.; Guo, W.; Peng, X. "Experimental determination of the extinction coefficient of CdTe, CdSe, and CdS nanocrystals" Chem. Mater. 2003, 15, 2854-2860.

[15] Shevchenko, E. V.; Talapin, D. V.; O'Brien, S.; Murray, C. B. "Polymorphism in AB_{13} nanoparticle superlattices; an example of semiconductor-metal metamaterials" J. Am. Chem. Soc. 2005, 127, 8741-8747.

[16] Murray, M. J.; Sanders, J. V. "Close-packed structures of spheres of two different sizes II. The packing densities of likely arrangements" Phil. Mag. A 1980, 42, 721-740.

[17] Eldridge, M. D.; Madden, P. A.; Frenkel, D. "Entropy-driven formation of a superlattice in a hard-sphere binary mixture" Nature 1993, 365, 35-37.

[18] Klokkenburg, M.; Houtepen, A. J.; Koole, R.; de Folter, J. W. J.; Erné, B. H.; van Faassen, E.; Vanmaekelbergh, D. "Dipolar structures in colloidal dispersions of PbSe and CdSe quantum dots" Nano Lett. 2007, 7, 2931-2936.

[19] Talapin, D.V.; Shevchenko, E.V.; Murray, C.B.; Titov, A.V.; Král."Dipole-dipole interactions in nanoparticle superlattices" Nano Lett. 2007, 7, 1213-1219.

Appendix A
Scanning tunneling microscope - Experimental set-up

The results presented in this thesis are obtained by using three different scanning tunneling microscopy set-ups. A variable temperature STM (VT-STM), a low temperature STM (LT-STM) from Omicron Nanotechnology and a LT-STM. The VT-STM is stationed in Utrecht, the LT-STM in France, Lille (ISEN) and the LT-STM in Nijmegen. All three microscopes work at ultra-high vacuum (UHV), at a base pressure of $5{\cdot}10^{-11}$ mbar.

In figure A1, the VT-STM (Utrecht) is shown. The set-up consists of a fast entry lock (FEL), a preparation chamber and an analysis chamber. Via the FEL, a sample is inserted in the set-up and pumped down with a turbo molecular pump (Pfeiffer vacuum TMU261) to $\sim 1 \cdot 10^{-8} mbar$. At the same time, the FEL can be baked out to decrease the contamination from oxygen and water. With a transfer arm, the sample is transferred from the FEL to the preparation chamber which has a base pressure of $5 \cdot 10^{-11}\ mbar$. This base pressure is reached by making use of an ion getter pump (Varian midivac) and a titanium sublimation pump (TSP, vacuum generators ST22) In this research, this chamber is mainly used to vacuum anneal the sample up to $120^{\circ}C$. The sample is therefore positioned on a second manipulator in the preparation chamber. This manipulator has a heating element and a build-in thermocouple. Besides vacuum annealing, this chamber can be used for tip-preparation, sample cleaving (LT-STM) and sputtering (VT STM).

Via the transfer arm in the preparation chamber, the sample is transferred to the analysis chamber with the scanning tunneling microscope (and in the VT-system a STM and an atomic force microscope AFM). In this chamber, 12 samples can be stored in a carrousel. The LT-STM has 6 storage positions in the analysis chamber and 6 storage positions in the preparation chamber. A wobble-stick is used to transfer the samples and/or tips from the carrousel to the STM.

The VT-STM can be operated at different temperatures ranging from 20 to 1000 K. Liquid helium (LHe) or liquid nitrogen (LN_2) is used to cool down the sample with a flow cryostat. A clamping block is brought into contact with the sample holder and via conduction (through wires) from the cryostat to the clamping block, the sample is cooled down. In this UHV system only the sample temperature is adjusted, the tip and piezo drivers are kept at room temperature.

The LT-STM can operate at room-temperature as well as at 77 K and 5 K. In the analysis chamber, the STM is connected to two cryostats. The outer cryostat is normally filled twice a day with LN_2 and acts as a heat shield. Once a day, the inner cryostat is filled with LHe or LN_2 depending on the temperature at which the experiments are performed, 5 K or 77 K, respectively. In this system, both tip and sample have the same temperature. The STM is mounted on an Eddy current damping system to reduce vibration in the

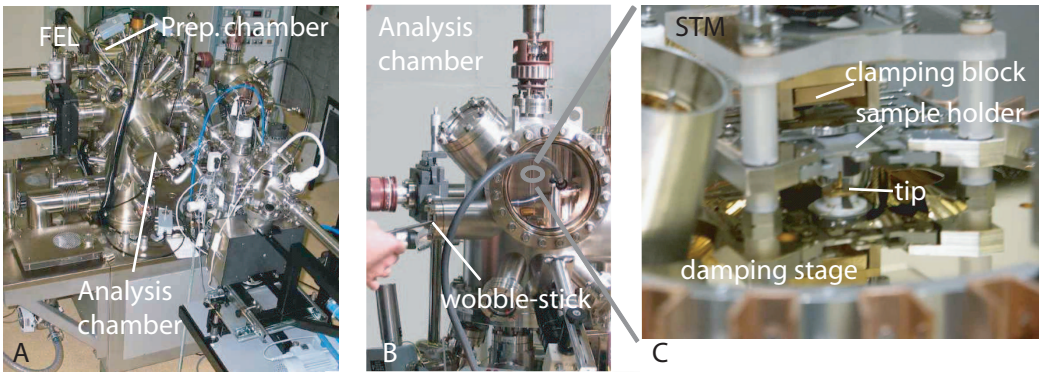

Figure A 1: Variable Temperature Scanning Tunneling Microscope used in the experiments performed on semiconductor QDs. (A) set-up showing the FEL, preparation and analysis chamber. The sliding transfer arms can transfer a sample from one to another chamber. (B) Analysis chamber, thorough a view-port, the STM stage is seen. With a wobble-stick, the sample can be manipulated and placed in the STM stage. (C) STM stage on an eddy current damping stage. The clamping block is used for electrical contact and sample heating and cooling.

experiments.

Appendix B
Sample and tip preparation

For sample preparation we used evaporated gold films on borosilicate glass from Metallhandel Schöer (0.5x1.0 cm, prepared at ESRON). They are flame annealed under hydrogen and cooled down/quenched under an Argon flow.[1] Gold grains are formed with atomically flat Au(111) surfaces with a typical diameter of 1 μm. The flame-annealed Au(111) substrate was immersed in a solution of 5 μL hexanedithiol (HxDT, $C_6H_{14}S_2$, Fluka purum > 97 %) in 10 ml methanol (CH_3OH, Aldrich) over night.[2] Figure B1 A shows a schematic representation of the sample preparation method. This procedure was performed in a glovebox under nitrogen atmosphere (oxygen- and water-free conditions). The substrate was thoroughly rinsed with methanol to remove the excess of HxDT from the surface and dried under nitrogen atmosphere. The substrate was then immersed in a dispersion of PbSe QDs in chloroform ($CHCl_3$, Aldrich) for a few minutes and rinsed with $CHCl_3$ to remove excess and non-covalently attached QDs. After sample preparation, the sample was inserted into the ultra high vacuum (UHV) system and annealed at 110°C prior to scanning tunneling microscopy (STM) experiments. This resulted in stable QDs, chemically linked to the gold substrate.

We investigated different sizes of PbSe QDs (synthesized according to reference 3) capped with oleic acid (OA) or recapped with hexylamine ($C_6H_{15}N$, 99 %, Fluka) ranging from 3-10 nm. The average diameter, shape and size distribution ($5-10$ %) were determined by transmission electron microscopy (TEM) and optical spectroscopy.

The tips used in STM are electrochemically etched tungsten (W) tips and or PtIr tips. Figure B1 B represents the set-up used for etching tungsten tips. We used high-purity tungsten wire (0.25 mm diameter, 99.95 % purity; Chempur) and sodium hydroxide (NaOH, Aldrich 97+ %). A drop of freshly prepared etchant solution (2 M NaOH) in doubly distilled water was put on a platinum wire ring cathode (wire thickness, 0.4 mm) producing a thin film (figure B1 B). The tungsten wire was placed vertically through the thin film (figure B1 B and C) and an AC-voltage was applied between the ring electrode and the wire electrode (+3V, 0.1 seconds and -1V, 0.05 seconds). After a few minutes, etching of the tip was complete (detailed information on the etching process can be found in e.g. references 4, 5). The lower section of the tungsten wire ($\sim$0.6 mm) was used as tip for STM. Before inserting the wire in the UHV system, the tungsten tip was dipped in double-distilled water and sonicated in ethanol for 10 seconds to remove contaminations and etching solution. A scanning electron microscope (SEM) image of this tip is shown in figure B1 D. As tungsten oxidizes over time, it was inserted in the UHV system immediately after preparation. Inside the UHV system, heating by electron bombardment was used to remove native oxide from the tip (tip preparation tool, Omicron Nanotechnology, 1 kV, 1.8 mA for 20 seconds).

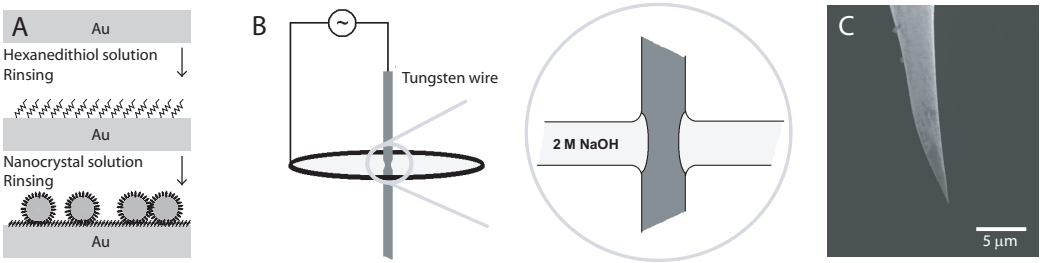

Figure B 1: Sample preparation (A) cartoon of sample preparation, a flame annealed Au(111) sample was immersed in a solution with hexanedithiol over night, rinsed and dried. Immersion of the sample in a dispersion of PbSe QDs results in stable attachment of the QDs on the Au(111) sample.

The PtIr tips can be fabricated by either electrochemical etching or by simple cutting. As the cutting procedure takes less time, mainly we used this method. The PtIr wire was cut using a pair of blunt scissors under an angle of $\sim 15°$. Finding a balance between cutting and pulling between the pair of scissors and the PtIr wire requires some experience; but once acquired, atomically sharp tips are produced in only a few seconds. Immediately after preparation, the PtIr tip was inserted in the UHV-system and it could directly be used for STM experiments. No annealing step was needed as PtIr does not oxidize.

References

[1] Bakkers, E.P.A.M. "Charge transfer between semiconductor nanocrystals and a metal" PhD thesis 2000, Utrecht.

[2] Colvin, V.L.; Goldstein, A.N.; Alivisatos, A.P. "Semiconductor nanocrystals covalently bound to metal surfaces with self-assembled monolayers" J. Am. Chem. Soc. 1992, 114, 5221-5230.

[3] de Mello Donegá, C.; Hickey, S.G.; Wuister, S.F.; Vanmaekelbergh, D.; Meijerink, A. "Single-step synthesis to control the photoluminescence quantum yield and size dispersion of CdSe nanocrystals" J. Phys. Chem. B 2003, 107, 489-496.

[4] Fotino., M. "Nanotips by reverse electrochemical etching" Appl. Phys. Lett. 1992, 60, 2935-2937.

[5] Ibe, J.P.; Bey Jr., P.P.; Brandow, S.L.; Brizzolara, R.A.; Burnham, N.A.; DiLella, D.P.; Lee, K.P.; Marrian, C.R.K.; Colton, R.J. "On the electrochemical etching of tips for scannin tunneling microscopy" J. Vac. Sci. Techn. 1990, 8, 3570-3575.

Samenvatting

Nanokristallen gemaakt van halfgeleider materialen zoals cadmium selenide (CdSe) en lood selenide (PbSe) zijn op dit moment van groot belang in colloidale nanowetenschappen. Vanwege een diameter kleiner dan 10 nanometer (1 nanometer is een miljardste meter) en de hoge mate van controle over de grootte en de vorm is het mogelijk om deze nanokristallen te gebruiken als bouwstenen voor toekomstig geminiaturiseerde optoelektronische circuits zoals bijvoorbeeld zonnecellen, LEDs, lasers en transistoren.

Halfgeleider nanokristallen zijn vanuit chemisch en fysisch standpunt zeer interessant. Dit komt omdat de elektronische structuur en de licht emissie en de daarmee samenhangende eigenschappen, zoals elektrische geleiding, sterk afhankelijk zijn van de grootte, de vorm en het materiaal waarvan de kristallen zijn gemaakt. Het samenvoegen van twee soorten nanokristallen van verschillende grootte en samenstelling in geordende structuren (een zogenoemd binair superkristal), zou kunnen resulteren in 'nieuwe' materialen met optoelektronische eigenschappen, die in de natuur niet voorkomen.

De uiteindelijke eigenschappen van dit soort superroosters zullen sterk afhangen van de interacties tussen de verschillende bouwstenen. In deze thesis wordt één soort interactie tussen nanokristallen in detail bestudeerd, namelijk de elektronische (quantum mechanische) koppeling. Met het kleiner worden van optische en elektronische circuits, wordt het maken van elektronische contactpunten een steeds grotere uitdaging. De karakteristieke eigenschappen van de contactpunten op nanokristal structuren zullen waarschijnlijk van cruciaal belang zijn in de werking van deze nieuwe structuren.

Om de invloed van elektronisch koppeling en elektronische contacten te bestuderen, is in dit onderzoek gebruik gemaakt van de scanning tunneling microscoop. Deze microscoop is ontwikkeld in de jaren tachtig door Binnig en Rohrer die voor dit werk de Nobelprijs ontvingen. De eerste experimenten op nanokristallen zijn pas uitgevoerd in 1995. De scanning tunneling microscoop is gebaseerd op het meten van een elektrische stroom die ontstaat als elektronen tunnelen tussen een scherpe metalen punt (tip) en een geleidend oppervlak, het substraat. De tip wordt op een afstand van minder dan een nanometer boven

het substraat gebracht waarop de nanokristallen zijn aangebracht. De tip wordt in een lijn over het oppervlak bewogen en de hoogte verandering wordt gemeten terwijl de tunnelstroom tussen tip en substraat constant blijft. Dit kan vergeleken worden met een naald die loopt over een langspeelplaat, maar dan op een veel kleinere schaal. Op deze manier ontstaat een driedimensionaal plaatje van het oppervlak, oftewel een topografieplaatje met subnanometer resolutie.

Vanuit deze topografische plaatjes kan een nanokristal naar keuze worden uitgezocht. De tip wordt boven het nanokristal geplaatst, zodat er een lokaal 'elektrisch contact' wordt gemaakt. Men meet de tunnelstroom als functie van het aangelegde potentiaalverschil tussen tip en substraat. Met spectroscopie kan de elektronische structuur van één individueel nanokristal bestudeerd worden, maar ook de elektronische koppeling van een nanokristal met naastgelegen deeltjes in een grotere geordende structuur. Scanning tunneling microscopie combineert topografie metingen en spectroscopie metingen met extreem hoge resolutie.

In dit proefschrift worden de elektronische structuur (energieniveaus van elektronen en gaten) van CdSe en PbSe nanokristallen gemeten, en de verandering van de elektronische struktuur als gevolg van interactie tussen de nanokristallen. De keuze voor CdSe en PbSe komt voort uit de grote verschillen in elektronische eigenschappen; CdSe nanokristallen emitteren in het zichtbare deel van het elektromagnetische spectrum (zichtbaar licht) en PbSe nanokristallen in het nabije infra-rode gebied (bruikbaar voor telecommunicatie).

De hierboven beschreven halfgeleider nanokrystallen, hun eigenschappen en nanokristal structuren worden beschreven in hoofdstuk 1. Dit wordt gevolgd door een theoretisch hoofdstuk over de scanning tunneling microscoop. In hoofdstuk 2 wordt de basis gelegd voor de interpretatie van de meetresultaten beschreven in de verdere hoofdstukken.

In hoofdstuk 3 worden de resultaten van de metingen op individuele PbSe nanokristallen van 3 tot 10 nanometer in detail beschreven. Om de nanokristallen te stabiliseren en niet te laten bewegen tijdens de metingen, zijn deze chemisch vast gezet op het substraatoppervlak met behulp van verbindingsmoleculen. De resultaten van onze metingen laten de invloed van de grootte van de nanokristallen op de elektronische structuur zien. Naast scanning tunneling microscopie wordt ook vaak een andere meettechniek gebruikt om de eigenschappen van nanokristallen te bepalen; optische spectroscopie. Het nadeel van deze methode is echter dat het geen eigenschappen van individuele nanokristallen kan meten. Met behulp van de STS metingen op individuele nanokristallen hebben we de elektronische structuur dermate nauwkeurig kunnen bepalen, dat optische overgangen veel preciezer konden worden begrepen.

De studie naar de eigenschappen van individuele nanokristallen is ook gebruikt als basis om elektronische koppeling tussen de PbSe nanokristallen in grotere geordende structuren (moleculen) te bestuderen. Hiervoor hebben we een nieuwe techniek ontwikkeld om de PbSe deeltjes, monomeren, dimeren, trimeren en grotere aggregaten, te stabiliseren in een inerte matrix van CdSe deeltjes. Op deze manier is het effect van elektronische koppeling als functie van het aantal PbSe buren te meten. In hoofdstuk 4 zijn de resultaten van deze experimenten weergegeven. Zij tonen aan dat, bij een toename van het aantal PbSe nanokristallen die in elkaars buurt liggen, de elektronische koppeling sterker wordt. Uit dit onderzoek is ook gebleken, dat de koppelingssterkte sterk variëert van plaats tot plaats en een maximale waarde bereikt ongeacht de grootte van de PbSe nanokristal structuur.

Hoofdstuk 5 beschrijft de elektronische koppelingssterkte in monolagen bestaande uit honderden PbSe nanokristallen. Ook hier valt op dat de elektronische koppelingssterkte sterk varieert, zelfs wanneer de lagen, gemaakt van deze deeltjes, 'perfect' geordend lijken. Dus ondanks dat topografische plaatjes zeer geordende structuren van nanokristallen laten zien blijkt de elektronische structuur dit niet te zijn. Deze resultaten zijn van groot belang voor de toepassing van nanokristallen in opto-elektronische circuits en verschaffen inzicht in de elektronische processen op lokale schaal.

De elektronische structuur van CdSe nanokristallen die enkele en dubbele lagen vormen op het substraat is beschreven in hoofdstuk 6. Voor de aanvang van de metingen was het niet duidelijk of scanning tunneling spectroscopie op dikkere lagen van nanokristallen mogelijk was. We hebben aangetoond dat dit inderdaad mogelijk is en dat de potentiaalverdeling over de nanokristalstructuren grote invloed heeft. De elektronische koppeling tussen de CdSe deeltjes is zwak (zoals ook getoond in de resultaten beschreven in hoofdstuk 4) en is niet meetbaar met tunneling spectroscopie. In deze structuren zijn de effecten van het elektrische veld tussen tip en CdSe nanokristallen (dit is het elektrisch contact) belangrijk gebleken; het veld hangt sterk af van de positie van het CdSe nanokristal in het rooster. Deze resultaten bieden goede perspectieven om de elektronische eigenschappen van nog complexere structuren, te bestuderen op lokale schaal.

In hoofdstuk 7 worden de eerste resultaten in de formatie van binaire structuren beschreven. De structuren zijn gemaakt van CdSe en PbSe nanokristallen. Via vloeistofverdamping uit de nanokristal suspensie vormen de nanokristallen geordende structuren. Uit experimenten is gebleken dat zowel de verhouding in diameter als de concentratie verhouding van CdSe en PbSe nanokristallen bij een gegeven diameter van invloed zijn op de formatie van geordende structuren. Zo worden bijvoorbeeld bij een verhouding van 0.57 voornamelijk AB_2 en cub-AB_{13} structuren gevormd. Vergelijking met een theoretisch 'harde

bollen' model suggereert dat interacties tussen de nanokristallen ook belangrijk zijn in de formatie van binaire structuren aangezien dit model de stabiliteit van AB_2 voorspelt maar de stabiliteit van cub-AB_{13} niet geheel kan verklaren. De gefabriceerde structuren zijn meestal driedimensionaal en dik genoeg voor toekomstige elektronische en optische toepassingen.

List of publications

- Overgaag, K.; Liljeroth, P.; Vanmaekelbergh, D.; Mahieu, G.; Grandidier, B.; Delerue, C.; Allan, G. "Contribution of the intervalley splitting to the linewidth of resonances in tunneling spectroscopy of PbSe nanocrystals" in preparation. (Chapter 3).

- Jdira, L.; Overgaag, K.; Stiufiuc, R.; Grandidier, B.; Delerue, C.; Speller, S.; Vanmaekelbergh, D. "Linewidth of resonances in scanning tunneling spectroscopy" Phys. Rev. B. 2008, 77, 205308/1–11. (Chapter 3).

- Liljeroth, P.; Jdira, L.; Overgaag, K.; Grandidier, B.; Speller, S.; Vanmaekelbergh, D. "Can scanning tunnelling spectroscopy measure the density of states of semiconductor quantum dots?" Phys. Chem. Chem. Phys. 2006, 8, 3845–3850. (Chapter 3).

- Overgaag, K.; Liljeroth, P.; Grandidier, B.; Vanmaekelbergh, D. "Scanning tunneling spectroscopy of individual PbSe quantum dots and molecular aggregates stabilized in an inert nanocrystal matrix" ACS Nano 2008, 2, 600–606. (Chapter 4)

- Liljeroth, P.; Overgaag, K.; Urbieta, A.; Grandidier, B.; Hickey. S.G.; Vanmaekelbergh, D. "Variable orbital coupling in a two-dimensional quantum-dot solid probed on a local scale" Phys. Rev. Lett. 2006, 97, 096803/1–4. (Chapter 5).

- Overgaag, K.; Jdira, L.; Speller, S.; Vanmaekelbergh, D.; Liljeroth, P. "Scanning Tunneling Spectroscopy of arrays of CdSe quantum dots: Response of wavefunctions to local electric fields" Nano Lett. 2008, submitted. (Chapter 6).

- Overgaag, K.; Evers, W.; de Nijs, B.; Koole, R.; Meeldijk, J.; Vanmaekelbergh, D. "Binary Superlattices of PbSe and CdSe Nanocrystals" J. Am. Chem. Soc. 2008, 130, 7833–7835. (Chapter 7).

- Rosso-Vasic, M.; Spruijt, E.; Popovi, Z.; Overgaag, K.; van Lagen, B.; Grandidier, B.; Vanmaekelbergh, D.; De Cola, L.; Zuilhof, H. "Amine-terminated silicon nanoparticles: synthesis, optical properties and their use in bioimaging" J. Mat. Chem. 2008, submitted.

- van Huis, M.A.; Kunneman, L.T.; Overgaag, K.; Xin, Q.; Pandraud, G.; Zandbergen, H.W.; Vanmaekelbergh, D. "Nanocrystal unification through rotations and reconstructions probed by $in\ situ$ transmission electron microscopy during low-temperature annealing" Nano Lett. 2008, submitted.

Dankwoord

In de afgelopen jaren heb ik met veel plezier gewerkt aan het onderzoek beschreven in dit proefschrift. Mijn naam staat dan wel op de voorkant van dit proefschrift, maar in feite zou daar een lange lijst van namen moeten staan. Een proefschrift wordt vaak toegeschreven aan één persoon, maar is het resultaat van de inspanning van velen.

Allereerst mijn promotoren Daniel Vanmaekelbergh, John Kelly en mijn copromotor Peter Liljeroth, bedankt voor de uitstekende begeleiding. Daniel, je kritische instelling en je tomeloze ambitie en enthousiasme hebben mij steeds gestimuleerd. Bedankt voor de vrijheid en het vertrouwen dat je me hebt gegeven tijdens mijn onderzoek en het afronden van mijn proefschrift. John, ik ben je dankbaar voor de algemene begeleiding, je toegankelijkheid zal me altijd bijblijven. Peter, "kiitos", your door was always open and discussions with you resulted often in creative solutions. One thing is certainly true: 'STM rules your life".

Dit onderzoek zou niet mogelijk zijn geweest zonder de hulp van Hans Ligthart, het technisch brein van onze onderzoeksgroep. Hans, voor elk probleem dat ik tegenkwam had jij een oplossing. Stephan Zevenhuizen, de ICT-er van onze groep, jij loste met het grootste gemak de voor mij onoverkomelijke problemen met de computer op. Jessica Heilbrunn, de secretaresse van onze groep, jij hield alles in de gaten en er ontging je niets. Enorm bedankt voor de hulp die ik tijdens mijn promotieonderzoek van jullie heb gehad.

Voor mijn metingen met de scanning tunneling microscoop had ik vaak vloeibare helium en stikstof nodig. Ook in tijden dat helium niet zo makkelijk voorhanden was, had ik nooit problemen om de metingen uit te voeren. Iedereen van de cryogene afdeling, bedankt, vooral Nico Kuipers, want door jouw inzet kwam altijd alles op zijn pootjes terecht.

Samenwerken met onderzoeksgroepen in de wereld is inspirerend en leerzaam. De volgende personen waarmee ik heb samengewerkt mogen dan ook niet ontbreken in dit dankwoord:

Aux Guy Allan et Christophe Delerue de l'Institut d'Electronique, de Micro-électronique et de Nanotechnologie (IEMN, département ISEN) à Lille: grâce à vos calculs et à nos discussions stimulantes, la base théorique de cette thèse est solide. A Bruno Grandidier: un grand merci pour la collaboration fructueuse sur les expérimentations avec le STM. Je me souviendrai de nos inoubliables discussions intéressantes (et parfois énervantes) et de votre soutien continu pendant mon séjour à l'ISEN. Merci également à Dominique Deresmes, Loic Patout, Maxime Berthe, Ana Urbieta, Rares Stiufiuc et Gautier Mahieu pour leur agréable collaboration. J'ai bien aimé votre compagnie à tous et nos discussions en langue française. Je n'oublierai jamais les déjeuners plaisants avec le groupe.

My acknowledgements also to Lucian Jdira from the group of Silvia Speller at the University of Nijmegen. We had interesting discussions on our joint experiments which resulted in the papers discussed in chapter 3 and 6. I'm very grateful for the opportunity to collaborate with you.

With Gal and Cecile from the group of Efrat Lifshitz of the Institute of Technology in Haifa, Israel, STM experiments on core-shell nanocrystals were performed. De samenwerking met Milena van de groep van Han Zuilhof in Wageningen heeft geresulteerd in mooie meetresultaten op silicium clusters. Met Marijn van de groep van Henny Zandbergen in Delft, zijn metingen verricht met TEM op monolagen van PbSe nanokristallen. Ook loopt er nog een tomografie onderzoek met Heiner en Petra van de groep van Krijn de Jong en met Alfons van Blaaderen, dat al prachtige meetresultaten aan binaire structuren heeft opgeleverd. Met Laura van de groep van Marjolein Dijkstra, is gestart met berekeningen aan binaire structuren. Allen hartelijk dank voor de samenwerking.

En dan de studenten die ik heb begeleid bij bachelor- of masterprojecten, van harte bedankt voor jullie bijdragen aan dit proefschrift: Ebru and Zafer (exchange students from Turkey), you were the first to start with the project on the formation of binary structures. Starting a new project is difficult, and I appreciate your perseverance. Maarten, jij hebt je ingezet om berekeningen te doen aan gekoppelde systemen; Evelien, met de AFM heb je een sterk begin gemaakt met het onderzoek naar de eigenschappen van binaire structuren. Dit onderzoek krijgt zeker een vervolg. Mark, met veel inzet heb je het maken van binaire structuren opgepakt; Bart en Wiel, jullie gaven niet op en maakten de eerste micrometers grote binaire structuren wat resulteerde in een prachtig artikel in samenwerking met TEM specialist Hans Meeldijk. Lucas, je onderzoek kreeg een mooie wending, van de scanning tunneling microscopie naar de TEM in Delft en een publicatie in het vooruitzicht. Ik wens jullie allemaal veel succes in de toekomst met jullie promotieonderzoek, baan of verdere studie.

Graag wil ik al mijn collega's van de groep Condensed Matter and Interfaces bedanken voor de fascinerende en interessante discussies in de afgelopen vier jaar: Harold, Andries, Cees, Jan, Thijs, Sven, Bert, Arjan, Bryan, Shuai, Linda, Heng-Yu, Zhixiang, Ingmar, Aleksander, Rolf, Floris, Philipp en Volker. In het bijzonder wil ik Dennis, Harold en Rianne noemen. Ik hoop dat we elkaar in de toekomst niet uit het oog zullen verliezen.

Aan de andere kant van het 'Ornstein' laboratorium zit het 'van der Graaff' laboratorium. De eerste drie jaar van mijn promotieonderzoek heeft daar de STM gestaan voordat deze verhuisde naar de kelder van het Ornstein lab. Tijdens de lange meetdagen bij de STM heb ik het genoegen gehad met veel mensen kennis te maken. In het bijzonder Elmuez Dawi en Mirela Georgescu! Met Pedro Zeijlmans van Emmichoven en Mirela heb ik de meetopstelling gedeeld en vele discussies gevoerd om de opspelende experimentele problemen op te lossen.

Ik zou dit dankwoord willen afsluiten met de boude bewering dat het schrijven van een proefschrift niet louter een wetenschappelijke exercitie is. Naast degenen die mij bij dit laatste gesteund hebben, zou ik dan ook degenen die op een andere, maar niet minder essentiële manier, hebben bijgedragen aan het tot stand komen van dit proefschrift willen bedanken. Want het proces naar dit resultaat had veel weg van het Leitmotiv uit de Romantiek: "Himmelhoch jauchend zum Tode betrübt". En vooral wat betreft deze laatste gemoedstoestand heb ik veel aandacht en begrip mogen ondervinden van familie en vrienden.

Lieve pap en mam, jullie zijn geweldig. Dank jullie wel voor de interesse die jullie altijd tonen en de steun in de keuzes die ik maak. Alex en Anja, Lucien, bedankt voor de gezellige etentjes op zondagavond. Opa en Oma, Cor en Mieke, Arno en Tamara, jullie zijn een geweldige 'schoon'-familie, bedankt voor jullie belangstelling. Lieve Sander, dank je voor alle discussies, gezellige avonden en weekendjes, zonder jou was het allemaal een stuk minder leuk geweest.

En dan als laatste, mijn paranimfen: Elmuez Dawi en Remco Nieuwland, bedankt dat jullie me bij wilden staan bij de verdediging van dit proefschrift.

Curriculum Vitae

Karin Overgaag was born in Dosso, Niger on May 24^{th} 1978. She obtained her secondary school diploma (O-level) at the Agnes College in Leiden in 1996. She studied Applied Physics at the Rijswijk Institute of Technology, where she obtained her bachelor degree of engineering in 2001. She did her graduation research on patterning and drying two-dimensional colloidal structures using optical tweezers at the 'Institute of Atomic and Molecular Physics' (AMOLF) in Amsterdam. She continued her study applied physics at Twente University, where she obtained her master in science in 2004 by studying the emission of quantum dots in photonic crystals.

The 1^{st} of October 2004 she started her PhD research in the group Condensed Matter and Interfaces of the Debye Institute for Nanomaterials Science at Utrecht University. Under the supervision of prof. dr. Daniël Vanmaekelbergh, prof. dr. John Kelly and dr. Peter Liljeroth, she studied electronic coupling in self-assembled nanocrystal arrays using a scanning tunneling microscope. During this period, a fruitful collaboration was established with the 'Institut d'Electronique, de Microélectronique et de Nanotechnologie' (IEMN, département ISEN) where many of the STM experiments were performed. The results of her PhD research are described in this thesis and have been published in scientific journals.

Besides her research activities she assisted in physical chemistry courses, analytical chemistry practica and supervised bachelor and master students. She followed courses in 'Organization and Leadership', and 'Science communication for PhD Students'. Furthermore during her studies she was a full-time board member (treasurer) of the student association NOVA in Rijswijk. During her PhD period she also contributed to conferences (presentations) and a summer school in nanoscience.